Polyoxometalates on Nitrogen-Containing Carbon Supports as Catalysts for Selective Oxidation

by

Xiaowen Zhao

A dissertation submitted in partial fulfillment
of the requirements for the degree of
Doctor of Philosophy
(Chemical Engineering)
in the University of Michigan
2019

Doctoral Committee:

Professor Mark A. Barteau, Co-Chair
Professor Emeritus Levi T. Thompson, Co-Chair
Professor Bart M. Bartlett
Professor Johannes W. Schwank

Xiaowen Zhao

smllle@umich.edu

ORCID iD: 0000-0001-8222-5542

Dedication

To my parents, Yufei, Tardis and Tamaki.

Acknowledgements

I would like to thank my advisor Professor Mark Barteau. Thank you for your critical eye and always stopping me before I spent too much time in a rabbit hole. Thank you for helping me hone all my presentations and writings again and again with so much patience. Thank you for being so supportive and approachable even when you are very busy in your other roles. Your mentorship is the most important factor that has helped me make progress along the way in the past four years. I think you are the best advisor ever.

I would like to thank my committee co-chair Professor Levi Thompson, for giving me professional advices and for inviting me to all the group meetings, lunches and parties, I have gained professional knowledge, improved my presentation skills and built friendship because of these opportunities. And thank you for letting me use the awesome instruments in your lab, including NH_3-TPD, BET and TGA, as those have produced essential characterization results in my work.

I would like to thank Professor Schwank and Professor Bartlett for serving on my committee. Thank you for being so patient with me with every meeting scheduling. And I really appreciate your advices in our previous meetings.

I would like to thank all the brilliant members of Barteau group and Thompson group. In particular, I would like to thank Trent Silbaugh, Wei-Chung Wen, Sarah Carl, Yixuan Chen, Jeejay Chen, Yuan Cao, Sarah Paleg, Zixuan Wang, Jiwoong Kang, Connor McGlothin, Scott Johnson and Benjamin Silcox, for friendships and helps on my project.

I would like to thank Trenton Wilke for being great mentor and friend, for helping me get started in the lab four years ago and for always being there when I have questions. My PhD life will be a lot harder without you!

I would like to thank Elizabeth Wilson for being such great friend. I used to be very nervous when talking to people in English, but you and Trenton have helped me overcome that. You have made our office such a happy place to work in and I will be missing you a lot!

I would like to thank my other friends in Ann Arbor, Ting-Wen Lo, Max Ma, Maria Ma, Tingting Han, Ying Yang and Shujie Chen, for all the board games, sitcoms, movies, foods and wonderful trips we enjoyed together. You have made my PhD years colorful!

I would like to thank my friends back in China, Shan Su, Wenjie Sun, Xinya Yang and Rui He. Thank you for the long-distance friendship and I miss you all!

I would like to thank my cats Tardis and Tamaki, for being cute (almost) all the time and for always reminding me that eat-well, sleep-well and play-well are very important elements in a happy (cat) life.

I would like to thank my parents for supporting me along the way, for all the encouragements, and for always being there when I was upset. I love you.

At last, I would like to acknowledge Yufei Wei, for being a great mentor for the modeling part of this work and a wonderful boyfriend. Thank you for helping me go through my darkest days when I hurt my knee and when I (ridiculously) thought I got skin cancer. You are the one that make Ann Arbor feel like home. I love you.

Table of Contents

List of Tables

List of Figures

List of Schemes

List of Equations

Abstract

Polyoxometalates (POMs) represent an important class of metal oxygen clusters of the early transition metal elements. Supported POMs are good model catalysts for transition metal oxide catalysts because of their stable and well-known structure as well as the possibility of controlling acid site population in these catalysts. Physical, chemical and catalytic properties of POMs, e.g., $H_3PMo_{12}O_{40}$ (HPM) supported on nitrogen-containing carbon materials were investigated in this work to understand support effects. Activated carbon (C), nitrogen-doped graphitic carbons, N-C-1000 (2 N-atom%) and N-C-600 (19 N-atom%), and mesoporous graphitic carbon nitride, mpgC_3N_4 (53 N-atom%) were used to study the influence of both nitrogen content and different nitrogen species.

Our results showed that the polyoxometalate framework was retained on all the four supports tested in this work, and the ability to disperse POMs without crystallite formation followed the trend N-C-600 < N-C-1000 ≈ activated carbon (C) < mpgC_3N_4. POMs preferentially interact with pyridinic nitrogen and surface amino groups; the latter lead to ammonium POM salt crystallites observed using X-ray Diffraction (XRD), while the former could be one of the reasons that mpgC_3N_4 can produce monolayer POM dispersions. At low coverage, POMs are molecularly dispersed on all four supports. At comparable POM coverages, the H^+/POM ratio followed the trend C ≈ N-C-1000 > N-C-600 > mpgC_3N_4. The POM loading effect on the POM-support interaction was also investigated. On C, as POM loading is increased, both population

and strength of the acid site increased as shown by ammonia temperature programmed desorption (NH_3-TPD), while on N-C-600 and mpgC_3N_4 such increase was not observed.

C and N-C-1000 supported POM catalysts with comparable POM surface coverages showed similar dehydration/oxidation activities in methanol oxidation. However, N-C-600 and mpgC_3N_4 exhibited lower activities for both reactions. The simultaneous decrease for dehydration and oxidation activities as supports with higher nitrogen content were used confirmed that protons played an important part for methanol oxidation using supported POM catalysts. The selectivity for oxidation products can be improved when a small but finite number of acid sites exist on the catalyst surface. For supports used in this work, N-C-600 provides an optimal number of acid sites and thus results in the highest selectivity for the sum of all oxidation products (CO_X excluded), as well as the highest selectivity for formaldehyde (80%).

To further understand how different supports can affect the reaction outcome, mechanism-based kinetic models were constructed for both primary and secondary products in methanol dehydration and oxidation for the first time in the literature and are shown to have worked well for HPM/C and HPM/N-C-600 catalysts. Based on the proposed mechanism, formaldehyde (HCHO) and methyl formate (MF) may form on the same site (likely on the bridging O in the vicinity of H^+); dimethyl ether (DME) and dimethoxymethane (DMM) may form on the same site (H^+). The rate constant for the rate determining steps in DME and HCHO formation tracked the decreasing trend observed when catalysts were compared at similar POM surface coverage levels. N-C-600 supported catalysts exhibited lower rates of DMM formation, leading to higher HCHO selectivity.

This is the first systematic study of support effects for nitrogen-containing carbon support POM catalysts, which can provide guidance in using supports to tune the properties of supported POMs other than changing the identity of its center/framework atom and counter cations.

Chapter 1 Introduction

1.1 Keggin-type Polyoxometalates (POMs)

Polyoxometalates (POMs), also referred to as heteropolyacids (HPAs) in their acid form, represent an important class of metal oxygen clusters of the early transition metal elements. The unmatched range of physical and chemical properties arising from their wide variety of molecular structures and sizes have made them particularly interesting for a variety of applications. POMs discussed in this work will be the Keggin-type (with the general formula $XM_{12}O_{40}^{x-8}$, structure see Figure 1-1), where 12 octahedra structures, each containing a MO_3 (M = Mo^{6+}, W^{6+} or V^{5+}), surround a XO_4 center (X= P^{5+}, Si^{4+}, As^{5+}, etc.)[1-3]. Cations such as H^+, Na^+, Cs^+, Ca^{2+}, Cu^{2+} can be used to balance the negative charge of POM anion[4-6]. Keggin POMs, among all POMs, are the most stable and easily synthesized POM structure, and possess interesting redox and Brønsted acid properties[1-3]. These properties can be tuned systematically by changing heteroatoms (X), framework polyatoms (M), or by choosing different counter-cations[7]. Keggin-type POMs have been applied to catalysis[8-12], electrochemistry[13, 14], photochemistry[15, 16] , energy storage[17], and to solve environmental problems[18].

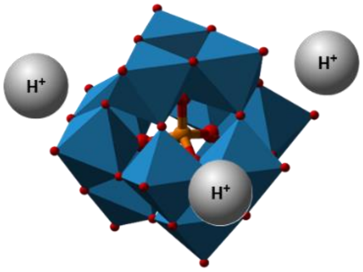

Figure 1-1. An example of Keggin POM in the acid form

In the solid state, POMs can form secondary and tertiary structures. Secondary structure refers to the three-dimensional arrangement of POM polyanions, cations, water of crystallization and other molecules if present[19]. Tertiary structure refers to the size of POM particles, pore structure, distribution of protons in the particle, etc. Tertiary structure can be greatly influence by the identity of cations. For example, when large ions like Cs^+ and NH_4^+ are used as cations for POMs, the corresponding salt can form a very porous structure with high surface area, whereas the H form or Na^+ salt of POMs have low surface areas (1-15 m^2/g)[19].

The thermal stability of heteropoly acids changes with the heteroatom and framework polyatoms following the trend: $H_3PW_{12}O_{40} > H_3PMo_{12}O_{40} > H_4SiMo_{12}O_{40}$. Thermolysis of $H_3PMo_{12}O_{40}$ has been shown to proceed by loss of water of crystallization and then of constitutional water. The Keggin structure of $H_3PMo_{12}O_{40}$ will be completely destroyed when the temperature is above 450°C[19].

The strength and number of acid sites on POMs can be controlled by the composition of POMs, extent of hydration, cation identity, support interactions and thermal treatment. Solid acid-form POMs possess Brønsted acidity. The acid strength of crystalline acid-form POMs follows the trend: $H_3PW_{12}O_{40} > H_4SiW_{12}O_{40} > H_3PMo_{12}O_{40} > H_4SiMo_{12}O_{40}$[3].

1.2 Supported POMs in catalysis

Catalysis was one of the first applications of POMs and it is still a major research focus. A key difficulty in utilizing POMs for many heterogeneous catalytic processes stems from their low bulk surface area (for acid-form POMs and most of the POM salts) and their high solubility in water and many organic solvents[3]. This can be overcome by supporting POMs on insoluble, high surface area supports. Supported POMs have been applied to both acid and oxidation catalysis[19] and have been used as catalyst for industry process, e.g. hydration of olefins, oxidation of methacrolein to methacrylic acid and production of ethyl acetate from ethylene and acetic acid, among others.[20-23]

1.2.1 Supported POMs as model catalyst

Supported POMs can also serve as model catalysts for more complicated transition metal oxide systems, since individual POM molecules can be viewed as transition metal oxide clusters with very stable, well-understood structure.[7, 24-26] Moreover, the catalytic properties of POMs can be changed by varying composition while maintaining a constant structure[25].

Previous works from Barteau and co-workers have shown that the by studying POMs deposited on graphite using tunneling spectroscopy with a scanning tunneling microscope, one can gain valuable information about the site requirements for catalysis by transition metal oxides[7, 27, 28]. Iglesia and co-workers have also used supported POM catalysts for fundamental catalysis studies[24, 25]. They have performed both experimental and Density Function Theory (DFT) studies using SiO_2-supported POM catalysts to understand the mechanistic details in oxidation and acid catalysis of methanol[29].

The two principal properties of POMs of interest in catalysis, redox behavior and Brønsted acidity, are often viewed as creating competing reaction channels for reactants that can undergo either oxidation or acid-catalyzed reactions. However, in recent years there are a number of results from supported POM catalyst studies that have indicated that some level of catalyst acidity is necessary to promote oxidation[21, 24, 30]. Examples include methacrolein oxidation with $H_{3-x}Cc_xPMo_{12-y}V_yO_{40}$ (1.5< x< 3, 0< y< 2, Cc, counter cations such as alkali metal, especially Cs)[21], methanol oxidation with SiO_2-supported $H_3PMo_{12}O_{40}$ and $H_4SiMo_{12}O_{40}$[24, 30] and ethylene oxidation with Pd-POM/SiO_2 catalysts[31]. Gaining control over the acid sites for supported POM catalysts thus becomes increasingly desirable. One common way to control the acidity of POMs is by exchanging other cations for H^+ [6, 19]. However, when preparing dispersed POM catalysts this strategy may be limited by the solubility of some POM salts and by differences in the ability to disperse these well on different supports, as well as by potential impacts of the counter cation on the stability of the POM framework during catalyst synthesis and reaction.

1.2.2 Support effects

Recently researchers have reported that interaction with specific supports can also indirectly tune the acid-base or the redox properties of POMs, which opens up new routes to design supported POM catalysts with optimal activity[26, 32]. Metal oxides such as ZrO_2, TiO_2, SiO_2, and Al_2O_3, etc. have been used as supports for POMs[3, 33]. Basic oxides such as Al_2O_3 and MgO tend to decompose POMs[9]. Iglesia and co-workers[33] have reported that rates of CH_3OH oxidative dehydrogenation for ZrO_2 and TiO_2 supported POMs are higher than the SiO_2 supported ones at similar POM surface coverage levels, indicating that the identity of supports can influence redox properties of Keggin clusters. Reaction rates were much lower on Al_2O_3, because POM tend to decompose on this support to form less active metal oxide domains. Selectivities to secondary products in methanol oxidation are also reported to be affected by the chemical properties of support surfaces. Acidic SiO_2 surfaces favored dimethoxymethane formation, whereas ZrO_2 and TiO_2 led to methyl formate formation.

Another commonly used support, carbon, has stronger interaction with POMs compared to metal oxides. $H_3PMo_{12}O_{40}$ can self-assemble into a monolayer with a periodic structure on highly oriented pyrolytic graphite, which has a graphite-like structure but with no surface functional groups [7, 34]. Carbon nanotubes[35, 36] , mesoporous carbon[37], activated carbon[8], and graphene[26, 38] have all been reported as POM supports. On activated carbon, up to 10wt% POMs are reported to be strongly adsorbed, which results in a weaker acidity of this supported POM system compared to bulk POM. No crystallization occurs even when the $H_3PW_{12}O_{40}$ loading is as high as 45wt% on activated carbon[3]. Further modification of carbon, for instance by adding nitrogen groups, can add to its interaction with POMs.

1.2.3 Nitrogen containing carbons as support for POMs.

Four kinds of nitrogen-containing carbon supports for POMs have been previously explored in the literature. One is carbon modified with $-NH_2$ on the surface. The Song group has successfully loaded well-dispersed POMs on $-NH_2$ decorated carbon spheres[39] and carbon aerogels[40]. The supported POM catalysts prepared this way were reported to be good selective oxidation catalysts for isopropanol oxidation, which showed enhanced oxidation activity (formation of acetone) and suppressed acid catalytic activity (formation of propylene and isopropyl ether) compared to unsupported POM catalysts.

Another support discussed in the literature is carbon embedded with nitrogen. In such materials there may be one or more nitrogen species such as pyridinic, pyrrolic, or graphitic nitrogen in the carbon structure instead of just $-NH_2$ group grafted on the support surface. The Song group used nitrogen-containing carbon (N-C) with 2wt%[39, 41], 3.6wt%[37], 10.6wt%[42] nitrogen to support $H_3PMo_{12}O_{40}$ or $H_5PMo_{10}V_2O_{40}$, and reported the catalysts were useful in selective conversion of methanol to dimethoxymethane[41] as well as in methacrolein oxidation[39], displaying in both cases a decrease in acid catalytic activity and an enhanced oxidation activity compared to the unsupported POMs. In the case of 2 wt% N-C, the composition was found to be 79.8% quaternary nitrogen, 17.0% pyridinic nitrogen and 3.2% of nitrogen oxide species[41]. They proposed that the edge quaternary nitrogen species can be more easily converted into positively charged nitrogen groups than pyridinic nitrogen, and thus could play an important part in immobilizing POM. Liu and co-workers[43] synthesized POM/nitrogen-functionalized, onion-like carbon hybrid catalysts. They observed in X-ray photoelectron spectroscopy (XPS) an increase in graphitic nitrogen N 1s signal with the increase of POM loading and concluded that POMs could bond to graphitic nitrogen through electrostatic interactions.

Conductive polymers such as polyaniline[11], polypyrrole[44], and poly(4-vinylpyridine) [45] have been studied as supports with generally higher loading of POMs and better dispersion. Hasik et al. [11] reported 35.2wt% $H_3PW_{12}O_{40}$ dispersed on polyaniline with no crystal phase observed in XRD. The high nitrogen content in the support (15.5wt%) proved to be very effective in the blocking of acid-base functions of POMs. When applied in catalytic isopropanol decomposition, the POM/aniline catalyst was reported to be 96.4% selective to acetone at 130°C.

Mesoporous carbon nitride (mpgC_3N_4) is another interesting possible support for POMs. Compared to the other three kinds of nitrogen-containing carbon supports discussed above, mpgC_3N_4 has an ordered structure (similar to that of graphene) and it has a nitrogen content even higher than the three nitrogen-containing conductive polymers discussed above (more than 50wt %, about 53 atom%)[46]. Because of its semi-conducting nature, current literature studying mpgC_3N_4 supported POMs has been mainly focused on photocatalysis such as organic pollutant degradation [47]. Few groups have reported POM/C_3N_4 as oxidation catalysts. Long et al. [48]studied the use of g-C_3N_4-$H_5PMo_{10}V_2O_{40}$ as a dual catalysts system for aerobic oxidation of benzene to phenol (liquid-phase). This non-noble metal system was reported to achieve a phenol yield of 13.6%. Zhu et al. [12] have reported a mpgC_3N_4-supported $H_3PW_{12}O_{40}$ catalyst for oxidative desulfurization of fuel (liquid-phase). It was shown that $H_3PW_{12}O_{40}$ is strongly immobilized on mpgC_3N_4 and that the catalyst exhibits very little deactivation after 15 cycles. No gas-phase oxidation has been reported for POM/C_3N_4 catalyst.

1.3 Motivation

In the literature reviewed, while nitrogen appears to play an important role by neutralization of some acidity of POMs and thus promoting selective oxidation pathways, these benefits of using nitrogen-containing carbon materials proposed are mostly based on a comparison with unsupported bulk POMs. A more rigorous comparison with a nitrogen-free carbon material can provide more information on the true contribution of having different nitrogen species in the support. Also, although some mechanisms for the interaction between POMs and nitrogen-containing carbon materials have been proposed, the nature of the POM-support interaction is still unclear.

Moreover, previous studies have tended to examine a fairly narrow range of nitrogen concentrations (N wt% < 15%, N atom% < 10%) that may not fully reflect the potential for utilizing basic supports. Therefore, an opportunity exists to use a wider nitrogen concentration range, and systematically study the effects of the support nitrogen content and nitrogen species distribution on the modification of the properties of POMs, including stability, dispersion, acid site population, acid site activity and oxidation activity.

By systematically studying the support effects, we can provide guidance in using supports to tune the properties of supported POMs other than changing the identity of its center/framework atom and counter cation, thus adding another degree of freedom to supported POM model catalysts. The information gained in this research will be useful for future catalyst design.

1.4 Research goals

The goal of this project is to answer the following three questions:

First, how does nitrogen-containing carbon material interact with POMs? To answer this question, two nitrogen-doped graphitic carbon samples, N-C-1000 (N atom% = 2%) and N-C-600 (N atom% = 19%), as well as the mesoporous graphitic carbon nitride (mpgC_3N_4, N atom% = 53%) were used as supports for POMs. Activated carbon (C) supported POM catalysts were also tested to serve as a rigorous nitrogen-free reference. The nitrogen content and nitrogen species distribution were thoroughly studied for the three nitrogen-containing materials and carefully relate to results from various characterization methods such as XRD to illustrate how the nitrogen-containing carbon materials interact with POMs.

Second, how strong are the interactions between POMs and this type of support? The strength of the interaction is represented by the H^+/POM ratio in this work, which comes from the results of ammonia temperature programmed desorption (NH_3 TPD) and butene chemisorption for POM supported on C, N-C-1000, N-C-600 and mpgC_3N_4. The H^+/POM ratios measured were compared to the theoretical H^+/POM ratio when no interaction is present to represent the strength of interaction between POMs and each support. The H^+/POM ratios were also compared across different supports groups at the same POM surface coverage level to relate the strength of interaction to nitrogen content as well as to the type of nitrogen species present in the support.

Third, can the interactions be used to control POM activity and selectivity? If so, How? POM supported on different nitrogen-containing carbon materials were tested in methanol oxidation and dehydration to answer this question. The methanol dehydration rate is used to represent the acid activity of the catalyst, whereas methanol oxidative dehydrogenation rate is used to characterize the oxidation activity of the catalyst. Kinetic models were constructed that describe the pathways of both methanol dehydration to form dimethyl ether and methanol oxidation to form formaldehyde, methyl formate and dimethoxymethane. By studying the change in kinetics parameters (rate constants, equilibrium constants) when switching to different supports, we can obtain insights on why using different supports can change the final product distribution, which is valuable information for future catalyst design.

1.5 Chapter summaries

1.5.1 Chapter 2: Preparation and Characterization of Nitrogen-containing Carbon Supported POM Catalysts

This chapter will discuss synthesis of nitrogen-containing carbon materials (N-C-1000, N-C-600 and mpgC_3N_4), preparation of POM catalysts using the as-synthesized materials as supports, as well as the tools and techniques used to characterize the supports and the catalysts. Nitrogen content and nitrogen species distribution in each support were studied in detail by XPS. Characterization results for C, N-C-1000, N-C-600 and mpgC_3N_4 supported POM catalysts are also presented, including Fourier transform infrared spectroscopy (FTIR) to confirm the stability of POMs and XRD/Scanning transmission electron microscopy (STEM) to check the dispersion state of POMs on these supports. XRD provided additional information about how the supports interact with POMs. NH_3-TPD and butene chemisorption results are reported for the strength and quantity of acid sites on these catalysts; thus an analysis of the strength of the interaction can be discussed. Overall, purpose of this chapter is to characterize the support materials, to confirm the stability and dispersion state of POMs on the support, and to understand the mechanism and result of the interaction between POMs and nitrogen-containing carbon materials.

1.5.2 Chapter 3: Nitrogen-containing Carbon Supported POM as Catalyst for Methanol Oxidation

Chapter 3 explores the behavior of POMs supported on different nitrogen-containing carbon materials as well as on carbon in methanol oxidation and dehydration. Reaction rates for both dehydration and oxidation products were analyzed for all the catalysts. Comparisons for catalysts with the same support were carried out to study the POM loading effect. Comparisons across catalysts with different supports were also performed at the same POM surface coverage level to study the support effect. Supports with higher nitrogen concentration lead to a decrease in both dehydration rates and oxidation rates, with dehydration rates dropping more dramatically. Therefore, it is possible to use the support effect to improve selectivity to oxidation products. N-C-600 catalysts showed the highest selectivity to oxidation products as well as highest selectivity to formaldehyde (about 80%).

1.5.3 Chapter 4: Kinetics and mechanistic details for methanol oxidation and dehydration

Chapter 4 studied in detail the kinetics for every product in methanol oxidation and dehydration. Kinetics experiments (varing total flow rate, partial pressure of reactants and co-feeding products) were conducted for two carbon-based and two N-C-600- based catalysts, to study the kinetic origin for both loading effect and support effect observed in Chapter 3. Mechanisms for every product were proposed based on the experimental results as well as knowledge from the literature. Mechanism-based rate equations were then derived, and kinetic models constructed based on the as-derived rate equations as well as the mass balance for the packed-bed reactor. The model prediction results and the experimental results were then compared to evaluate the models. Finally, the kinetic parameters were analyzed for all the four catalysts to provide insight on why support can affect the rate of dehydration and oxidation and the distribution of oxidation products.

1.5.4 Chapter 5: Conclusions and Recommended Future Directions

Chapter 5 includes the conclusions from this work as well as recommended possible future directions. In this chapter we summarize the nature of interactions between POM and nitrogen-containing carbon supports, the strength of the interaction in terms of H^+/POM ratio, the effect of this POM-support interaction in methanol dehydration and oxidation reactions, as well as the insights about support effects gained from kinetic studies. Also presented in this chapter are the potential new directions that include proposed DFT studies of the support effects, calorimetry experiments to measure adsorption energy for methanol on different supports, as well as possible liquid-phase reactions that could benefit from strong support-POM interactions to prevent leaching.

Chapter 2 Preparation and Characterization of Nitrogen-containing Carbon Supported POM Catalysts

2.1 Introduction

2.1.1 Methods to confirm stability and dispersion of supported POMs

The structural integrity of supported POM catalysts is usually confirmed by FTIR[26, 49, 50]. As introduced in Chapter 1, the structure of Keggin-type POMs ($XM_{12}O_{40}^{n-}$, ball-stick structure shown in Figure 2-1) contains one XO_4 tetrahedron surrounding by four M_3O_{13} sets formed by three edge-sharing octahedra (linked by M-O_c-M). The M_3O_{13} sets are linked together by bridging oxygen atoms (M-O_b-M). The FTIR spectrum of $H_3PMo_{12}O_{40}$ is dominated by four characteristic peaks at around 1050 cm^{-1} (P-O), 950 cm^{-1} (Mo=O_t), 880 cm^{-1} (Mo-O_b-Mo) and 740 cm^{-1} (Mo-O_c-Mo)[51]. The Mo-O_c-Mo mode has been shown to move to higher wavenumbers when the POM loading is decreased, possibly due to the absence of anion-anion interactions at low loadings[26, 51]. Polarization, perturbation from water molecules as well as anion-cation interactions can also lead to shift in FTIR peak positions. Other techniques such as Nuclear Magnetic Resonance[24] or Raman spectroscopy[20, 52] can also be used to confirm the intact structure of POMs.

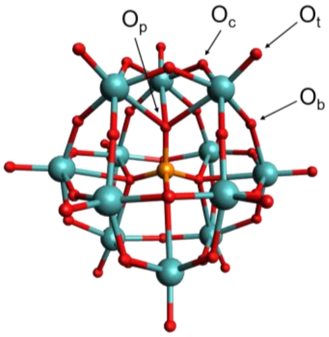

Figure 2-1. Keggin POM with the four types of oxygen labeled: P-O (O_p), corner (O_c), terminal (O_t), and bridging (O_b).

XRD and aberration-corrected scanning transmission electron microscopy high-angle annular dark field (STEM-HAADF) have been used in the literature to confirm the dispersion state of POMs on supports. The XRD for a dispersed POM catalyst should show no features of POM crystallites, which for $H_3PMo_{12}O_{40}$ are triclinic or tetragonal structures depending on the degree of hydration[53]. Small POM clusters of 2-3 molecules are also identifiable based on the literature, with a characteristic peak shown at about $2\theta = 7°$[54]. STEM-HAADF done by Barteau and co-workers for graphene-supported POMs has shown that individual POM molecules or small POM clusters can be clearly observed using this technique[26].

2.1.2 Methods to measure acid site population of supported POMs

The Iglesia group has developed a titration method with 2,6-di-*tert*-butylpyridine (DTBP) under reaction conditions to determine the quantity of Brønsted acid sites[24, 25, 55-58]. Acid site population can also be measured by butene chemisorption as shown by Seo and co-workers[59]. NH_3-TPD is often used for acid site strength measurement, where NH_3 (or other N-containing species) desorbing at higher temperature corresponds to sites with higher acid strength[60].

2.1.3 Interactions between POMs and nitrogen-containing carbons in the literature

For POMs on –NH_2 decorated carbon spheres and carbon aerogels, the Song group has suggested that during the loading process, the –NH_2 group could be protonated and act as the counter cation to anchor the negatively charged Keggin units[40]. For other nitrogen-containing carbon supports where both quaternary nitrogen and pyridinic nitrogen existed on the surface, the same researchers have proposed that the edge quaternary nitrogen species can be more easily converted into positively charged nitrogen group than pyridinic nitrogen, and thus could play an important part in immobilizing POMs[41]. Liu and co-workers synthesized POM/nitrogen-functionalized onion-like carbon hybrid catalysts. They observed in XPS an increase in graphitic nitrogen N1s signal with the increase of POM loading and concluded that POMs could bond to graphitic nitrogen through electrostatic interactions[43]. No interaction theory has been proposed for mpgC_3N_4 supported POM catalysts in the current literature.

2.2 Experimental

2.2.1 Support Preparation

2.2.1.1 N-C-1000 and N-C-600 synthesis

Surfactant P123, titanium tetraisopropoxide (TTIP), and H_2O were successively added to a solution containing ethanol and concentrated hydrochloric acid (HCl, 37%) and stirred at 40 °C for 12 h. Final molar ratios of TTIP/ P123/ HCl/ H_2O/ ethanol in the mixture were 1: 0.0135: 0.52: 16:40. 2.8g dicyandiamide was then added to the as-formed dispersion and dried at 40°C overnight. The dried white powders were heated at 5°C·min^{-1} to 1000 °C (for N-C-1000) and 600°C (for N-C-600) under N_2 flow and maintained at the fixed temperature for 1 h. After cooling to room temperature, the as-formed black powder was etched with an excess amount of

HF solution (20%) to remove TiN and TiO_2 components. After etching, the sample was further washed with water and ethanol and dried at 60°C overnight. The sample was then calcined at 300 °C in air for 30min before POM loading. Synthesis of both N-C-1000 and N-C-600 are performed by the Jie-Sheng Chen lab at Shanghai Jiao Tong University[61].

2.2.1.2 mpgC_3N_4 synthesis

50 g of cyanamide (Fisher) was dissolved in 156.3 g of Ludox HS40 solution (dispersion of 12 nm SiO_2 particles with 40 wt% in water, Fisher). After all the cyanamide dissolved, ethanol (500ml) was added to the solution to form a gel. The as-formed gel was then heated in air at 550 °C for 4 h (ramp: 2.3°C min^{-1}). The resulting powder was treated with 4 M HF acid to remove the silica template[62]. After etching, the powders were washed with distilled water and then ethanol using vacuum filtration. Finally, the powders were dried at 60°C under vacuum overnight and was calcined at 300 °C in air for 30min before POM loading.

2.2.2 POM deposition procedure

Keggin-type acid polyoxometalates ($H_3PMo_{12}O_{40}\cdot xH_2O$ and $H_3PW_{12}O_{40}\cdot xH_2O$, Fisher) were deposited on activated carbon (C, Darco G-60 from Sigma Aldrich, calcined at 300 °C in air for 30 min before POM loading), N-C-1000, N-C-600 and mpgC_3N_4 by incipient wetness from aqueous solution. The as-obtained samples were dried in air at 60°C overnight. A wide loading range (4-50wt%) was adopted on each support. As an example, a 0.107M $H_3PMo_{12}O_{40}$ solution was used to impregnate C (pore volume 0.59ml/g) with 15 wt% $H_3PMo_{12}O_{40}$, denoted as HPM-15/C. Because the surface areas of these four supports are different, we compare catalysts with similar polyoxometalate (POM) surface densities. Following previous examples [29], a density of 0.88 POM/nm^2 was taken as monolayer coverage. For example, for the HPM-15/C catalyst, the surface POM coverage on the 942m^2/g carbon support was calculated to be 0.06 POM/nm^2.

Although all catalysts are labeled with their HPM loading (wt%), it is useful also to group them by surface coverage when comparing reaction behavior. Table 2-1 lists the catalysts that fall into three characteristic POM coverage ranges.

Approximate surface coverage	Calculated range of surface coverage	Catalysts
0.04 POM/nm^2	0.034-0.042 POM/nm^2	HPM-10/C, HPM-15/N-C-1000, HPM-7/N-C-600, HPM-2/mpgC_3N_4
0.06 POM/nm^2	0.049-0.063 POM/nm^2	HPM-15/C, HPM-20/N-C-1000, HPM-10/N-C-600, HPM-3/ mpgC_3N_4
0.09 POM/nm^2	0.084-0.098 POM/nm^2	HPM-20/C, HPM-30/N-C-1000, HPM-15/N-C-600, HPM-4/ mpgC_3N_4

Table 2-1. Catalysts grouped by approximate POM surface coverage

2.2.3 Catalyst Characterization

All the characterization for the supports shown in this thesis were carried out after the 300°C calcination step. BET specific surface areas and pore volumes for each material were determined by N_2 physisorption using a Micromeritics ASAP 2020 automated system. XPS was used to analyze the composition and nature of nitrogen-containing carbon materials using a Kratos axis ultra XPS with a monochromated Al Kα source. The binding energy of the Au $4f_{7/2}$ peak at 84 eV was used for calibration. Elemental analysis was performed by Atlantic Microlab, Inc. to determine the N concentration in the bulk structure. XRD measurements were performed on a Rigaku MiniFlex 600 Table-top X-ray Diffractometer with Cu Kα (λ=1.5406 Å) radiation in the range of $5 \leq 2\theta \leq 32.5^{\circ}$. α-SiC (99.8% from Alfa Aesar) was used as an internal standard in XRD studies. Attenuated total reflectance (ATR) FTIR measurements were performed on a Nicolet iS50 spectrometer equipped with a DTGS detector and an ATR diamond sampling station.

Typically, 128 scans were accumulated with a resolution of 4 cm^{-1}. STEM-HAADF images were obtained with JEOL JEM2100F electron microscope.

Butene chemisorption was used to measure the acid site population on the supported POM catalysts. The chemisorption was performed on a TA Instruments SDTQ600 TGA with a quartz-lined QGA furnace, modified with a custom gas manifold to provide pretreatment with reactive gases. The samples were pretreated at 220°C for 0.5h in 90sccm air and then cooled to 60°C in air. Mass was recorded when it stabilized (m_0). Then flow was switched to 90sccm 1% 1-butene in N_2 and the mass increase was monitored until saturated, typically for 0.5 hour. The samples were then purged in He overnight, and final mass (m_f) was recorded when it is stabilized. Adsorption was assumed to be irreversible at 60°C) and the butene/H^+ was assumed to be 1:1. Then the initial mass (m_i) and final mass (m_f) can be used to calculate the H^+/POM ratio based on Equation 2-1.

Equation 2-1: H^+/POM ratio calculation based on results from butene chemisorption.

$$\frac{H^+}{POM} = \frac{(m_f - m_0)}{\Delta MW \cdot N_{POM}}$$

NH_3-TPD was also used to gather information about the acid sites on the catalysts (acid site population as well as acid strength). It was conducted using a Micromeritics AutoChem II 2920 chemisorption instrument equipment with a mass spectrometer (Balzers ThermoStar) according to procedures presented by Song and co-workers[41]. Catalyst samples were loaded into a U-shaped quartz tube, pretreated in 20 sccm He at 220˚C for 30 min and cooled back to room temperature. Then the He flow was switched to 5 sccm, and NH_3 was pulsed in with a 0.5 mL loop until the TCD signal of two consecutive pulses did not change anymore. The sample was then heated to 100˚C in 5 sccm He and kept for 1 hour. Finally, the catalyst was cooled to room temperature, and then heated in 10 sccm He to 800 ˚C at 5˚C/min. Following every run, pure NH_3 and pure N_2 were pulsed into mass spectrometer to calibrate NH_3 (mass 16 and mass 17) and N_2 (mass 28 and mass 14) in the mass spectrometer.

2.3 Results

2.3.1 Support surface area and pore volume

The surface areas and pore volumes of the supports are listed in Table 2-2. The surface areas were very different among the four supports, with mpgC_3N_4 being the lowest (163m^2/g) and N-C-1000 being the highest (1692m^2/g). Although the packing of POMs can vary with different structures, degrees of cation exchange, hydration and support[27, 63], we have used a standard value for monolayer coverage of 0.88 POM/nm^2 [29] to facilitate comparison between the supports in this study that exhibit this wide range of surface areas. This value is based on a van der Waals diameter of 1.2 nm[64].

	Surface area (m^2/g)	**Pore volume (cm^3/g)**
C	942	0.9
N-C-1000	1692	0.29
N-C-600	591	0.59
mpgC_3N_4	163	0.44

Table 2-2. Surface area and pore volume of the supports.

2.3.2 Support XPS

The XPS survey scans and the composition analyses of N-C-1000, N-C-600 and mpgC_3N_4 are shown in Figure 2-2 (a-c) and Table 2-3 respectively. All three materials are composed of mainly C and N, with less than 5% O. Among the three, N-C-1000 has the lowest N concentration (2 atom%) due to the very high carbonization temperature (1000°C) applied during the synthesis. N-C-600 contains more nitrogen (19 atom%) than N-C-1000 because of the lower carbonization temperature (600°C). mpgC_3N_4 has the largest N% (53 atom%), which is consistent with its ideal stoichiometric value (57 atom%). Table 2-3 also shows the N:C ratios from CHN analysis of the N-C-600 and mpgC_3N_4 samples, demonstrating that the surface region of both materials is moderately depleted in N relative to the bulk.

Further deconvolution of N 1s spectra is shown in Figure 2-2 (d-f), illustrating the N-species distribution in the nitrogen-containing carbon supports. Among the three supports, mpgC_3N_4 provides the most straightforward analysis because of its more organized structure, see Figure 2-2(g). As shown, with a heptazine repeating unit[65], mpgC_3N_4 has four different kinds of nitrogen, designated N1, N2, N3 in the perfect C_3N_4 structure, as well as amine sites formed at defects. According to this structure, we have assigned the peak at 401.3eV to N1 (analogous to graphitic nitrogen, $N_{\text{Graphitic}}$), 400.2eV to both N2 and the amine groups and 398.8eV to N3 (analogous to pyridinic nitrogen, $N_{\text{Pyridinic}}$). This is in agreement with previous polyemeraldine XPS assignments by Tan[66], that of 3, 5, 11, 13-tetraazacycl[3, 3, 3]azine XPS by Boutique et al[67], as well as the theoretical and experimental studies of nitrogen-containing carbon materials[68-70]. The analysis of N-C-1000 and N-C-600 is more complicated, but it can be seen that they mainly contain graphitic nitrogen ($N_{\text{Graphitic}}$), pyrrolic nitrogen (N_{Pyrrolic}) and pyridinic nitrogen ($N_{Pyridinic}$)[68-70]. Meanwhile, similar to $mpgC_3N_4$, some amine groups were present on the surface of N-C-600, positioned at 399.8eV.

	O	C	N	N/C (surface)	N/C (bulk)
N-C-1000	5%	93%	2%	0.02	-
N-C-600	5%	76%	19%	0.25	0.34
$mpgC_3N_4$	3%	44%	53%	1.20	1.45

Table 2-3. XPS survey results for N-C-1000, N-C-600 and $mpgC_3N_4$. Compositions are given as at%. Bulk N/C ratio are obtained from CHN analysis.

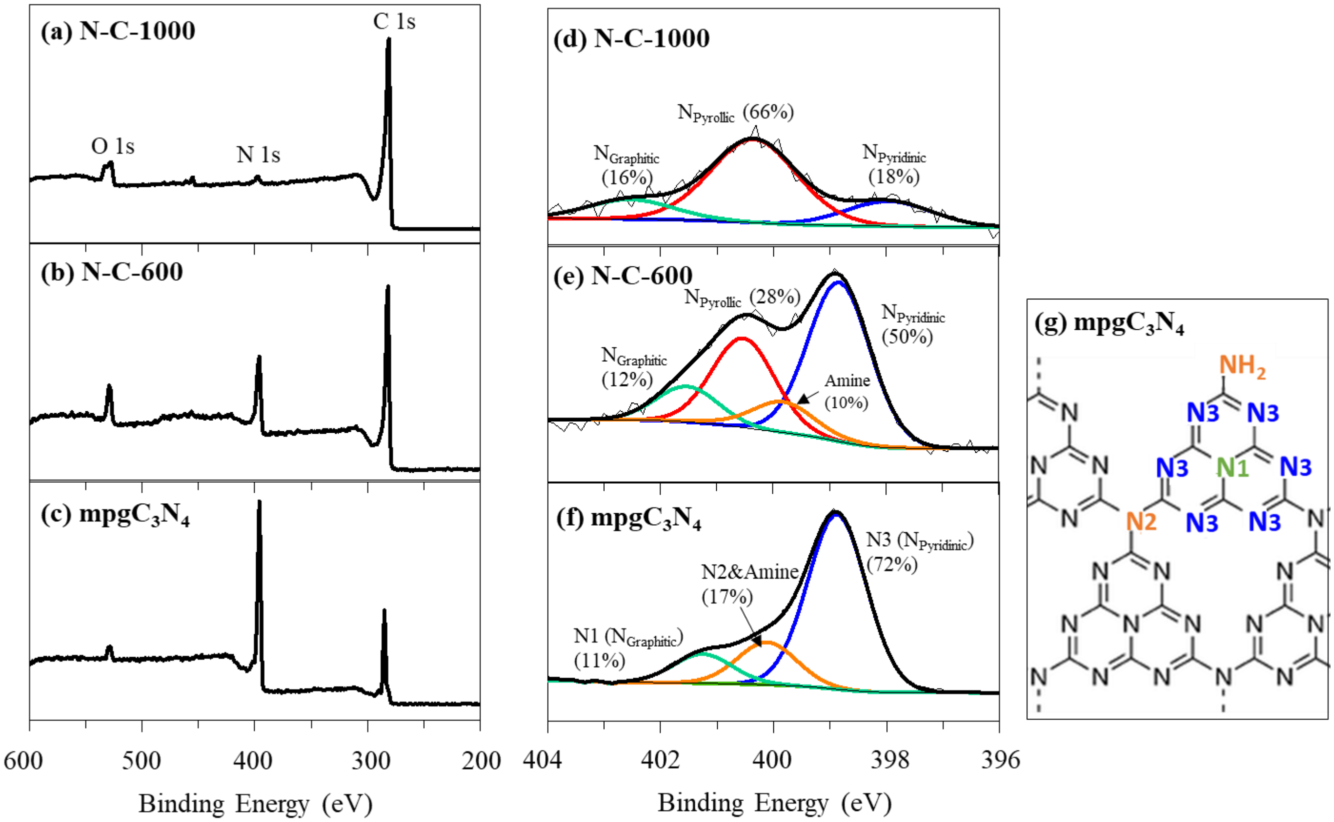

Figure 2-2. Survey scans of (a) N-C-1000, (b) N-C-600, (c) $mpgC_3N_4$; N 1s peak deconvolution of (d) N-C-1000, (e) N-C-600, (f) $mpgC_3N_4$; (g) structure of $mpgC_3N_4$.

2.3.3 FTIR

ATR-FTIR spectra were used to confirm the stability of the polyoxometalate framework in the supported POM catalysts (Figure 2-3). With the bulk HPM spectra shown at the bottom of each panel in Figure 2-3 as a reference, the four main framework vibrational modes of the Keggin ion in the range of 650-1100cm^{-1} are apparent in all spectra[51]. Besides the characteristic peak for HPMs, for HPM-40/N-C-600, an extra peak at around 1400cm^{-1} for $(NH_4)_3PMo_{12}O_{40}$ (NH_4PM)[71] is observed, which agreed with the NH_4PM spectra at the bottom of the spectra. This is consistent with the NH_4PM peak observed in XRD for the N-C-600 and mpgC_3N_4 based catalysts, which will be discussed in detail in Section 2.3.4. The IR spectrum of mpgC_3N_4 in this region has a large number of features due to the aromatic carbon nitrogen heterocycles[72]; thus, a similar vibrational fingerprint for NH_4PM on this material could not be discerned.

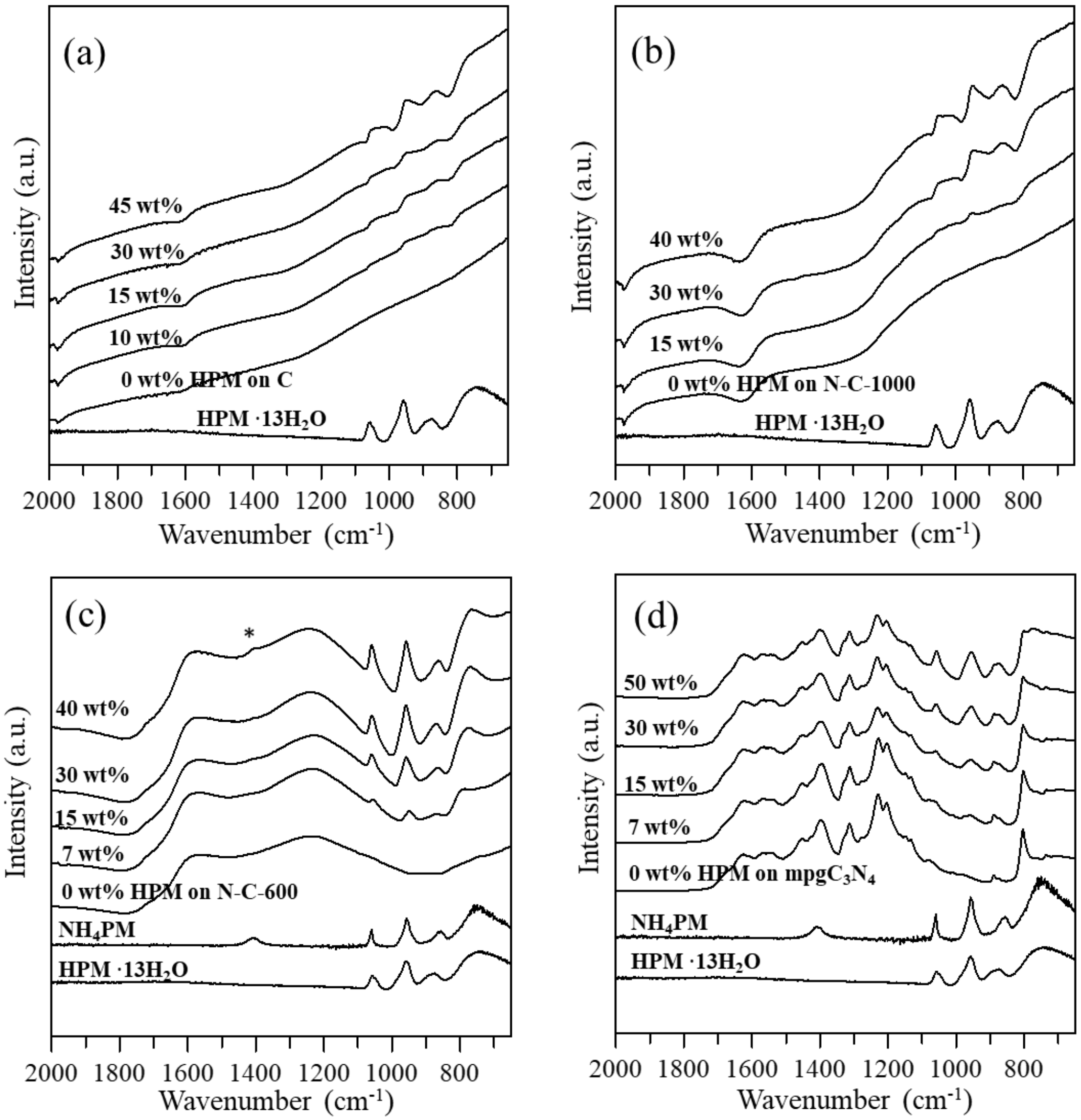

Figure 2-3. ATR-FTIR spectra for (a) 0, 10, 15, 30, 45wt% HPM on C; (b) 0, 15, 30, 40wt% HPM on N-C-1000; (c) 0, 7, 15, 30, 40wt% HPM on N-C-600; (d) 0, 7, 15, 30, 50wt% HPM on mpgC_3N_4. HPM and NH_4PM spectra are shown as reference.

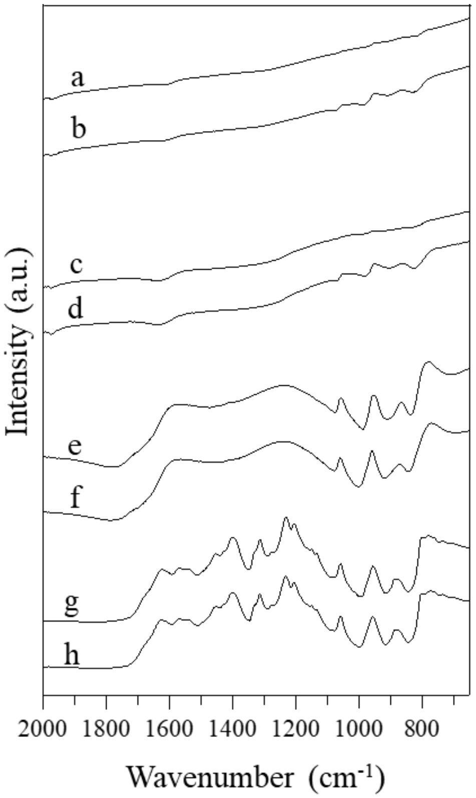

Figure 2-4. ATR-FTIR spectra of HPM-50/C (a) after and (b) before washing, HPM-50/N-C-1000 (c) after and (d) before washing, HPM-30/N-C-600 (e) after and (f) before washing, HPM-50/mpgC_3N_4 (g) after and (h) before washing

To have a general ideal of how strong the HPMs are attached to the supports, water-washing experiments were performed. The catalysts were stirred in water at 600rpm for 3 hours, then filtered and dried before FTIR was taken again. Results were shown in Figure 2-4. For C and N-C-1000 supported catalysts, the signal for POM peaks became much weaker after washing, suggesting that some HPMs have been washed off. This is consistent with literature on C-supported HPMs, which suggests that POMs can only be strongly adsorbed to activated carbon at low loading (below 10wt%)[8]. For N-C-600 and mpgC_3N_4 supported catalysts, the signals remained very strong after the washing experiments, suggesting that the interaction between

HPMs and these two supports are strong even at very high HPM loadings (30 wt% for N-C-600 and 50% for mpgC_3N_4).

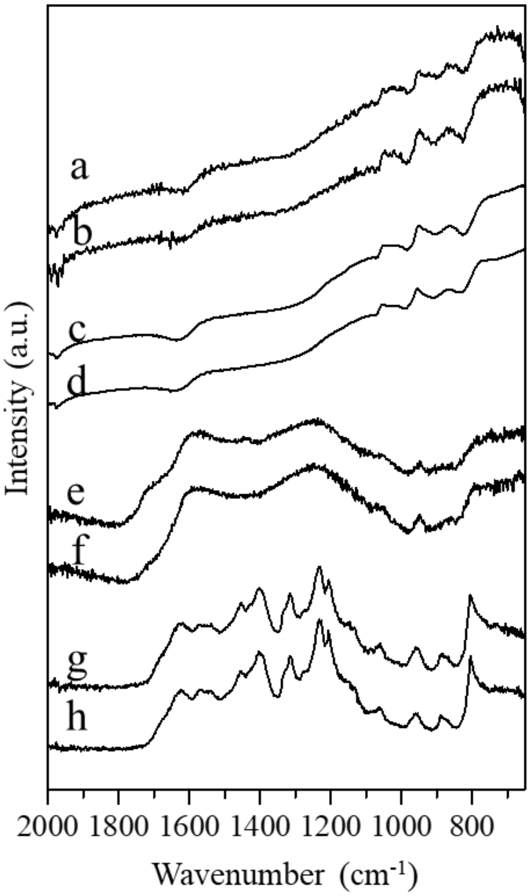

Figure 2-5. ATR-FTIR spectra of HPM-30/C (a) after and (b) before methanol oxidation reaction at 220°C, HPM-40/N-C-1000 (c) after and (d) before reaction, HPM-7/N-C-600 (e) after and (f) before reaction, HPM-15/mpgC_3N_4 (g) after and (h) before reaction

Examples of FTIR spectra for catalysts before and after methanol oxidation are shown in Figure 2-5 (reaction results are discussed in Chapter 3 and Chapter 4). As shown in the figure, the four characteristic POMs can be observed for the after-reaction catalysts, indicating that POMs are intact after reaction.

2.3.4 XRD

The XRD patterns of HPM/C and HPM/N-C-1000 with different HPM loadings/ surface coverages are shown in Figure 2-6. The XRD pattern for HPM·8H_2O crystallites, consistent with previous literature results[73], is shown at the bottom of each panel for reference. As shown in Figure 2-6(a), the HPMs were well dispersed on C at loadings up to 30wt%, which corresponds to 0.16 POM/nm^2 on this support. Only when the loading reached 35wt% (0.22 POM/nm^2) was there evidence (peak at $2\theta = 8°$) of HPM crystallite formation. Therefore, the maximum loading of HPMs on carbon that can be achieved without crystallite formation is between 0.16 and 0.22 POM/nm^2. N-C-1000 showed a similar ability to disperse HPMs. HPM·8H_2O crystallites started to appear in samples with loadings corresponding to between 0.13 and 0.23 POM/nm^2, as shown in Figure 2-6(b).

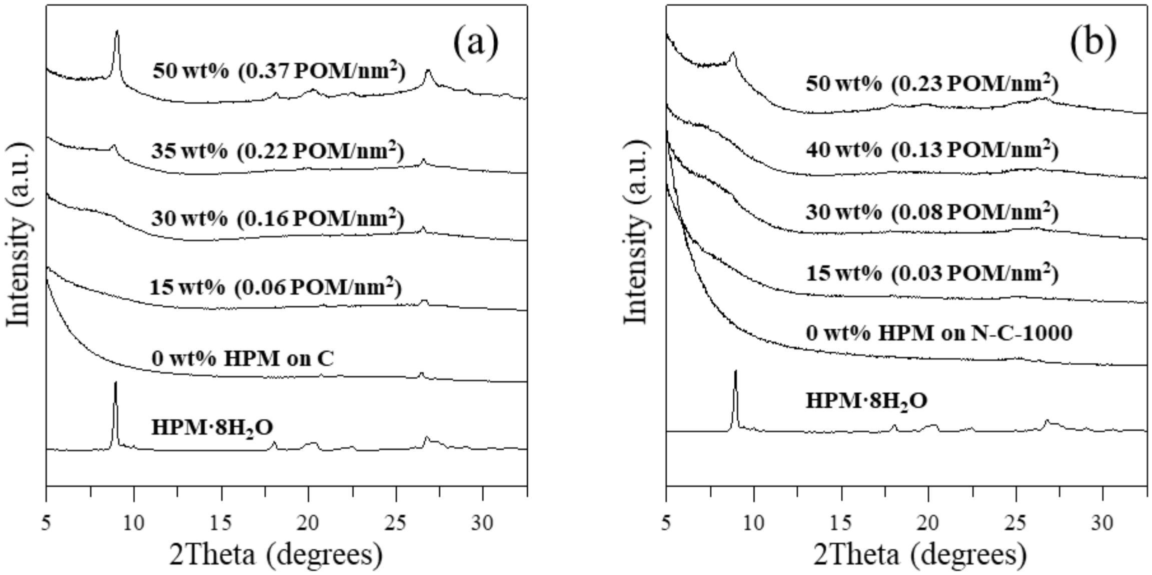

Figure 2-6. XRD pattern of (a) 0, 15, 30, 35, 50wt% HPM on C; (b) 0, 15, 30, 40, 50wt% HPM on N-C-1000.

The XRD patterns are quite different in the case of HPM supported on the materials with higher nitrogen content, N-C-600 and mpgC_3N_4. As shown in Figure 2-7(a), as the HPM loading was increased on N-C-600 from 10wt% to 30wt%, diffraction peaks for $(NH_4)_3PMo_{12}O_{40}$ (cubic structure, main peak at 26.4°, consistent with previous literature[74]) appeared instead of $H_3PMo_{12}O_{40}$, which does not exhibit a similar pattern regardless of its degree of hydration[53]. This suggests that the -NH_2 groups on the support were extracted by HPM deposition to form the ammonium salt. This process must involve removal of nitrogen from the support, or else 3-dimensional crystallites of the ammonium salt would not be formed. At higher loadings, e.g., 40 wt% HPM on N-C-600, small peaks for HPM·28H_2O (in the 5-10°, 25-30° area) started to appear, indicating that the -NH_2 from the N-C-600 surface had been exhausted. NH_4PM was also formed with the HPM/mpgC_3N_4 system as shown in Figure 2-7(b), but only at the highest loading, 50wt%. This further supports the relationship between surface -NH_2 and the NH_4PM formation, because, as demonstrated in XPS, mpgC_3N_4 also contains defect amine groups on the support surface.

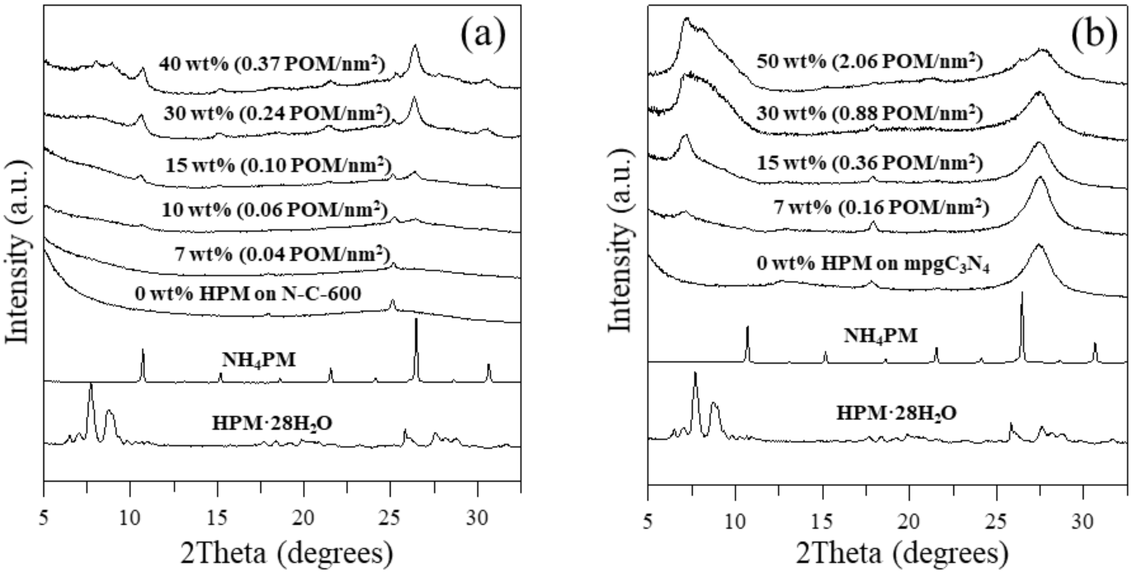

Figure 2-7. XRD patterns for (a) 0, 7, 10, 15, 30, 40wt% HPM on N-C-600; (b) 0, 7, 15, 30, 50wt% HPM on mpgC_3N_4. Diffraction pattern for NH_4PM and HPM·28H_2O is shown at the bottom of each figure for comparison.

However, despite the fact that both supports give rise to NH_4PM crystallite formation, there is a significant difference between N-C-600 and mpgC_3N_4 in their ability to disperse HPMs. With N-C-600, as shown in Figure 2-7(a), NH_4PM crystallites appeared at very low loadings, 10wt% (0.06 POM/nm^2), and the area of the crystallite peaks continued to increase as HPM loading increased until the -NH_2 groups were consumed. In contrast, with mpgC_3N_4, for 30wt% HPM, which corresponds to 0.88 POM/nm^2 (monolayer coverage), the HPMs remained dispersed on the surface with no evidence for crystallite formation by the parent POM or its ammonium salt. Even when the loading reached 50wt%, which corresponds to more than two layers (2.06 POM/nm^2), the NH_4PM crystallite peaks in XRD were still very small. The most prominent peak for the HPM/mpgC_3N_4 system was a lower angle peak at around 7°, and it continued to increase with HPM loading. This peak is assigned to the dispersed HPMs or clusters of 2-3 HPM molecules according to previous literature[54].

To further estimate the amount of NH_4PM crystallites formed after loading HPM, we used α-SiC as a standard and performed XRD on the as-synthesized supported HPM samples (HPM-30/N-C-600 and HPM-50/mpgC_3N_4) as well as physical mixtures of NH_4PM and corresponding supports. Ammonium phosphomolybdate (Strem Chemicals) and silicon carbide (alpha-phase, 99.8% (metals basis), Alfa Aesar) were used to make physical mixtures in comparative XRD. The results are shown in Figure 2-8 and Figure 2-9 for N-C-600 and mpgC_3N_4 respectively. Figure 2-8(a) presents the XRD pattern for a physical mixture of 30wt% NH_4PM with N-C-600, which is a good indicator of how much ammonium salt should appear in XRD if all the HPM loaded on

N-C-600 were transformed into NH_4PM in the sample HPM-30/N-C-600. Figure 2-8(b) shows the XRD pattern of HPM-30/N-C-600 for comparison. Because crystallite size affects both the width and height of the diffraction peaks, rigorous calibration is not possible. However, by integrating the area of the NH_4PM peaks at 10.6°, 21.3° and 30.5° for both HPM-30/N-C-600 and the physical mixture, one can make a rough estimate of the relative contributions of NH_4PM crystallites to the diffraction patterns of each. For HPM-30/N-C-600 we estimate that about 30% of the POM loaded is converted to crystalline NH_4PM by reaction with amine groups on the N-C-600 support. For HPM-50/mpgC_3N_4 the corresponding value is about 3%, based on analysis of the diffraction peak at 26.3°.

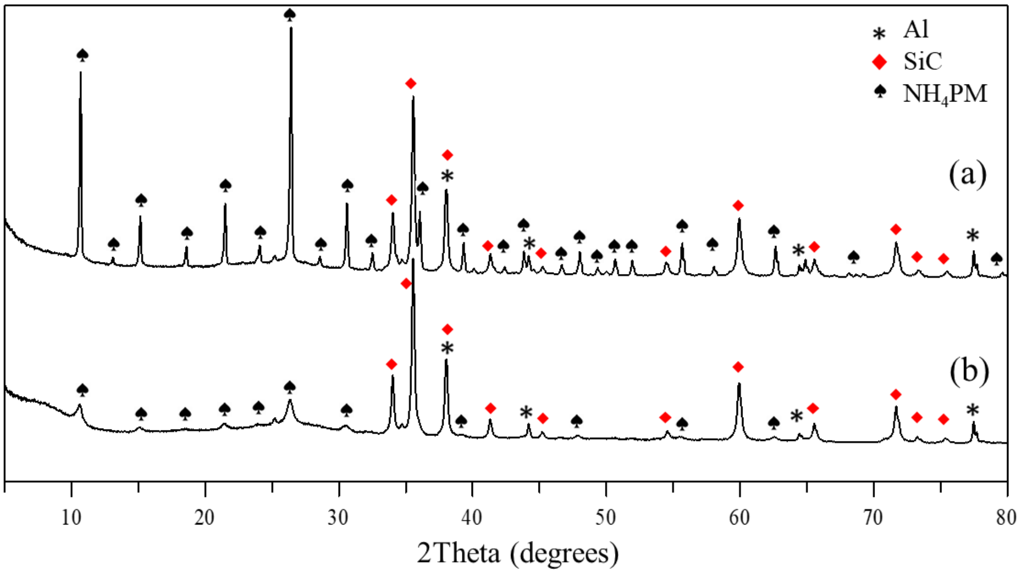

Figure 2-8. Comparative XRD using α-SiC as standard: (a) physical mixture of 30wt% NH_4PM with N-C-600; (b) HPM-30/N-C-600. Both samples contained the same concentration of SiC (41 wt%). The two spectra were normalized to the same SiC peak height. Aluminum peaks are from the sample holder.

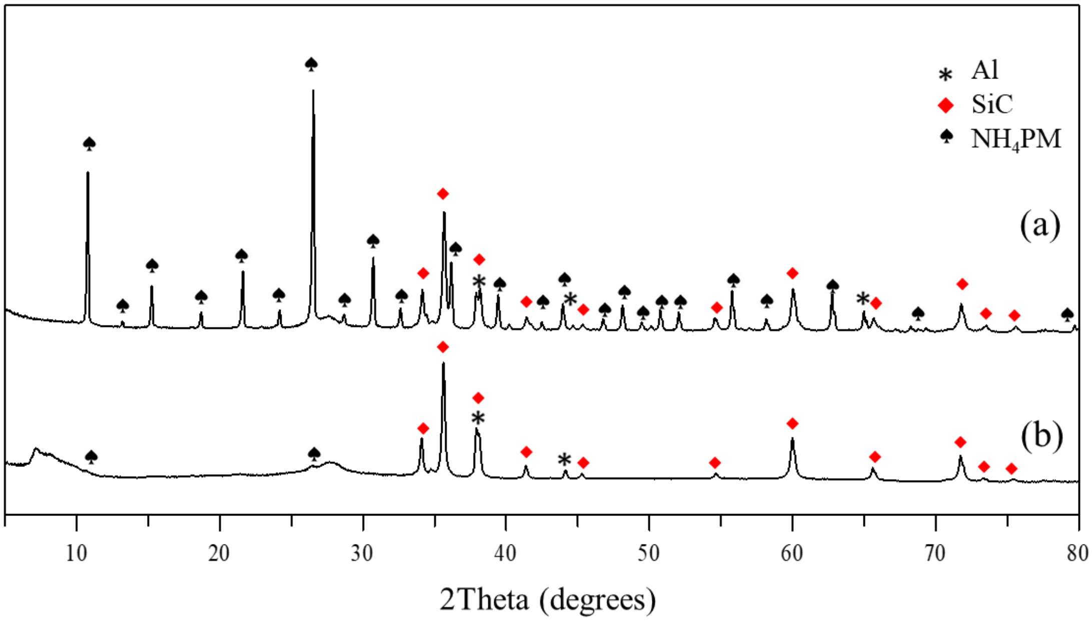

Figure 2-9. Comparative XRD using α-SiC as standard: (a) physical mixture of 50wt% NH_4PM with mpgC_3N_4; (b) HPM-50/ mpgC_3N_4. Both samples contained the same concentration of SiC (41 wt%). The two spectra were normalized to the same SiC peak height.

Different loadings of $H_3PW_{12}O_{40}$ on the four supports were also prepared and examined by XRD. Similar trends, including the correlation of -NH_2 and ammonium salt formation and the proficiency of mpgC_3N_4 at dispersing HPWs, were observed. As shown in figure 2-10 (a), for HPW-15/N-C-600 and HPW-30/N-C-600 catalysts, $(NH_4)_3PW_{12}O_{40}$ (NH_4PW) peaks were observed instead of HPW, meaning that the amino groups on N-C-600 are again pulled off from the support. A very weak NH_4PW peak was observed for HPW-15/mpgC_3N_4 and HPW-30/mpgC_3N_4 at about 26.8°, which is a little different from the HPM/mpgC_3N_4 data where the NH_4PM crystallites did not show up until 50wt%. However, this is consistent with literature, which showed that the loading threshold for HPW crystallite formation is always lower than that for HPM. Nevertheless, NH_4PW peaks were very small for both HPW-15/mpgC_3N_4 and HPW-30/mpgC_3N_4 and the low angle peak did appear in Figure 2-10(b) as the HPW loading went up, so most HPWs are still dispersed or in very small clusters on the surface of mpgC3N4 even up to high loading of 30wt%.

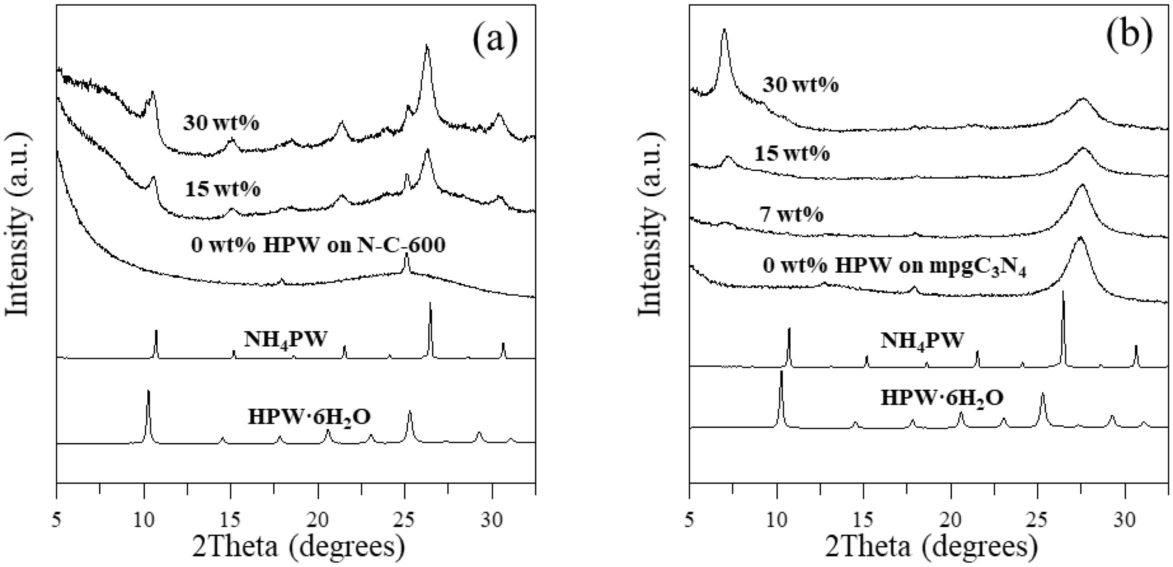

Figure 2-10. XRD patterns for (a) 0, 15, 30wt% HPW on N-C-600; (b) 0, 7, 15, 30 HPW on $mpgC_3N_4$. Diffraction pattern for NH_4PW and $HPW·6H_2O$ is shown at the bottom of each figure for comparison.

2.3.5 STEM-HAADF

Aberration-corrected STEM-HAADF was performed to help visualize the dispersion state of HPMs on the four supports. Since the atomic numbers of carbon (Z=6) and nitrogen (Z=7) are very different from molybdenum (Z=42), the molybdenum-containing POMs can be distinguished from the support as bright spots in STEM-HAADF images. As shown in Figure 2-11(a-d), bright features of 1.1 to 2.4 nm are apparent in all images. The lower end of this range is as expected for molecularly dispersed POMs; the upper end of the distribution may reflect clusters of ~ 3 POMs. However, since this technique does not resolve depth well, the larger features may also include contributions from multiple layers of the sample. Thus, these results are in good agreement with the XRD results that showed low angle peaks indicative of some 2-D cluster formation, but no crystallite formation at the loadings characteristic of most of the samples in Figure 2-11. Even in the case of HPM-15/N-C-600, see Figure 2-11(c), for which there is evidence in XRD of crystallite formation, most POMs are still dispersed molecularly or in small clusters on the support.

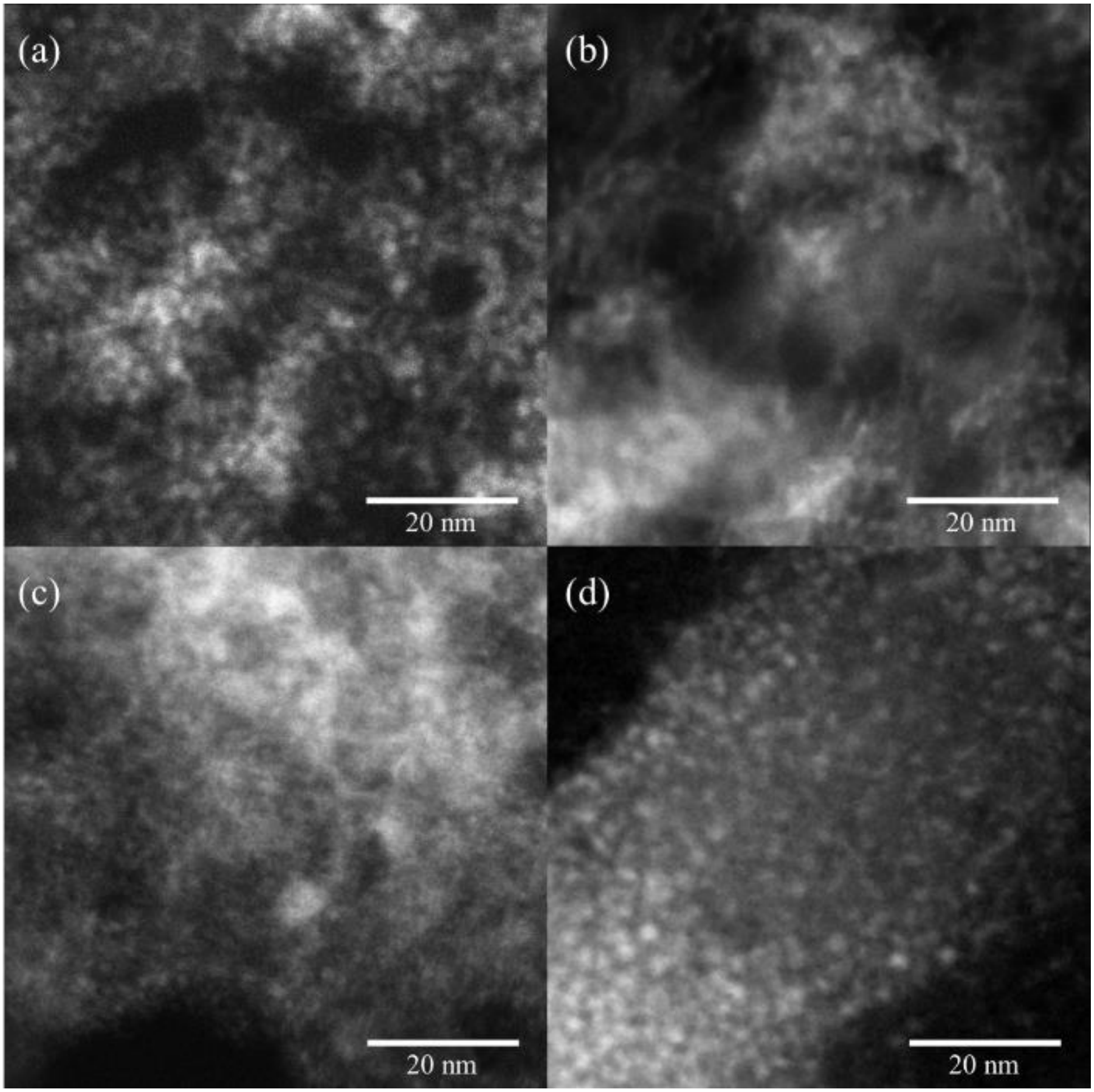

Figure 2-11. STEM-HAADF image of (a) HPM-10/C; (b) HPM-20/N-C-1000; (c) HPM-15/N-C-600; (d) HPM-7/ mpgC_3N_4.

2.3.6 NH_3-TPD

NH_3-TPD was used to measure acid site population and acid strength for C and N-C-600 supported catalysts. For C-supported HPM catalyst, NH_3-TPD of both catalyst and support were taken. Taking HPM-10/C as an example, the raw data from mass spectrometer for both HPM-10/C and C are shown in Figure 2-12. As shown in the figure, carbon itself can adsorb a small amount of NH_3, meaning that it has a small amount of weak acid sites on the surface. This support contribution will be subtracted from the NH_3 signal of HPM-10/C to get the amount of NH_3 that is adsorbed by only HPMs. No other N-containing species were observed during the TPD for HPM-10/C and C. NH_3 signal are based on the mass spectrometer signals for mass 17.

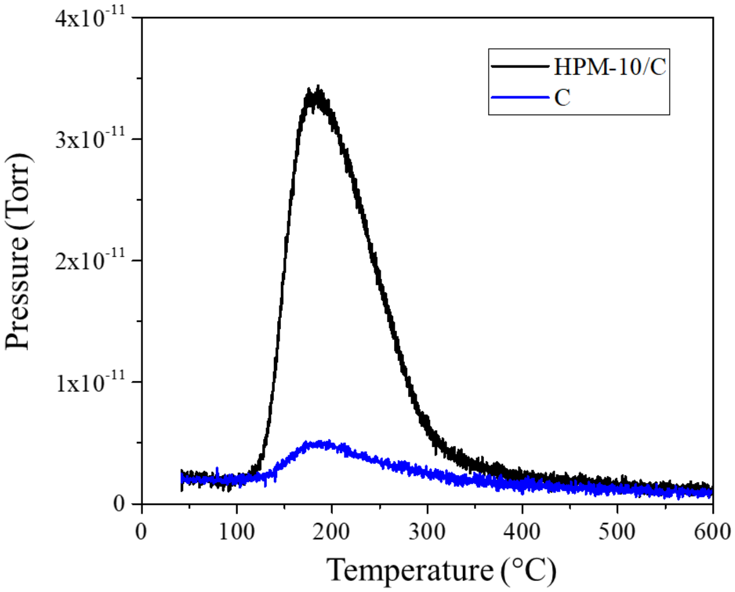

Figure 2-12. Mass spectrometer signals for NH_3-TPD from HPM-10/C and C. NH_3 was monitored using mass 17. Both spectra were based on same amount of support mass.

The NH_3-TPD data (support contribution subtracted) for HPM-7/C, HPM-10/C, HPM-15/C, HPM-20/C and HPM-30/C are shown in Figure 2-13 and Figure 2-14, where NH_3 signal based on mass 17 is shown in Figure 2-13 and N_2 signal based on mass 14 is plotted in Figure 2-14. As is demonstrated in the Figure 2-13, for HPM-7/C, HPM-10/C, HPM-15/C and HPM-20/C, NH_3 desorbed between 120 and 350˚C, the peak area increases with HPM loading and also shifted slightly to higher temperature. However, for HPM-30/C, the peak area between 120 and 350°C decreased compared to HPM/C with low loadings and an additional peak at 400°C appeared. In the meantime, a N_2 peak at 400°C was also observed, as shown in Figure 2-14, whereas the N_2 peak for HPM-20/C was very small (at about 300°C) with no N_2 peak for HPM/C catalyst with loadings lower than 20wt%. This indicates that the acid strength for some of the protons in HPM-30/C is higher than the other HPM/C catalysts with lower loadings, possibly because small clusters of POMs existed in this catalyst whereas in the low loading ones the POMs are molecularly dispersed. The integration result of the peaks (from both NH_3 and N_2) is shown in Table 2-4.

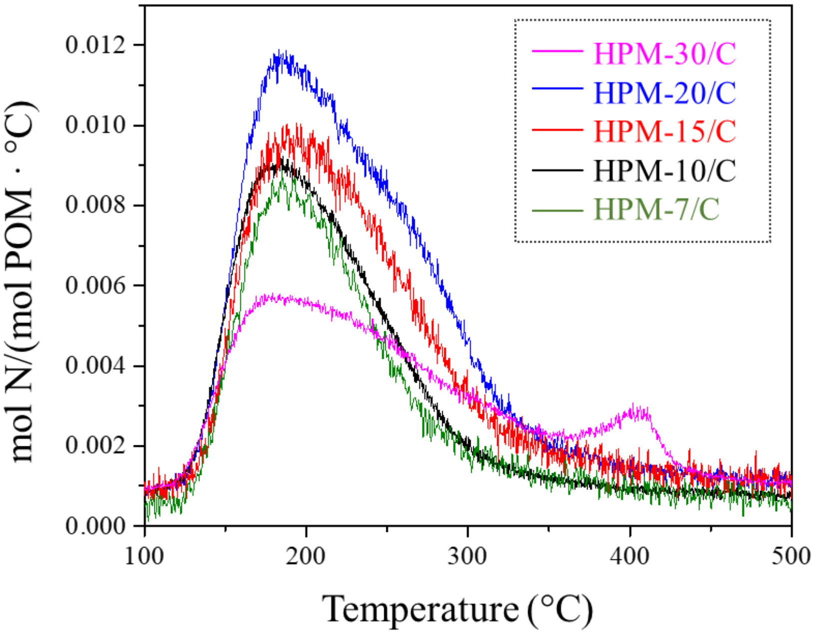

Figure 2-13. NH_3 desorption signal (in mol N/(mol POM · °C)) based on mass 17 for HPM-7/C, HPM-10/C, HPM-15/C, HPM-20/C and HPM-30/C. Support (C) signal has been subtracted.

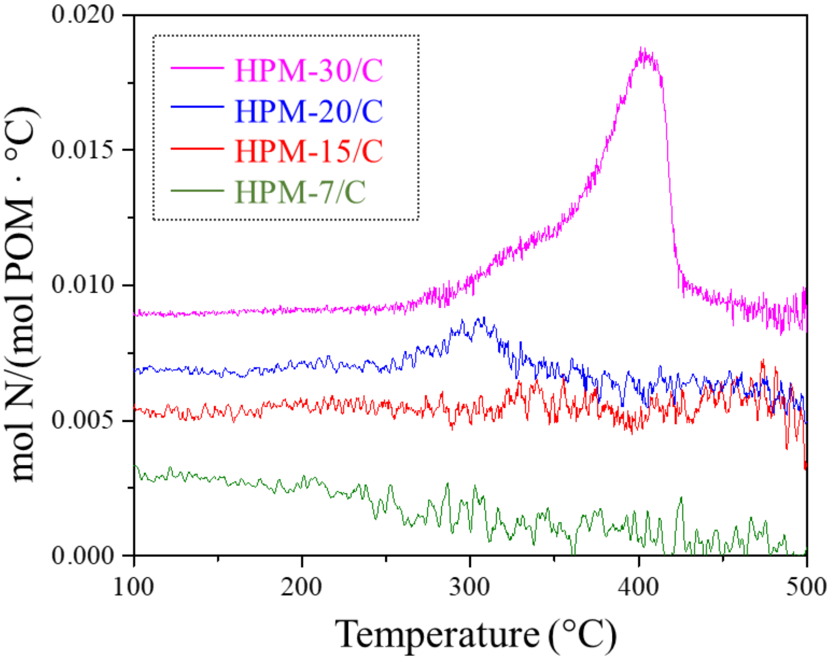

Figure 2-14. N_2 desorption signal (in mol N/(mol POM · °C)) based on mass 14 for HPM-7/C, HPM-15/C, HPM-20/C and HPM-30/C.

Catalyst	Calculated H^+/POM ratio		
	from NH_3 peak	from N_2 peak	total
HPM-7/C	0.82	0	0.82
HPM-10/C	0.9	0	0.9
HPM-15/C	1.11	0	1.11
HPM-20/C	1.32	0.03	1.35
HPM-30/C	0.82	0.58	1.4

Table 2-4. Calculated H^+/POM ratio based on the integration result of NH_3 and N_2 peaks in NH_3-TPD.

For N-C-600 supported catalysts, a TPD procedure without the NH_3 adsorption step was performed first to get an idea of how much NH_3 or other N species (e.g. N_2) would come off from the N-C-600 support or N-C-600 supported catalysts themselves. As is shown in the Figure

2-15(a), N-C-600 itself can emit a large amount of NH_3 in the temperature range of 400-700°C, which could come from breaking of C-N bond for the amino groups on the surface of N-C-600. A rough estimate based on the integration of the peak gives a density of $2.2*10^{20}$ $-NH_2$ per gram N-C-600. This is consistent the $-NH_2$ density result calculated with XPS result ($4.9*10^{20}$ $-NH_2$ per gram N-C-600), if we assume a surface atom density of $3.6*10^{19}$ $/m^2$ for N-C-600.

After HPMs were loaded on N-C-600 however, take HPM-7/N-C-600 for example, the peak that may correspond to $-NH_2$ decreased dramatically, while in the meantime we see a big increase in the N_2 emission of the sample. This simultaneous decrease in NH_3 and increase in N_2 can be interpreted as the $-NH_2$ groups interacting very strongly with HPM, so instead of coming off as NH_3 they came off oxidized to N_2. For HPM-30/N-C-600, the shape of N_2 peak is different from that of HPM-7/N-C-600, a sharp peak at around 600°C was observed. This can be attributed to NH_4PM crystallite formation observed in XRD for this sample, because the same sharp peak appears in the TPD result of bulk NH_4PM at similar temperature.

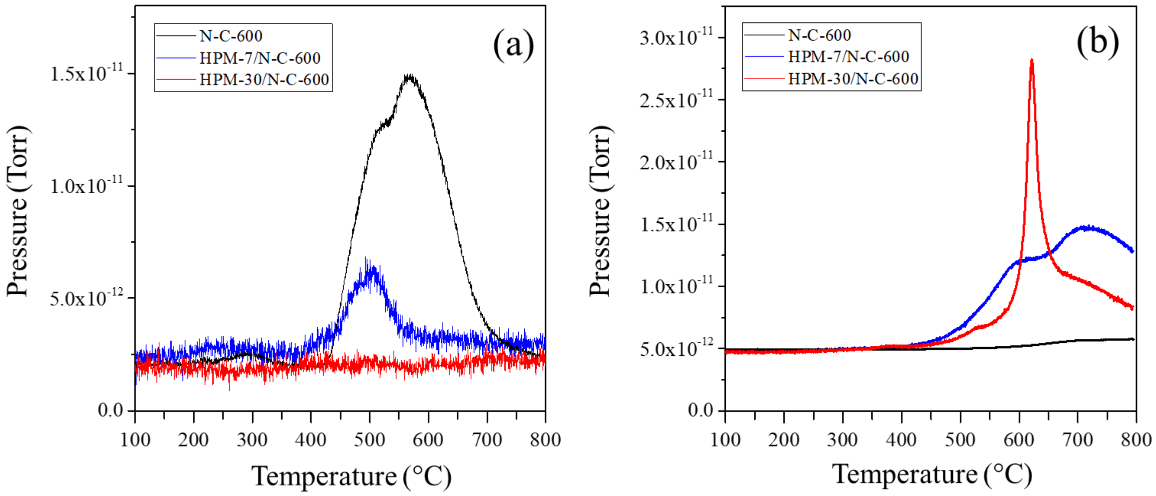

Figure 2-15. (a) NH_3 and (b) N_2 desorption signal without NH_3 adsorption step for N-C-600, HPM-7/N-C-600 and HPM-30/N-C-600 (all NH_3 and N_2 came from N-C-600). NH_3 and N_2

Signals are based on mass 17 and mass 14 respectively, and are normalized by the amount of N-C-600 used in the experiments.

Figure 2-16 showed the NH_3 evolution for HPM-7/N-C-600 and HPM-15/N-C-600 after the NH_3 adsorption step was added before the temperature ramp. No new N_2 peak appeared and the N_2 peak area remained the same. The new NH_3 peak, coming from the HPMs, appeared in the temperature range of 150-350 °C, which is similar temperature compared to that observed for the low loading HPM/C catalysts. H^+/POM ratios are calculated to be 0.58 and 0.53 for HPM-7/N-C-600 and HPM-15/N-C-600 respectively.

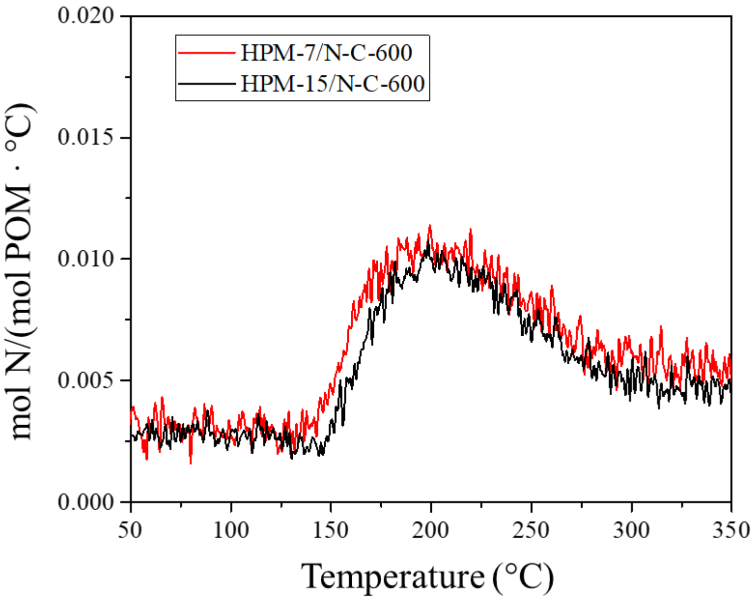

Figure 2-16. NH_3 desorption signal (mol N/(mol POM · °C)) based on mass 17 for HPM-7/N-C-600 and HPM-15/N-C-600.

NH_3-TPD for mpgC_3N_4 supported catalysts was also carried out. However, the N species desorbed from the support itself were complicated and hard to analyze, so the results are not shown here. NH_3-TPD for N-C-1000 supported catalysts were not performed due to the limited amount of N-C-1000 materials.

2.3.7 Butene Chemisorption

Butene chemisorption was also used to measure acid site population[59, 75]. Results are shown in Table 2-5. To address the large variation in surface area among the supports, catalysts with different supports were grouped based on the POM coverage level (0.04, 0.06 and 0.09 POM/nm^2). Take 0.06POM/nm^2 for example. As shown in Table 2-5, both HPM-15/C and HPM-20/N-C-1000 gave similar acid site population results (1.3 vs. 1.2 H^+/POM), which is about half of the stoichiometric value (3 H^+/POM). This is consistent with literature results showing that activated carbon supported POMs are less acidic than bulk POMs[76]. It also implies that the low nitrogen content (2%) of the N-C-1000 sample did not make a significant contribution to removing acid sites. However, for the supports with higher nitrogen concentrations, the H^+/ POM ratio was dramatically lower. For HPM-10/N-C-600, the H^+/ POM ratio decreased to 0.55. For HPM-3/mpgC_3N_4, which contains 53% nitrogen in the support, the H^+/ POM ratio dropped to an almost undetectable level, suggesting a very strong interaction between the HPM and mpgC_3N_4 which consumes almost all the available HPM protons at this loading. Note that the low H^+/POM ratio for HPM-3/mpgC_3N_4 was not due to the low loading, as the acid site population for HPM-30/mpgC_3N_4 was also measured to be about 0.03 H^+/POM. Thus, the same strong interaction between HPM and mpgC_3N_4 was observed even at 30wt% HPM loading. Experiments in which the catalysts were exposed to ammonia prior to butene uptake demonstrated complete suppression of butene adsorption. Thus, any NH_4^+ species that may have been present on the catalyst are insufficiently acidic to bind butene and are not counted as acid sites by this method.

Overall butene chemisorption gave similar results compared to NH_3-TPD. However, butene chemisorption failed to portray the increasing H^+/POM trend with HPM loading for the carbon-based catalysts. This is possibly because butene chemisorption cannot access protons in small POM clusters (2 or 3 POM molecules), and such clusters might exist for higher-loading HPM/C catalysts. However, since we are focusing on the H^+/POM trend at the same POM surface coverage level (0.04, 0.06 and 0.09 POM/nm^2), butene chemisorption still gives valid results when making comparisons within the same surface coverage group.

Supported HPM catalysts		**H^+/ POM**
0.04 POM/nm^2	HPM-10/C	1.33
	HPM-15/N-C-1000	1.14
	HPM-7/N-C-600	0.58
	HPM-2/mpgC_3N_4	less than 0.03
0.06 POM/nm^2	HPM-15/C	1.30
	HPM-20/N-C-1000	1.20
	HPM-10/N-C-600	0.55
	HPM-3/mpgC_3N_4	less than 0.03
0.09 POM/nm^2	HPM-20/C	1.35
	HPM-30/N-C-1000	1.10
	HPM-15/N-C-600	0.50
	HPM-4/mpgC_3N_4	less than 0.03

Table 2-5. N atom% on support surface (determined by XPS) and H^+/POM measured by butene adsorption for supported HPM. Catalysts are grouped by POM surface coverage.

2.4 Discussion

Three nitrogen-containing carbon materials (N-C-1000, N-C-600, mpgC_3N_4) with different nitrogen concentrations and nitrogen species distributions were examined in this study. XPS revealed that most of nitrogen in all three materials belonged to quaternary nitrogen, pyrrolic nitrogen and pyridinic nitrogen or their analogous species. However, in N-C-600 and mpgC_3N_4, for which the nitrogen contents were higher, some -NH_2 groups were also present on the surface. For N-C-600, the -NH_2 coverage on the surface was calculated to be about 2% based on the nitrogen content of the sample (19%) and the fraction of the XPS signal assigned to -NH_2 groups (10%). In the case of mpgC_3N_4, it is more complicated to determine the -NH_2 coverage because of the overlap with the N2 peak in XPS (see Figure 2-2(f)). However, an estimate can be made based on the N1 and N3 concentration obtained and the theoretical ratio of N1: N2: N3 in an ideal C_3N_4 structure (1: 1: 6, see Figure 2-2(g)). Since N1 and N3 account for 11% and 72% of the total nitrogen, the N2 concentration can be estimated at about 12%. Subtracting this value from the total assigned to N2 and -NH_2 yields an -NH_2 percentage of about 5% of the total N. This corresponds to a -NH_2 surface coverage of about 2.7%, given the overall nitrogen content of 53%.

It should be noted that the NH_2 surface coverages estimated above for both N-C-600 and mpgC_3N_4 are similar to the surface oxygen atom contents of these materials determined by XPS (Table 2). Thus, one cannot exclude the possibility that the -NH_2 groups present are amides (i.e., bound to a carbonyl carbon), rather than amines. If this is the case, their removal by hydrolysis with acidic POM solutions would be expected to be facile and may explain the observed formation of ammonium salts of the POMs.

HPMs can be supported on C, N-C-1000, N-C-600, mpgC_3N_4 and remain well dispersed at low coverages (less than 0.06 POM/nm^2). Individual HPM molecules can be seen on all four supports in the STEM-HAADF images (Figure 2-11). FTIR spectra showed that the HPMs were stable on all four supports (Figure 2-3) and that POMs remain its structure after methanol oxidation reactions (Figure 2-5). IR taken after the water-washing experiments showed that POMs are strongly adsorbed on N-C-600 and mpgC_3N_4 even at very high loadings. XRD further showed that for C and N-C-1000, where there was no or little nitrogen and no -NH_2 groups, some HPM crystallites were formed as the HPM loading was increased. For N-C-600 and mpgC_3N_4, where -NH_2 groups are present, NH_4PM crystallites were observed. This suggests that when there is NH_2 present on the support, the -NH_2 can be extracted by POMs, possibly by amide hydrolysis. This ammonium salt crystallite formation has not been previously recognized, although evidence for this phenomenon can be found in published data for POMs on nitrogen-containing carbons [12, 77, 78]. Regardless of the mechanism by which it occurs, it is important to recognize this phenomenon in catalyst preparation because it represents a change in the identity of surface species actually formed.

Another noteworthy point from the XRD results is the ability to disperse HPMs on the four materials tested. N-C-1000 showed a similar capability of dispersing HPMs compared to C, both can disperse about 0.20 POM/nm^2. However, the presence of abundant -NH_2 groups on the support does not improve the dispersion of POMs because of the tendency to form ammonium salt crystallites, in contrast to the earlier suggestions that -NH_2 will help disperse POMs[39]. This was demonstrated very clearly in the case of N-C-600, which can disperse less than 0.06 POM/nm^2 of HPMs before ammonium salt crystallite formation is detected. Surprisingly, mpgC_3N_4, which is nitrogen-rich and has amine groups present on the surface, can achieve full monolayer dispersion. Even at 2.06 POM/nm^2, the amount of NH_4PM crystallites formed remained very small.

The estimate of NH_4PM crystallite content for HPM-30/N-C-600 from XRD is consistent with our determination of the population of $-NH_2$ groups on this support from XPS. The 30wt% HPM loading on this 600 m^2/g support corresponds to a nominal coverage of $2.4 \cdot 10^{13}/cm^2$; conversion of this entire amount to $(NH_4)_3PMo_{12}O_{40}$ would require $7.2 \cdot 10^{13}$ $-NH_2/cm^2$. From the surface atom density of graphite ($3.8 \cdot 10^{15}/cm^2$) the nitrogen content of the N-C-600 material (19 at%), and the fraction of the nitrogen present as $-NH_2$ from XPS (10%), one can estimate the coverage of available $-NH_2$ groups to be $7.2 \cdot 10^{13}$ $-NH_2/cm^2$. Thus, there are sufficient amino groups on N-C-600 to convert 30% of the HPM loaded to ammonium salts as estimated from XRD.

The combined results of XRD and the nitrogen species distribution information obtained from XPS suggest an HPM-support interaction that mainly involves the $N_{Pyridinic}$ and amino groups on the support. It is possible that HPMs interact with both $N_{Pyridinic}$ and amino groups ($-NH_2$), where the $N_{Pyridinic}$ lead to dispersed HPMs and the amino groups to NH_4PM crystallites. Based on the XPS spectra of N-C-600, the ratio of $(-NH_2)/(-NH_2 + N_{Pyridinic})$ is calculated to be 17%, which is roughly comparable to the NH_4PM crystallite percentage in HPM-30/N-C-600 estimated from XRD. Thus, in the sample HPM-30/N-C-600, it is possible that around 20-30% of HPMs interacted with amino groups and formed ammonium salts, whereas the other 70-80% of HPMs interacted with pyridinic N and were dispersed on the support. This proposed mechanism can also offer an explanation to the superior HPM dispersion ability of $mpgC_3N_4$ compared to N-C-600, despite having similar $-NH_2$ surface concentration, since $mpgC_3N_4$ has far more pyridinic nitrogen in its structure. Therefore, in HPM-50/mpgC_3N_4, nearly all of HPMs loaded are potentially interacting with the $N_{Pyridinic}$ (N3 in Figure 2-2(g)) with very few interacting with amino groups and forming NH_4PM. Moreover, at HPM loadings less than 50wt% on mpgC_3N_4, the HPMs are likely to interact with pyridinic N only. Another possible explanation for this excellent ability of mpgC_3N_4 to disperse POMs is its ordered structure. The characteristic rhombic unit cell dimension of mpgC_3N_4 is 1.43 nm if planar, 1.37 nm if corrugated[79]. This is slightly larger than the POM anion (1nm). Thus, it is geometrically feasible for HPMs to form a 2 × 2 array in the voids of mpgC_3N_4 structure, see Figure 2-17. Such packing could achieve coverages of 70 to 78% of a theoretical close-packed POM monolayer. Both factors, the abundance of pyridinic N and its ordered structure, suggest that mpgC_3N_4 may be a promising candidate to support POMs at high surface coverages. Strong binding of the POMs in this fashion may also explain the absence of ammonium salt formation at monolayer coverage and below, even when surface NH_2 groups are available for salt formation as on N-C-600.

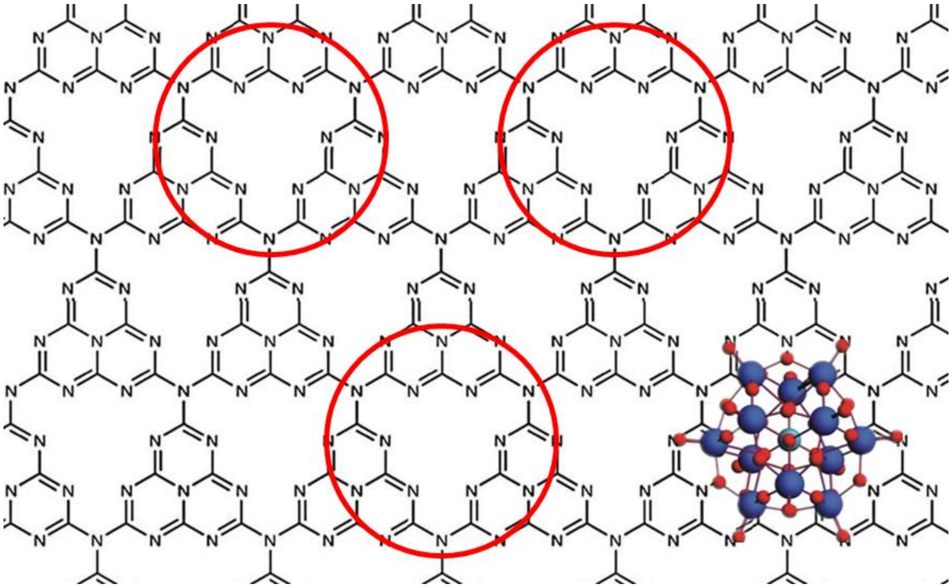

Figure 2-17. Proposed surface structure for HPM/mpgC_3N_4. HPMs form a 2 × 2 array in the voids of mpgC_3N_4 structure. Bottom right: top view of C_3 Symmetry HPM.

NH_3-TPD and butene adsorption was carried out in order to measure differences in acid site population and acid strength. NH_3-TPD showed that the H^+/POM ratio for HPM/C catalysts increased with HPM loading, and that the acid sites get stronger with higher loading catalyst such as HPM-20/C and HPM-30/C. Butene chemisorption failed to portray the increasing H^+/POM ratio trend with loading possibly because it is sensitive to dispersion, so the results are only used for acid site population comparison at the same POM surface coverage level. Based on the butene chemisorption results, at the same surface coverage level, N-C-600 (19% nitrogen) and mpgC_3N_4 (53% nitrogen) can reduce acid site population quite effectively due to their strong interaction with POMs compared to C and N-C-1000. mpgC_3N_4 suppressed almost all acidity. The strong interaction observed in N-C-600 and mpgC_3N_4 supported catalysts with butene chemisorption is consistent with the preliminary water washing experiment. These results provide guidance for controlling the acid site population of supported POM systems by taking advantage of the interaction between POMs and nitrogen-containing carbon materials.

2.5 Conclusions

Three nitrogen-containing carbon materials with a wide nitrogen content range and different N species distribution (N-C-1000, N-C-600 and mpgC_3N_4) were synthesized and used to support POMs (HPM and HPW). By comparing C, N-C-1000, N-C-600 and mpgC_3N_4, the effects of nitrogen in the support (both concentration and species distribution) on POM dispersion and acid site population were examined. XRD and FTIR demonstrated that high levels of -NH_2 can lead to ammonium POM salt crystallite formation. The POM dispersion ability of these supports followed the trend: N-C-600 < N-C-1000 ≈ C < mpgC_3N_4. mpgC_3N_4, in particular, can produce monolayer POM dispersions, possibly because of its rich pyridinic nitrogen content and its ordered structure. At low POM coverage (0.04, 0.06 and 0.09 POM/nm^2), the acid site population followed the trend: C $\approx$ N-C-1000 > N-C-600 > mpgC_3N_4. Thus, by using nitrogen-containing carbon materials as supports, one can construct molecularly-dispersed POMs catalysts with controllable acid site populations.

Chapter 3 Nitrogen-containing Carbon Supported POMs as Catalysts for Methanol Oxidation

3.1 Introduction

3.1.1 Methanol Oxidation as a test reaction

Methanol oxidation is a commonly used catalytic surface probe because it satisfies the three general criteria considered for such reactions. First, the activity should be influenced by the properties of catalytic surface, such as the chemical composition and the arrangement of surface atoms. Second, the test reaction should present different selectivity patterns, where different reaction routes can lead to different final products. Third, the mechanism of the test reaction should be thoroughly understood to give a correct interpretation of catalytic behavior observed. The pathways of methanol oxidation have been proposed by Iglesia[24] and Tatibouet[30] (shown in Scheme 3-1), where on acid site dimethyl ether is formed through dehydration of methanol, whereas on oxidation site methanol is oxidized into formaldehyde (HCHO), which can further react to become dimethoxymethane (DMM) and methylformate (MF).

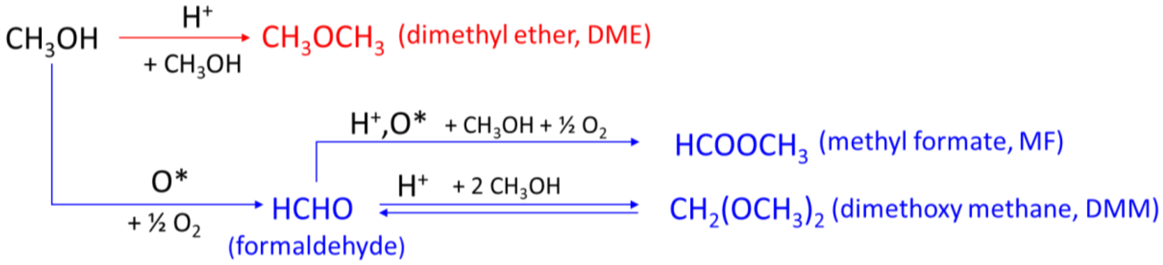

Scheme 3-1. Methanol oxidation and dehydration pathways as proposed by Iglesia.

Although it might seem that the dehydration and oxidation pathways are independent of one another, research from Iglesia and co-workers have proved that this is not the case. It is shown in their work using SiO_2-supported POM catalysts that when protons are titrated during reaction, both dehydration and oxidation rates dropped to very low level, which suggested that protons play a role in the methanol oxidation pathway too. The DFT study carried out by the same researchers suggested an oxidation pathway that involved proton sitting close to the oxidation site, which could possibly help stabilize the adsorbed methanol molecule.[24]

3.1.2 Nitrogen-containing carbon supported POMs as Oxidation catalysts in the literature

Amine-decorated carbon (N wt% = 1.7%[39], 1.1%[80]), and carbon embedded with other N-containing species (e.g., pyridinic, graphitic nitrogen) (N wt% = 2%[41, 81], 3.6%[82], 10.6% [42]) and nitrogen-containing polymers such as polyaniline (N wt% = 15%)[32] have been used as supports for POMs. They have proven useful in isopropanol oxidation[39, 42, 80, 82], methacrolein oxidation[81], methanol oxidation[41] and isopropanol decomposition[32], displaying in all cases a decrease in acid catalytic activity and enhanced oxidation activity compared to unsupported POMs. While nitrogen appears to play an important role by neutralization of some acidity, thus promoting selective oxidation pathways, the nature of the POM-support interaction is unclear. Moreover, previous studies have tended to examine a fairly narrow range of nitrogen concentrations (N wt% < 15%, N atom% < 10%) that may not fully reflect the potential for utilizing basic supports. In this section, catalysts supported on C, N-C-1000, N-C-600 and $mpgC_3N_4$, with a wide span of nitrogen content range (0-53atom%) are tested, to study how the support effect can change the result of methanol oxidation and dehydration.

3.2 Experimental

Methanol oxidation was carried out in a ¼” quartz tube in a resistively heated furnace (Mellen Microtherm) with a thermocouple placed at the top of the catalyst bed. Catalysts were pretreated in 20 kPa O_2 and 80 kPa He by ramping up temperature at 10 ˚C/min to 220˚C and holding for 0.5 hours before exposing catalysts to reactants. Reaction mixtures contained 5 kPa methanol (99.99%, Fisher), 2.5 kPa water (distilled and deionized), 20 kPa O_2 (99.99%, Purity Plus) and balance He (99.99%, Purity Plus). Methanol and water were delivered using syringe pumps (New Era Pump Systems NE-300). He and O_2 were delivered via flow controllers (GF80/GF40, Brooks). Catalyst loading (10-150 mg) and flow rate (10-100 sccm) were adjusted to maintain methanol conversions below 5%. Products were analyzed using an online gas chromatograph equipped with a DB-1 capillary column connected to FID and packed Hayesep Q and ShinCarbon ST columns connected to a TCD. All rates reported in this paper were measured after the catalyst reached steady state. For the higher surface area supports, up to 13 hr was required for DME formation to reach steady state. For the low surface area carbon nitride support, steady state was achieved more rapidly. This suggests that some slow rearrangement of the high surface area catalysts may occur under reaction conditions, as the activity decrease prior to reaching steady state was less than 50% in all cases. An example of the variation of DME production, measured by GC, is shown in Figure 3-1. Data points in the red box were used to calculate the average steady-state partial pressure of DME ($P_{DME)}$ and standard deviation. In this case the P_{DME} was calculated to be 0.0486 ± 0.00386 kPa, representing about ±7.9% error.

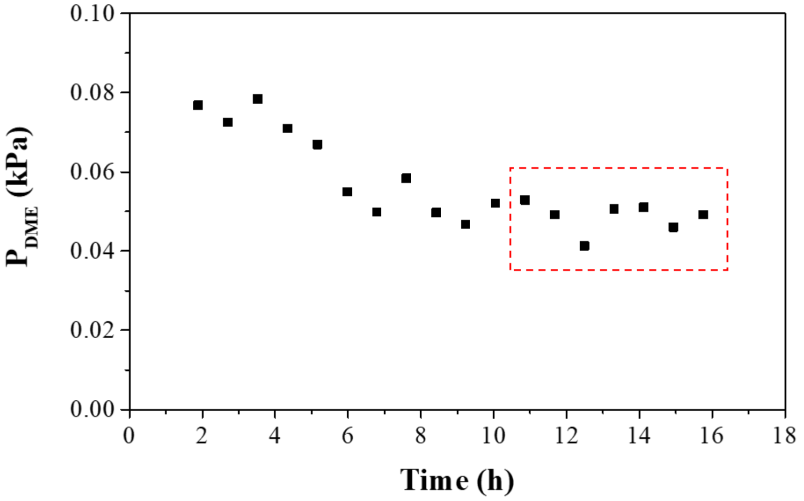

Figure 3-1. P_{DME} (partial pressure of DME measured by GC) vs. time for HPM-10/C (170mg) reaction at 220°C, with 30sccm total flow rate, 101kPa total pressure, 5 kPa CH_3OH, 18 kPa O_2, 2.5 kPa H_2O and balance He. Data points in the red box were used to calculate the steady-state P_{DME} average and standard deviation.

DME, HCHO, MF, DMM and H_2O were the main products for most of catalysts. CO and CO_2 were also detected, but the amount was small compared to the main products. Selective oxidation turnover frequency (TOF) was defined as the molar sum of HCHO, MF and DMM per POM, as the formation of DMM and MF each requires the formation of one molecule of HCHO, the primary product. Dehydration TOFs are presented in two ways, both as the molar production rate of DME normalized per POM and molar production rate of DME per Brønsted acid site (H^+), based on the acid site populations measured from butene adsorption experiments. Amounts of CO_X products ($CO+CO_2$) TOF per POM are also reported. All the analysis of TOF variations in this chapter is based on the assumption that the nature of the active sites is the same before and after reaction.

3.3 Results

3.3.1 Loading effects in C, N-C-1000, N-C-600 and mpgC_3N_4 supported HPM catalysts

Methanol oxidation was used to probe both acid and oxidation activity of the supported POM catalysts. Shown in Figure 3-1 are selective oxidation products (HCHO+MF+DMM), DME and CO_x turnover frequency (TOF) normalized per POM plotted vs. POM loading (wt%). As can be seen in the figure, for HPM/C and HPM/N-C-1000 catalysts, both selective oxidation and DME TOF increased as HPM loading increased. The DME TOF trend observed here is consistent with the NH_3-TPD results for HPM/C shown in Chapter 2 (Table 2-4), where for catalysts with higher HPM loading, both acid site population and acid site strength increased. To account for the change in acid site population, DME TOF data normalized per H^+ (acid site population measured by NH_3-TPD) are calculated for HPM/C and plotted in Figure 3-1(a). As shown in the figure, DME TOF per H^+ still showed a similar increasing trend with HPM loading compared to DME TOF normalized by POM, which suggested that only a portion of the increasing trend can be explained by the increase in total acid site population, because otherwise a flat line should be observed when TOF is normalized per H^+. A similar trend was observed in another research conducted in Barteau Group that involved using cation exchange to control the acid site of supported POMs, in which the non-ideal increasing trend is explained by a difference in thermodynamic activity of protons between catalysts with different H^+/POM ratio. A similar discussion applied to HPM/C catalysts with different loadings can be found in Section 3.4.1. For both HPM/C and HPM/N-C-1000, oxidation TOF per POM also followed a similar trend with DME TOF, which is consistent with studies from Iglesia group, indicating that protons are needed in methanol oxidation with supported POM catalysts[24]. CO_x TOF was low for all HPM/C and HPM/N-C-1000 catalysts.

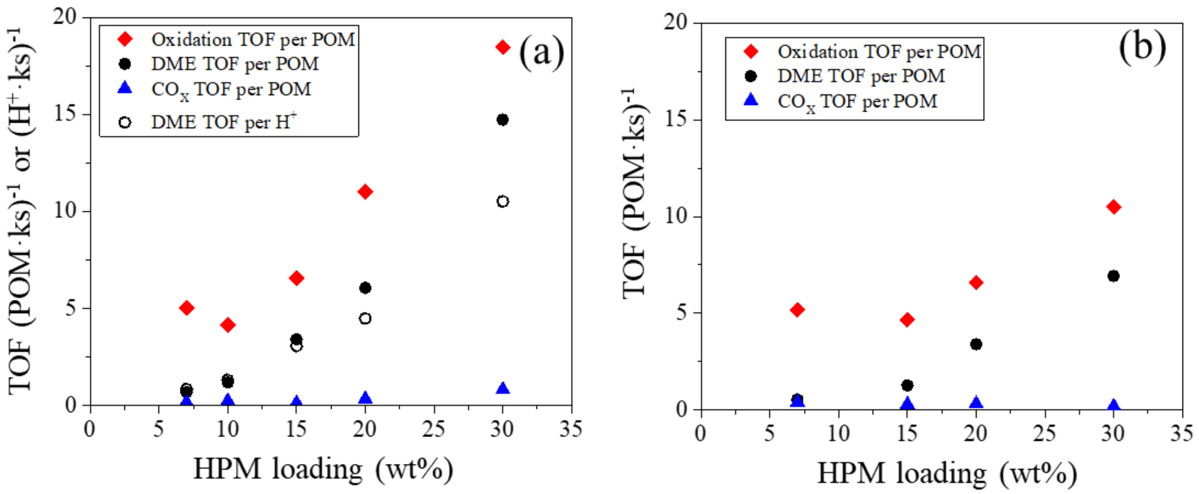

Figure 3-2. Oxidation (HCHO + MF + DMM) TOF per POM, DME TOF per POM, CO_x TOF per POM and DME TOF per H^+ at various HPM loading (wt%). (a) HPM/C, (b) HPM/N-C-1000

The TOF trend for DME, Selective Oxidation and CO_x products for HPM on N-C-600 and mpgC_3N_4 is quite different from that on C and N-C-1000. For both HPM/N-C-600 and HPM/mpgC_3N_4, a decreasing trend for both DME and Oxidation TOF with loading is observed, as demonstrated by Figure 3-2. One possible reason for the different trend observed in Figure 3-1 and Figure 3-2 is that unlike HPM/C and HPM/N-C-1000, the H^+/POM ratio for HPM/N-C-600 and HPM/mpgC_3N_4 did not change much when HPM loading changed (H^+/POM ratio measured by NH_3-TPD for HPM-7/N-C-600 and HPM-15/N-C-600 is 0.58 and 0.53 respectively. Acid site population for HPM/mpgC_3N_4 remains very close to zero within the loading range of 2-30wt%.). Thus, it is possible that with H^+/POM ratio remaining constant, other factors come into play, e.g., POM dispersion effects. For HPM/N-C-600, NH_4PM crystallites were identified in XRD for HPM loadings higher than 15wt% (shown in Chapter 2, Figure 2-7), which could lead to a loss in the number of active oxidation sites. For HPM/mpgC_3N_4, although no crystallites was observed up to 30wt%, clusters of 2-3nm did appear in HAADF-STEM for HPM-7/mpgC_3N_4, meaning that small clusters of 2-3 POM molecules can form at relatively low loading. Therefore, it is possible that such cluster formation in HPM/mpgC_3N_4 can lead to blockage of active sites and thus low oxidation TOF.

For DME and CO_x TOF, HPM/N-C-600 and HPM/mpgC_3N_4 also exhibited very different behavior compared to HPM/C and HPM/N-C-1000. DME TOF are much lower compared to catalysts with C or N-C-1000 as supports, which is consistent with the lower H^+/POM ratio from butene chemisorption. CO_x TOF, however, is higher than that from HPM/C and HPM/N-C-1000, which agrees with literature results that suggest CO_2 is mainly formed on basic sites[30].

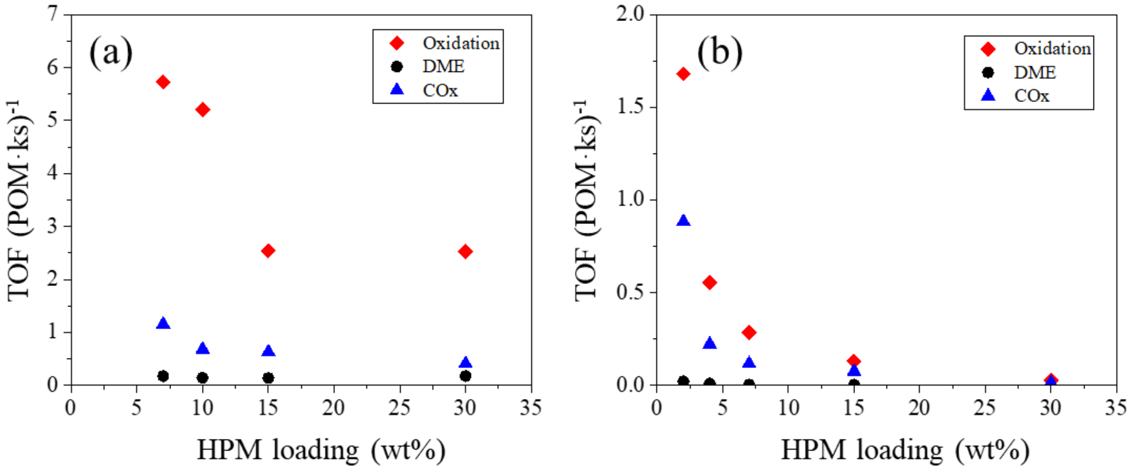

Figure 3-3. TOF for Oxidation (HCHO + MF + DMM), DME and CO_x at various HPM loading (wt%). (a) HPM/N-C-600, (b) HPM/mpgC_3N_4

3.3.2 HPM/C, HPM/N-C-1000, HPM/N-C-600 and HPM/mpgC_3N_4 at comparable surface coverages

In this section methanol oxidation and dehydration results are compared across four different supports on the same coverage levels (0.04, 0.06, 0.09 POM/nm^2). DME TOF (POM·ks)$^{-1}$ is shown in Figure 3-3 (a). As demonstrated, HPM on C and N-C-1000 showed almost the same acid activity at every coverage level respectively. However, the acid activity decreased dramatically for supports with higher nitrogen content (N-C-600 and mpgC_3N_4). It dropped two to three orders of magnitude from C to mpgC_3N_4 for comparable POM coverages.

Much of the dramatic drop in acid activity in Figure 3-3(a) can be explained by the decrease in acid site population, since the TOFs in Figure 3-3(a) were normalized per POM. In Figure 3-3(b) DME TOF $(H^+ \cdot ks)^{-1}$ were plotted, where the acid site population is based on the butene chemisorption results. Because of the difficulty of measuring acid site populations on the mpgC_3N_4 catalysts, dehydration TOFs per acid site are less reliable for these catalysts. Even so, comparing the N-C-600 supported catalysts to the carbon-supported catalysts, it is apparent that the decrease in rate is larger than can be explained by the decrease in acid site population measured by butene chemisorption shown in Chapter 2, Table 2-5. This suggests that supports with higher nitrogen content not only reduce the acid site population, but also decrease the reactivity of the remaining acid sites.

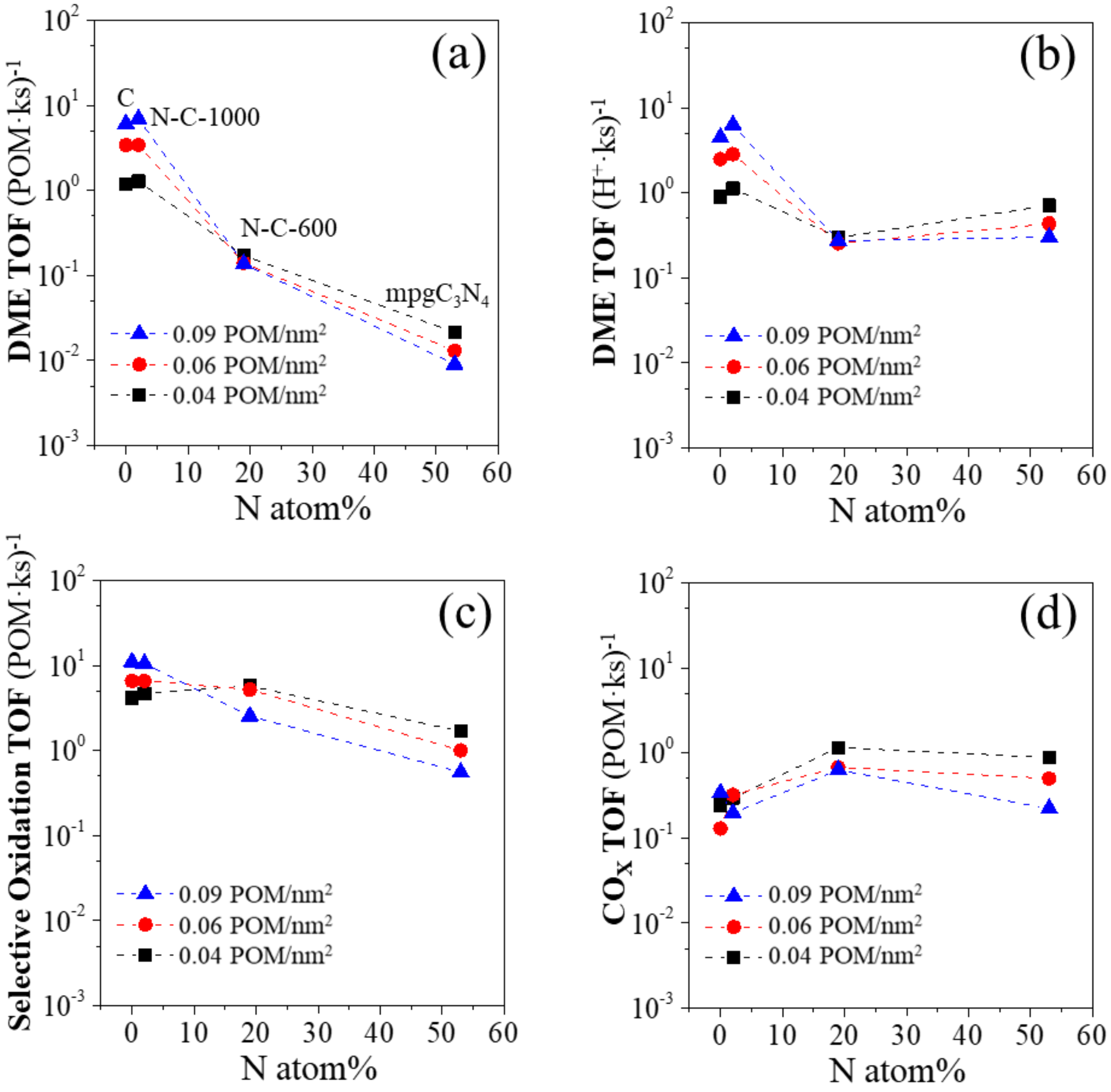

Figure 3-4. (a) DME TOF (POM·ks)$^{-1}$, (b) DME TOF (H$^+$·ks)$^{-1}$, (c) Selective Oxidation TOF (POM·ks)$^{-1}$, (d) CO_X TOF (POM·ks)$^{-1}$as a function of nitrogen content of the supports, at 0.04, 0.06, 0.09 POM/nm^2 coverage levels. (493 K, 5 kPa CH_3OH, 20 kPa O_2, 2.5 kPa H_2O, less than 5% conversion)

Oxidation TOF is again reported in two parts, selective oxidation TOF (HCHO, MF, DMM) and CO_X TOF (CO, CO_2). Selective oxidation TOF (POM·ks)$^{-1}$ is presented in Figure 3-3(c). As demonstrated, aside from HPM/N-C-1000, which exhibited similar activity as HPM/C, selective oxidation TOF also decreased as the nitrogen content increased to 19atom% and 53atom%. However, CO_X TOF presented a different trend. As shown in Figure 3-3(d), N-C-600 and mpgC_3N_4 produced more CO_X than C and N-C-1000, which is consistent with what is observed in Section 3.3.1 and could be attributed to the basic nature of the supports with more nitrogen.

It is interesting that DME TOF and Selective Oxidation TOF follow the same decreasing trend if comparing Figure 3-3 (a) and (c). This relationship is clearer in Figure 3-4, where Selective Oxidation TOFs $(POM \cdot ks)^{-1}$ are plotted vs. DME TOFs $(POM \cdot ks)^{-1}$ and DME TOFs $(H^{+} \cdot ks)^{-1}$ respectively. MpgC_3N_4-based catalyst data were not included in figure 3-4(b), because DME TOFs per acid site are less reliable for these catalysts due to the difficulty in measuring acid sites. Nevertheless, we can see in both figures that catalysts with higher DME TOFs, normalized per POM or per acid sites, also exhibited higher oxidation TOFs. This is in agreement with previous work by Iglesia[24]. They have shown that when titrating the SiO_2-supported HPM catalyst with 2, 6-di-*tert*-butylpyridine during methanol oxidation reaction, dehydration and oxidation rate decreased together, which suggested that acid sites are involved in formaldehyde production. Their DFT calculations indicated that the lowest energy pathway for methanol oxidation involved interactions between molecular methanol and protons from the catalyst, explaining the association between dehydration and oxidation rates.

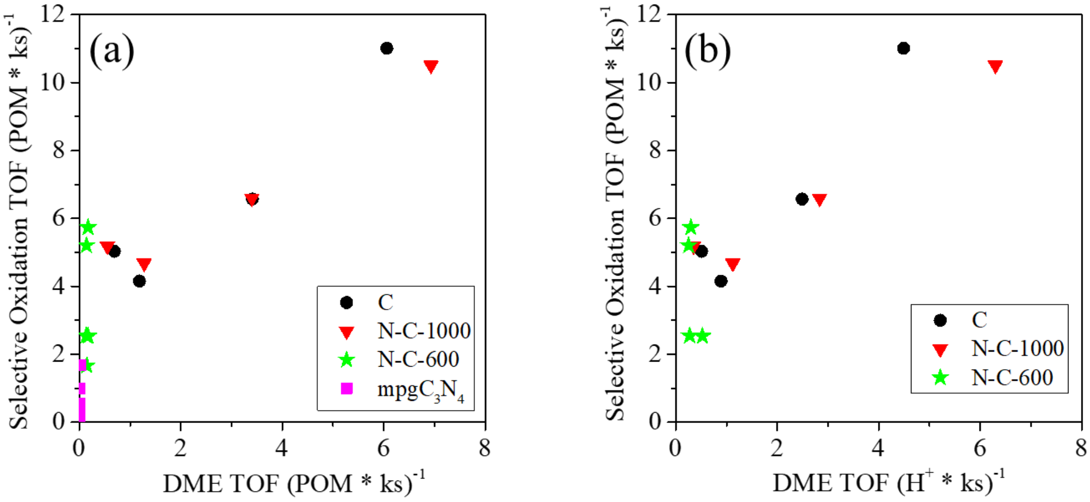

Figure 3-5. (a) Selective Oxidation TOF (POM·ks)$^{-1}$ as a function of DME TOF (POM·ks)$^{-1}$ for HPM/C (7-20wt%), HPM/N-C-1000 (7-30wt%), HPM/N-C-600 (7-30wt%) and HPM/mpgC$_3$N$_4$ (2-30wt%); (b) Selective Oxidation TOF (POM·ks)$^{-1}$ as a function of DME TOF (H$^+$·ks)$^{-1}$ for HPM/C (7-30wt%), HPM/N-C-1000 (7-30wt%), HPM/N-C-600 (7-30wt%). (493 K, 5 kPa CH_3OH, 20 kPa O_2, 2.5 kPa H_2O, less than 5% conversion)

3.4 Discussion

3.4.1 Loading effects

The ability of using support-POM interaction to control acid activity was tested using methanol oxidation and dehydration as a test reaction. When comparing oxidation and dehydration activity with various loading within each support group, we found different TOF trend for C/ N-C-1000 supported catalysts and N-C-600/mpgC$_3$N$_4$ supported catalysts. Both DME and Oxidation TOF for C/N-C-1000 supported POM catalysts increased with HPM loading, whereas Oxidation TOF for N-C-600/mpgC$_3$N$_4$ supported POM catalysts decreased with HPM loading (DME TOFs are very low for those catalysts so the DME TOF trend is not discussed here).

To understand why the DME TOF changed so much with HPM loading for HPM/C and HPM/N-C-1000 catalysts, DME TOF per H^+ is plotted for various H^+/POM ratios (only HPM/C data is discussed here because we have shown in Section 3.3.2 that HPM/C and HPM/N-C-1000 exhibited identical reaction rates at the same POM surface coverages). In Figure 3-5 (a), an increasing trend of DME TOF per H^+ vs. H^+/POM ratio is observed. This trend is similar to the results of another POM project from Barteau Group, which focused on the effect of cation exchange in supported POM catalysts. The finding from the cation exchange study showed that when H^+/POM ratio decreased due to different extent of cation exchange, the DME TOF in methanol oxidation decreased exponentially. A novel theory is proposed to explain this TOF behavior based on a framework developed to apply activity coefficients to describe supported POM catalysts. Since a similar trend is seen here, the same method is applied to see if it can be used to explain the 'non-ideal' behavior observed for HPM/C when HPM loading changes.

The main idea of the framework is to treat supported POM catalysts as a concentrated acid solution that follows the theory of Debye and Hückel[83] and Harned's rule[84, 85], which is reasonable because similar to concentrated acid solutions, anions, cations as well as water (from either water of hydration, or the water fed during reaction) exist in supported POM catalysts under reaction conditions. Following this assumption, a modified Harned's rule equation (Equation 3-1) can be used to calculate the activity coefficient (γ_H) that describes proton activity, using variable χ defined as the fractional extent of proton removal (Equation 3-2).

Equation 3-1: Harned's rule defined using the extent of proton removal, χ.

$$\log_{10}(\gamma_H)=\log_{10}\left(\gamma_{\mathrm{H}}^{\mathrm{pure}}\right)-\alpha\chi$$

Where γ_H is activity coefficient for proton, γ_H^{pure} is set equal to 1, χ is the fractional extent of proton removal defined in equation 3-2, and α is the Harned coefficient defined for the extent of proton removal.

Equation 3-2: The fractional extent of proton removal, χ, as a function of the quantity of acid sites per POM, N_{H+}.

$$\chi = \frac{N_{H^+,30} - N_{H^+,x}}{N_{H^+,30}}$$

where χ is the extent of proton removal, $N_{H+,30}$ is the quantity of protons per POM measured by NH_3-TPD for HPM-30/C, and $N_{H+,x}$ is the quantity of protons per POM measured by NH_3-TPD for HPM-x/C.

γ_H calculated using equation x with $\alpha = 2.5$ is plotted in Figure 3-5 (a). As shown in the figure, the γ_H curve (open symbol) has a similar shape as DME TOF per H^+ (closed symbol), which indicates goodness of fit between the activity coefficients of H^+ and the non-ideal behavior observed for DME TOF per H^+. When the difference in γ_H is taken into consideration in the calculation of TOF (TOF_γ described in Equation 3-3), the result appears invariant (with the exception of HPM-20/C) with H^+/POM ratio and HPM loading, as shown in Figure 3-5(b). Therefore, by calculating TOF using proton thermodynamic activity instead of proton concentration, we are able to normalize dehydration rates to get invariant TOFs with different H^+/POM ratios.

Equation 3-3: DME TOF defined using the proton activity coefficient and proton concentration.

$$\text{DME TOF}_\gamma\ (\text{ks}^{-1}) = \frac{\text{mol DME}}{\text{mol H}^+ \cdot \gamma_\text{H} \cdot \text{ks}}$$

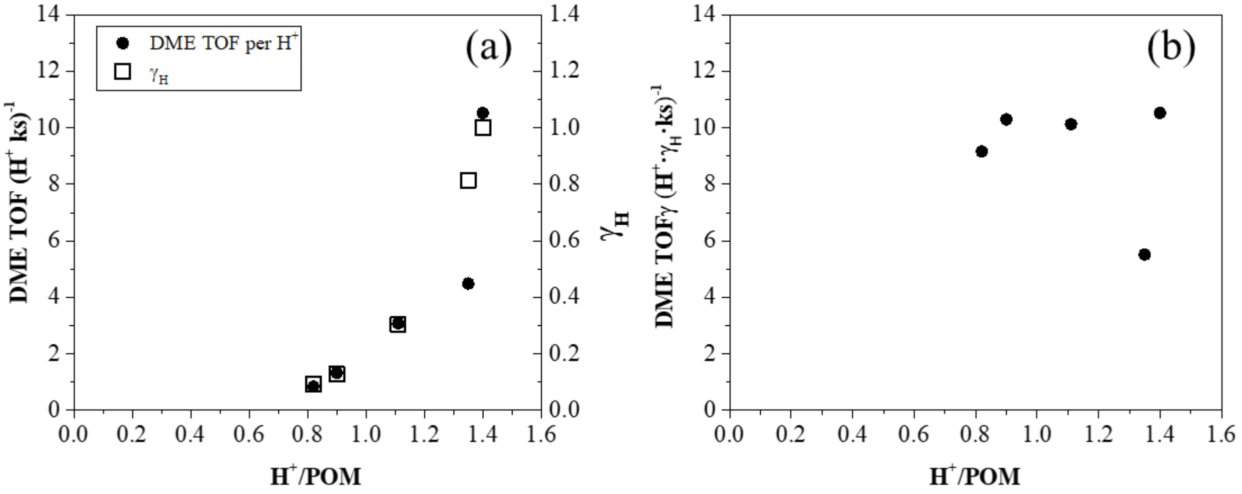

Figure 3-6. (a) DME TOF per H$^+$ and γ_H at various H$^+$/POM ratio; (b) DME TOF$_\gamma$ (H$^+ \cdot \gamma_H \cdot$ks)$^{-1}$ at various H$^+$/POM ratio for HPM/C

For HPM/N-C-600 and HPM/mpgC_3N_4, the H$^+$/POM ratio did not change much with loading within each support group, so a similar analysis could not be carried out. However, an attempt was made to incorporate HPM-7/N-C-600 and HPM-15/N-C-600 data into Figure 3-5. As shown in Figure 3-6, the addition of HPM/N-C-600 data did not disrupt the trend followed by HPM/C. For both HPM/C and HPM/N-C-600 catalysts, DME TOF normalized by thermodynamic activity DME TOF$_\gamma$ (calculated using the same α value, 2.5) is relatively constant at various H$^+$/POM ratio and various HPM loading, suggesting that H$^+$/POM ratio may be the one determining factor for DME TOF when either cation exchange or support effects is used to control the acid sites in supported POM catalysts.

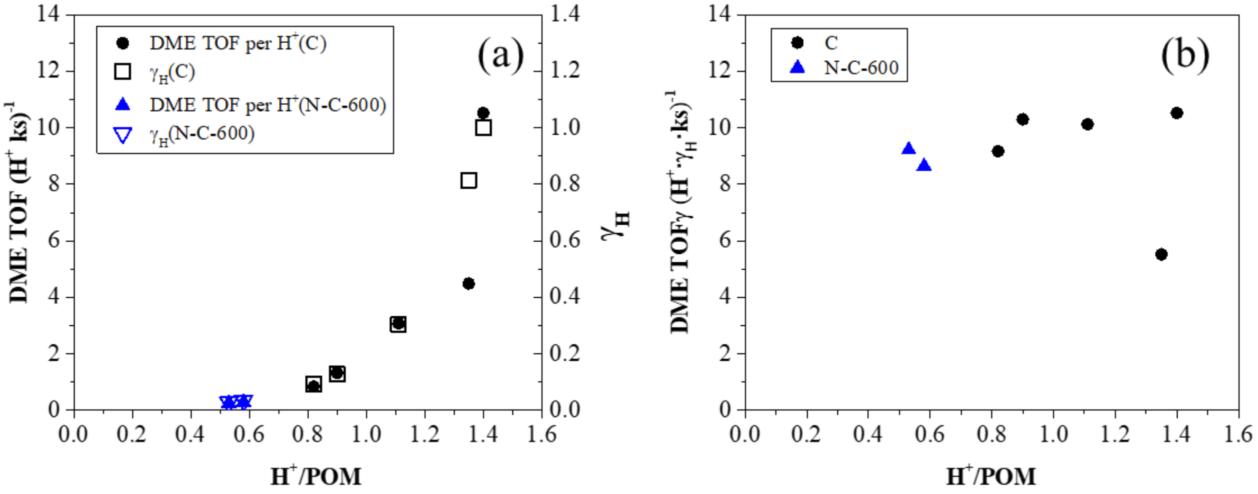

Figure 3-7. (a) DME TOF per H^+ and γ_H at various H^+/POM ratio; (b) DME TOF_γ $(H^+ \cdot \gamma_H \cdot ks)^{-1}$ at various H^+/POM ratio for HPM/C and HPM/N-C-600

In the cation exchange project for supported POM catalysts, the same trend of DME TOF was found for oxidation TOF. And it is shown that when adding the thermodynamic activity coefficient to normalize the oxidation TOF, i.e., using Equation 3-4 to calculate Oxidation TOF_γ, the Oxidation TOF_γ would also be invariant at various H^+/POM ratio when the extent of cation exchange varied. However, this is not true in the case of support effect, when H^+/POM changed with HPM loading as well as with different supports. As shown in Figure 3-7, the shape of γ_H did not agree with the shape of Oxidation TOF per POM, especially at low loading HPM/C and HPM/N-C-600 catalysts. Therefore, Oxidation TOF_γ is not constant over various H^+/POM ratio here. This suggested that using cation exchange and support effect to control the oxidation activity of supported POM catalysts is different when in the low H^+/POM regime, possibly because in that region dispersion effects and interactions between POMs and supports come into play.

Equation 3-4: Oxidation TOF defined using the proton activity coefficient and POM concentration.

$$\text{Oxidation TOF}_{\gamma}\ (\text{ks}^{-1}) = \frac{\text{mol (HCHO + DMM + MF)}}{\text{mol POM} \cdot \gamma_H \cdot \text{ks}}$$

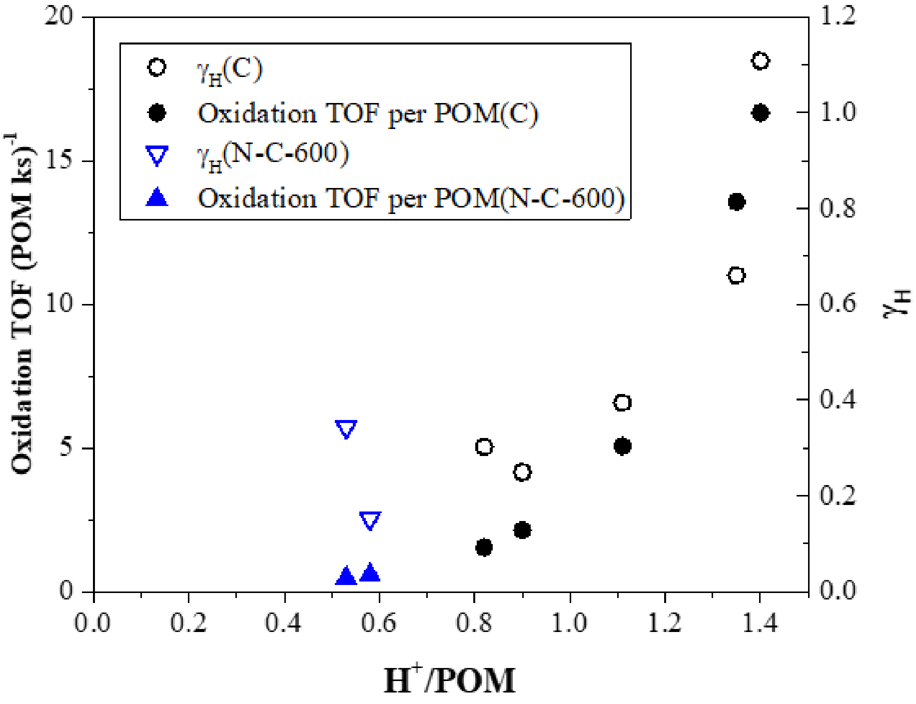

Figure 3-8. Oxidation TOF per POM and γ_H at various H$^+$/POM ratio for HPM/C and HPM/N-C-600

3.4.2 TOF trend at the same surface coverage level

When compared at the same surface coverage level (0.04, 0.06, 0.09 POM/nm^2), DME formation rates between N-C-1000 and C based catalysts showed that the 2 atom% nitrogen in N-C-1000 is not effective in reducing the acid activity, contrary to common belief that a little nitrogen doped in carbon would significantly affect the support-POM interaction. This has not been pointed out in previous literature because most researchers have used unsupported POMs as a benchmark to compare their catalysts[39, 41, 42, 81, 82]. Supports with higher nitrogen content (N-C-600 and mpgC_3N_4), which have not been studied as supports for POMs before, produced much lower DME formation rate regardless of coverage levels. mpgC_3N_4 suppressed almost all the acid activity to 2-3 orders of magnitude below that of C and N-C-1000.

The selectivity of Selective Oxidation products for all catalysts tested here fell in the range of 60-85% (molecule based), higher than the SiO_2-supported HPM catalysts which usually have less than 50% selectivity toward oxidation products under the same reaction condition. Among all the catalysts tested, the N-C-600 based catalysts gave the highest selective oxidation selectivity (80-85%), due to their significantly lowered DME selectivity (less than 5%) and moderate CO_x formation. N-C-600 catalysts also give the highest selectivity to HCHO (about 80%) among all the catalyst tested, since only a small portion of HCHO further reacted to become secondary products. For mpgC_3N_4 based catalysts, although with even lower DME selectivity (about 1%), the selectivity of selective oxidation products is about 70% because they produce more CO_x (up to about 30% selectivity.)

3.5 Conclusions

Within each support group, DME TOF and Oxidation TOF responded in different ways to loading changes for HPM supported on C/N-C-1000 and HPM supported on N-C-600/mpgC_3N_4. For HPM supported on C/N-C-1000, DME TOF and Oxidation TOF increased as HPM loading increased. The increasing trend of DME TOF per H^+ can be portrayed by the trend of thermodynamic activity coefficient γ vs. H^+/POM ratio, which is consistent with the DME TOF behavior when cation exchange is used to control acid sites. The DME TOF normalized per proton activity is constant over a H^+/POM ratio range of 0.5-1.4 when both HPM/C and HPM/N-

C-600 are plotted. Oxidation TOF (POM * γ_H) is not constant over the same range of H^+/POM ratio, possibly because of dispersion effects and the interactions between POMs and different supports at low H^+/POM ratio.

When compared at the same surface coverage level (0.04, 0.06, 0.09 POM/nm^2), both DME TOF $(\text{POM}\cdot\text{ks})^{-1}$ and Selective Oxidation TOF $(\text{POM}\cdot\text{ks})^{-1}$ followed the trend: C ≈ N-C-1000 > N-C-600 > mpgC_3N_4, with DME TOF $(\text{POM}\cdot\text{ks})^{-1}$ dropping more dramatically than Selective oxidation TOF. N-C-600 based catalyst presented the highest selectivity to selective oxidation products as well as to formaldehyde. This is the first systematic study of the modification of POM acidity by nitrogen-containing carbon support materials, which can provide guidance in using supports to tune the properties of supported POMs.

Chapter 4 Kinetics and mechanistic details for methanol oxidation and dehydration

4.1 Introduction

The known structure and bifunctional nature of POMs make them ideal to probe the mechanism for methanol oxidation and dehydration. Mechanistic interpretations of the formation of primary products, DME from CH_3OH dehydration and HCHO from oxidative dehydrogenation (ODH, calculated as the sum of HCHO, MF and DMM) has been studied in detail by Iglesia and co-workers using SiO_2-supported POM catalysts[24, 86].

For methanol dehydration, Iglesia and co-workers proposed that DME is formed by the concerted reactions between co-adsorbed CH_3OH molecules (protonated methanol dimer) and involved a late ion-pair transition state according to their DFT calculation. These researchers have also suggested that separate assessments of ionic and covalent deprotonation energy (DPE, the energy required to separate a proton from a conjugate base to non-interacting distance), can serve as a descriptor for DME reactivity[24].

For methanol oxidative dehydrogenation, existing literature has agreed that it involves Mars-van Krevelen ODH redox cycles, and the rate limiting step is the breaking of C-H bond in either adsorbed methoxy group or molecularly adsorbed methanol[24, 30]. The Iglesia group used DFT results to argue that the H-abstraction from the adsorbed methanol molecule, rather than dissociated methoxy group is more energetically favorable.[86] They also suggested that a late transition state was involved in this process, and that the energy of the transition state correlates with H-atom addition energy (HAE), which is the energy of adding an H-atom to an O-atom in POM molecule (the value is averaged over all the O atoms in POM structure). Thus, they proposed that the HAE can be used as a reactivity descriptor for oxidative dehydrogenation reaction of methanol.

There are fewer discussions about the kinetics of the secondary products in the literature. Researchers generally agree that the formation of both MF and DMM involve hemiacetal intermediates. Tatibouet has suggested that the selectivity of MF and DMM depends on the acid strength as well as the nucleophilic character of the catalyst surface[30]. Iglesia found that the reactions leading to DMM and MF are influenced by the properties of support surfaces[33, 87]. Acidic surfaces such as SiO_2 favored DMM formation, while amphoteric or dehydrogenating surfaces like ZrO_2 and TiO_2 led to MF formation. No specific rate equations or kinetic models have been proposed for MF and DMM.

4.2 Experimental

Kinetics experiments for methanol oxidation and dehydration were carried out in a ¼” quartz tube in a resistively heated furnace (Mellen Microtherm) with a thermocouple placed at the top of the catalyst bed. Catalysts were pretreated before the reactant mixture was flowed into the reactor as described in Section 3.2. Four catalysts, including both HPM/C and HPM/N-C-600 catalysts with two surface coverage levels for each group of catalysts (HPM-10/C (0.04 POM/nm^2), HPM-20/C (0.09 POM/nm^2), HPM-7/N-C-600 (0.04 POM/nm^2), HPM-15/ N-C-600 (0.09 POM/nm^2)), were chosen for the kinetics experiments, so that both loading effects and support effects on kinetics could be studied. Kinetic experiments for HPM/N-C-1000 were not performed because it has been shown in Chapter 3 that HPM/N-C-1000 catalysts behave very similar to HPM/C at the same POM surface coverage levels. HPM/mpgC_3N_4 catalysts were also not chosen for kinetic experiments because of their general inactivity toward methanol oxidation and dehydration as well as its high selectivity to CO_x products.

A series of experiments were carried out for each catalyst (HPM-10/C (0.04 POM/nm^2), HPM-20/C (0.09 POM/nm^2), HPM-7/N-C-600 (0.04 POM/nm^2), HPM-15/ N-C-600 (0.09 POM/nm^2)). The experiments performed using HPM-10/C are shown in Table 4-1. 170mg HPM-10/C catalyst was used in all seven experiments, and the reactions were run at 220℃ and 101kPa total pressure. For experiment 1, the total flow rate was varied with all other variables (partial pressure of CH_3OH, O_2 and H_2O in the feed) kept the same. Changing the total flow rate leads to a change in space time (or space velocity), thus a change to the conversion achieved at the end of catalyst bed. For 170 mg HPM-10/C at 220℃, a change in total flow rate of 5-120sccm would lead to 2.5-23% conversion. For experiment 2, O_2 partial pressure was changed to study the effect of O_2 on the reaction kinetics. Results of experiment 2 showed that changing O_2 partial pressure had no effect on the kinetics of both methanol oxidation and dehydration, thus O_2 is not included in any discussion or figures in this chapter. For experiments 3 and 4, methanol partial pressure was changed to see the role of methanol in the reaction kinetics. 0 kPa and 2.5 kPa water were co-fed into the system in experiments 3 and 4 respectively to understand the kinetics effect of water, because water accompanies the formation of every major product in methanol oxidation and dehydration and it can compete with methanol for catalytic sites in the reaction process. For experiments 5-7, various partial pressures of HCHO, MF or DMM were fed into the reactor along with CH_3OH, O_2 and H_2O, to check the kinetic effects of HCHO, MF or DMM respectively. Different partial pressures of HCHO, MF or DMM were achieved by injecting using a syringe pump (New Era Pump Systems NE-300) a mixture of certain concentration of HCHO/MF/DMM, CH_3OH and H_2O that was mixed prior to the injection. Experiments 2-7 were all run under 10% conversion. In all experiments the catalyst was allowed to go to steady state before any change in flow rate or partial pressure was made to the system. All reactions, except for $HCHO + 2CH_3OH \longleftrightarrow CH_3OCH_2OCH_3(\boldsymbol{DMM}) + H_2O$, are far from equilibrium under the reaction conditions listed in Table 4-1.

	flow rate (sccm)	O_2 (kPa)	CH_3OH (kPa)	H_2O (kPa)	HCHO (kPa)	$HCOOCH_3$ (kPa)	$CH_2(OCH_3)_2$ (kPa)
expr 1	**5-120**	20	5	2.5	0	0	0
expr 2	30	**5-30**	5	0	0	0	0
expr 3	30	20	**2-20**	**0**	0	0	0
expr 4	30	20	**2-20**	**2.5**	0	0	0
expr 5	25	20	15	2.5	**0, 0.6, 0.9**	0	0
expr 6	25	20	15	2.5	0	**0, 0.1, 0.2**	0
expr 7	25	20	15	2.5	0	0	**0, 0.5, 1**

Table 4-1. Kinetic experiments for 170mg HPM-10/C, 220℃, 101kPa. Balance He.

Data from all the kinetics experiments were used to construct the kinetics models. Ordinary differential equations (ODEs) based on mass balance in packed-bed reactor and proposed reaction mechanisms are solved numerically with Matlab. Kinetic parameters were adjusted individually to get the model that gives prediction results closest to experimental results.

4.3 Results

4.3.1 Reaction network

Information about the reaction network of methanol oxidation and dehydration are mainly given by experiments 5-7 and will be discussed in this section. The results of experiment 1 (vary total flow rate) and experiments 3&4 are shown in Figure 4-3 to Figure 4-10. These results will be discussed in detail later in section 4.3.3.

Results from experiment 5 (co-feeding HCHO) are shown in Figure 4-1. As shown in the figure, the formation rates of DMM, MF and CO are all first order in HCHO (Figure 4-1(a)), whereas DME (Figure 4-1(b)) and CO_2 (Figure 4-1(c)) are both 0th order in HCHO. The results for DME, DMM and MF is consistent with the reaction network proposed by both Iglesia[24] and Tatibouet[30].

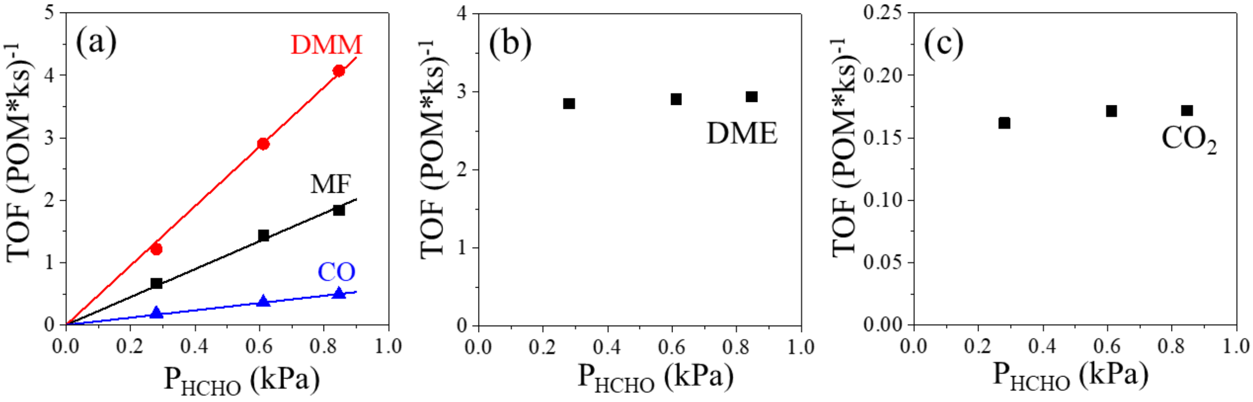

Figure 4-1. TOF of (a) DMM, MF and CO (b) DME (c) CO_2 at various HCHO partial pressure (P_{HCHO}, kPa). Reaction and catalyst information: 156mg HPM-10/C, 220°C, 101kPa total pressure, 25sccm total flow rate, 15kPa CH_3OH, 20kPa O_2, 2.5kPa H_2O, balance He.

Reaction pathways for CO and CO_2 have not been discussed in the literature before. It is interesting to see from our experiment that CO and CO_2 have different kinetic responses regarding HCHO. This result suggests that CO is a secondary product coming from HCHO, whereas CO_2 is not. This is backed by another evidence that comes from the CO_2 partial pressure vs. space time (τ, calculated using Equation 4-1) plot based on results from experiment 1 (Figure 4-2). As can be seen from this figure, for all the four catalysts tested, at $\tau = 0$, the slope of an imaginary curve for P_{CO2} has a non-zero value, meaning that at $\tau = 0$, CO_2 is being produced at a non-zero rate. Since at $\tau = 0$ only methanol, O_2 and H_2O exist, at least a portion of CO_2 has to come directly from methanol as primary product.

Equation 4-1: Calculation of space time (τ)

$$\tau = \frac{W}{F_{CH3OH,\,0}}$$

where W is HPM amount in μmol, $F_{CH3OH,\,0}$ is CH_3OH initial flow rate in μmol/ks.

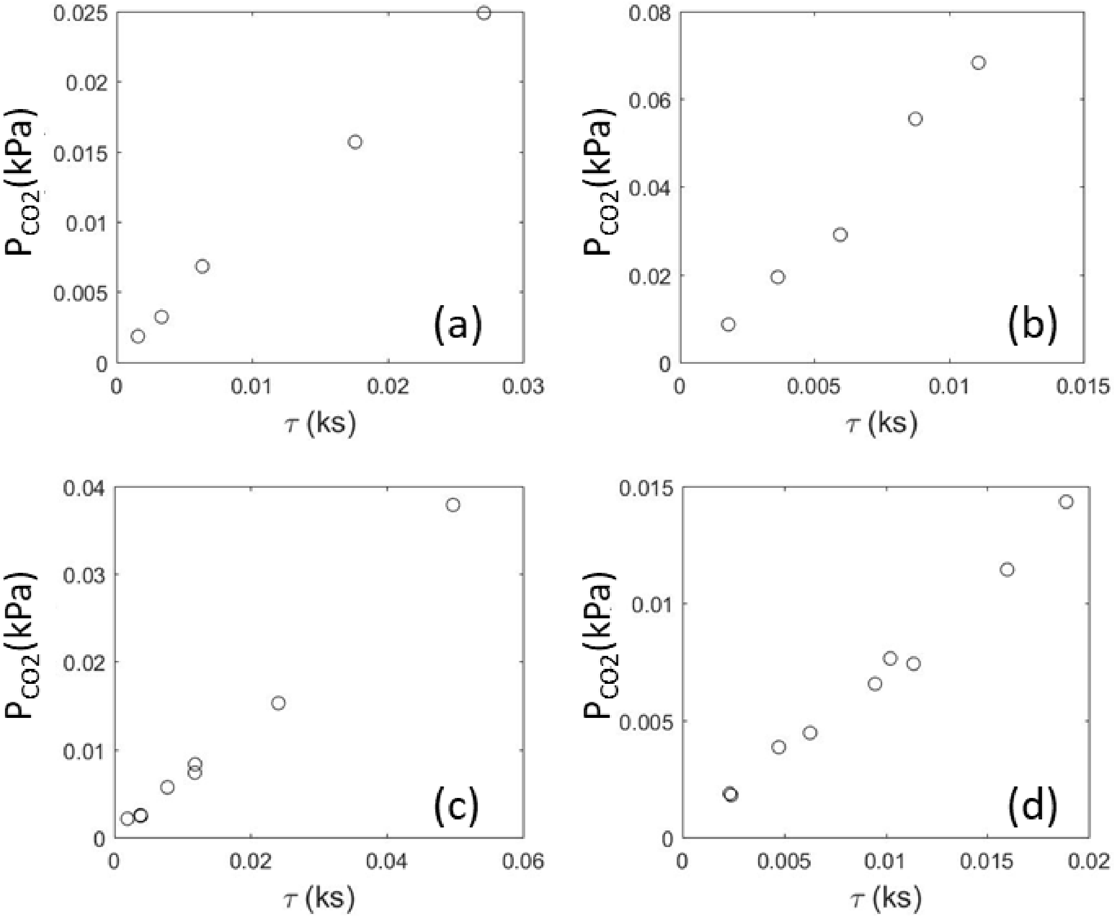

Figure 4-2. Partial pressure of CO_2 (P_{CO2}, kPa) vs. space time τ(ks) for (a) HPM-7/N-C-600, (b) HPM-15/N-C-600, (c) HPM-10/C, (d) HPM-20/C

Experiment 6 (co-feeding different amounts of MF, data not shown here) demonstrated that co-feeding MF does not affect the formation rate of DME, HCHO and DMM. CO and CO_2 increased a little as more MF was fed, indicating that very small amount of MF can react to CO and CO_2.

Experiment 7 (co-feeding various amounts of DMM, result shown in Table 4-2) showed that both forward and reverse reaction of $HCHO+2CH_3OH \leftrightarrow CH_3OCH_2OCH_3 + H_2O$ is significant under reaction conditions. Table 4-2 presented the partial pressure of all the reactants and products when 0 kPa, 0.5 kPa and 1 kPa of DMM were fed into the reactor for HPM-10/C. As shown, when 0.5 kPa DMM was introduced into the reactor, partial pressure of HCHO increased from 0.27kPa to 0.52kPa, indicating that some DMM reacted with water to form HCHO and CH_3OH. Partial pressure of MF and CO also increased because some of the HCHO further reacted into secondary products.

	feed 0 kpa DMM	**feed 0.5 kpa DMM**	**feed 1 kpa DMM**
P_{HCHO} (kPa)	0.27	0.52	0.72
P_{DME} (kPa)	0.10	0.11	0.13
P_{CH3OH} (kPa)	13.70	14.42	17.73
P_{MF} (kPa)	0.024	0.051	0.072
P_{DMM} (kPa)	0.05	0.12	0.23
P_{CO} (kPa)	0.007	0.013	0.016
P_{CO2} (kPa)	0.006	0.007	0.006

Table 4-2. Partial pressure of HCHO, DME, CH_3OH, MF, DMM, CO and CO_2 when 0 kPa, 0.5 kPa and 1 kPa of DMM is fed into the reactor. 170mg HPM-10/C, 220°C, 101kPa total pressure, 25sccm total flow rate, 15kPa CH_3OH, 20kPa O_2, 2.5kPa H_2O, balance He.

Combining information from experiment 5, 6 and 7, a network reaction for methanol oxidation and dehydration that involves every product is proposed. As shown in Scheme 4-1, this scheme is the same as the one proposed by Iglesia[24] and Tatibouet[30] except that CO and CO_2 are added to the network. CO is assumed to only come from HCHO in the reaction network, where in reality some CO might also come from secondary products, as shown by the result of experiment 6 (co-feeding different amounts of MF). CO_2 is assumed as a primary product, possibly coming from methanol reacting with oxygen on the support surface (both C and N-C-600 have some oxygen atoms on the surface as detected by XPS, shown in Chapter 2). However, in reality, some CO_2 formation could also come from burning of secondary products. Assumptions about CO and CO_2 were made so that the kinetic models were not too complicated for these two products. All the reactions in the network are listed below in Scheme 4-2 with correct stoichiometry.

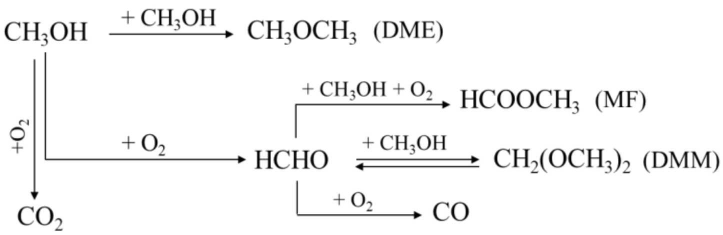

Scheme 4-1. Proposed reaction network for methanol oxidation and dehydration.

(1) $2CH_3OH \longrightarrow CH_3OCH_3(\boldsymbol{DME}) + H_2O$

(2) $CH_3OH + \frac{1}{2}O_2 \longrightarrow HCHO + H_2O$

(3) $HCHO + CH_3OH + \frac{1}{2}O_2 \longrightarrow HCOOCH_3(\boldsymbol{MF}) + H_2O$

(4) $HCHO + 2CH_3OH \longleftrightarrow CH_3OCH_2OCH_3(\boldsymbol{DMM}) + H_2O$

(5) $HCHO + \frac{1}{2}O_2 \longrightarrow CO + H_2O$

(6) $CH_3OH + \frac{3}{2}O_2 \longrightarrow CO_2 + 2H_2O$

Scheme 4-2. Individual reactions in methanol oxidation and dehydration.

4.3.2 Proposed mechanisms and rate equations for DME, HCHO, MF and DMM

Mechanisms for the formation of DME, HCHO, MF and DMM proposed for constructing kinetics models will be shown in this section. A general assumption for the mechanisms proposed here is that two different sites are involved, Site a (acid site) and Site b (oxidation site), where DME and DMM are assumed to form on Site a (H^+), whereas HCHO and MF are assumed to form on Site b (oxidation site).

The reaction steps happening on Site a are listed in Scheme 4-3. The steps for DME formation listed here are largely based on the theoretical and kinetics studies by Iglesia and co-workers

[24], where they suggested that formation of protonated methanol monomer and dimer are involved to produce DME. One extra step that involved water competing with methanol to form a protonated water-methanol dimer is added to better portray DME formation here, because it has been found in our kinetics study that adding water has a negative effect on DME production rate with all the HPM/C and HPM/N-C-600 catalysts tested (results shown in Figure 4-3 to Figure 4-10, discussed in section 4.3.3). The steps involved in DMM formation are also proposed in Scheme 4-3, which involved hemiacetal formation and hemiacetal condensation with another methanol to form DMM. Detailed steps are described below.

The first step involves the quasi-equilibrated adsorption of CH_3OH ($CH_3OH \cdot s_a$) at Site a (S_a, the acid site) (Step 1, Scheme 4-3). The adsorbed CH_3OH ($CH_3OH \cdot s_a$) can then react with another CH_3OH or a H_2O molecule in quasi-equilibrated steps, which involves proton transfer from POM to $CH_3OH \cdot s_a$ to form protonated dimer ($CH_3OH \cdot s_a \cdot CH_3OH\ and\ \ CH_3OH \cdot s_a \cdot H_2O$) (Step 2 and 3, Scheme 4-3). The protonated methanol dimer ($CH_3OH \cdot s_a \cdot CH_3OH$) can then eliminate a H_2O molecule and form DME (Step 4, Scheme 4-3).

For DMM formation, here we proposed that the adsorbed CH_3OH ($CH_3OH \cdot s_a$) can react with HCHO formed on oxidation sites (will be discussed later in Scheme 4-5) and form adsorbed hemiacetal ($HOCH_2OCH_3 \cdot s_a$) (Step 5, Scheme 4-3), and this adsorbed hemiacetal ($HOCH_2OCH_3 \cdot s_a$) can react with another CH_3OH and eliminate a H_2O molecule to form adsorbed DMM ($CH_3OCH_2OCH_3 \cdot s_a$) (Step 6, Scheme 4-3). DMM can then desorb from the surface (Step 7, Scheme 4-3).

(1) $CH_3OH + s_a \overset{K_1}{\Longleftrightarrow} CH_3OH \cdot s_a$

(2) $CH_3OH \cdot s_a + CH_3OH \overset{K_2}{\Longleftrightarrow} CH_3OH \cdot s_a \cdot CH_3OH$

(3) $CH_3OH \cdot s_a + H_2O \overset{K_3}{\Longleftrightarrow} CH_3OH \cdot s_a \cdot H_2O$

(4) $CH_3OH \cdot s_a \cdot CH_3OH \xrightarrow{k_4} CH_3OCH_3\ (DME) + H_2O + s_a$

(8) $CH_3OH \cdot s_a + HCHO \overset{K_8}{\Longleftrightarrow} HOCH_2OCH_3 \cdot s_a$

(9) $HOCH_2OCH_3 \cdot s_a + CH_3OH \underset{k_{-9}}{\overset{k_9}{\Longleftrightarrow}} CH_3OCH_2OCH_3 \cdot s_a + H_2O$

(10) $CH_3OCH_2OCH_3(DMM) + s_a \overset{K_{10}}{\Longleftrightarrow} CH_3OCH_2OCH_3 \cdot s_a$

Scheme 4-3. Proposed reaction steps on Site a (acid site), step number 5-7 are used to describe oxidation steps in Scheme 4-5 and do not appear here. K_i and k_i represent the equilibrium constant and rate constants for Step i.

Based on steps proposed in Scheme 4-3, if we assume that the adsorbed methanol monomer ($CH_3OH \cdot s_a$), protonated methanol dimer ($CH_3OH \cdot s_a \cdot CH_3OH$) and the protonated methanol-water dimer ($CH_3OH \cdot s_a \cdot H_2O$) are the most abundant reactive intermediate, and that Step 1, 2, 3, 5 are at quasi-equilibrium, whereas Step 4 and Step 6 are rate determining for DME and DMM formation respectively, then the rate equation for DME and DMM formation can be derived as shown by Scheme 4-4. K_i and k_i in these equations correspond to those listed in Scheme 4-3. Note that equilibrium constants K_1, K_2 and K_3 are used in both DME and DMM rate calculation, because Step 1, 2, 3 are involved in both DME and DMM formation.

$$K_1 = \frac{[\,CH_3OH \cdot s_a]}{P_{CH3OH} * [s_a]}$$

$$K_2 = \frac{[\,CH_3OH \cdot s_a \cdot CH_3OH]}{P_{CH3OH} \ * [CH_3OH \cdot s_a]}$$

$$K_3 = \frac{[\,H_2O \cdot s_a \cdot CH_3OH]}{P_{H2O} \ * [CH_3OH \cdot s_a]}$$

$$K_8 = \frac{[HOCH_2OCH_3 \cdot s_a]}{P_{HCHO} \ * [CH_3OH \cdot s_a]}$$

$$K_{10} = \frac{[\,CH_3OCH_2OCH_3 \cdot s_a]}{P_{DMM} * [s_a]}$$

$$[\,CH_3OH \cdot s_a] + [\,CH_3OH \cdot s_a \cdot CH_3OH] + [\,H_2O \cdot s_a \cdot CH_3OH] = L_a$$

$$r_{DME} = k_4 * \ [\,CH_3OH \cdot s_a \cdot CH_3OH]$$

$$\frac{r_{DME}}{L_a} = \frac{k_4 * K_1 * K_2 * P_{CH3OH}{}^2}{K_1 * P_{CH3OH} + K_1 * K_2 * P_{CH3OH}{}^2 + K_1 * K_3 * P_{CH3OH} * P_{H2O}}$$

$$= \frac{k_4 * K_2 * P_{CH3OH}}{1 + K_2 * P_{CH3OH} + K_3 * P_{H2O}}$$

$$= \frac{m_1 * P_{CH3OH}}{1 + m_4 * P_{CH3OH} + m_5 * P_{H2O}}$$

$$in\,which\ \ m_1 = k_4 * K_2\ , m_4 = K_2,\ \ m_5 = K_3\ ,\ \frac{m_1}{m_4} = k_4$$

$$r_{DMM} = k_9 * [HOCH_2OCH_3 \cdot s_a] * P_{CH3OH} - k_{-9} * [\,CH_3OCH_2OCH_3 \cdot s_a] * P_{H2O}$$

$$\frac{r_{DMM}}{L_a} = \frac{k_9 * K_1 * K_8 * P_{HCHO} * P_{CH3OH}{}^2 - k_{-9} * K_{10} * P_{DMM} * P_{H2O}}{K_1 * P_{CH3OH} + K_1 * K_2 * P_{CH3OH}{}^2 + K_1 * K_3 * P_{CH3OH} * P_{H2O}}$$

$$= \frac{m_3 * (m_{10} * P_{HCHO} * P_{CH3OH}{}^2 - P_{DMM} * P_{H2O})}{P_{CH3OH} * (1 + m_4 * P_{CH3OH} + m_5 * P_{H2O})}$$

$$in\,which\, m_3 = \ \frac{k_{-9}K_{10}}{K_1}\ , m_{10} = \frac{K_1K_8K_9}{K_{10}}\ \ (K_9 = \frac{k_9}{k_{-9}}), m_4 = K_2,\ \ m_5 = K_3$$

Scheme 4-4. Derivation of DME and DMM rate equations if we assume that the adsorbed methanol monomer ($CH_3OH{\cdot}s_a$), protonated methanol dimer ($CH_3OH{\cdot}s_a{\cdot}CH_3OH$) and the protonated methanol-water dimer ($CH_3OH{\cdot}s_a{\cdot}H_2O$) are the most abundant reactive intermediates, and that Steps 1, 2, 3, 5 are at quasi-equilibrium whereas Step 4 and Step 6 are rate determining for DME and DMM formation, respectively. L_a is the total number of site a on the catalyst. K_i and k_i in these equations correspond to those listed in Scheme 4-3. m_i are the parameters used in the kinetic models during calculation.

The reactions on site b are listed in Scheme 4-5. Site b (oxidation site) is assumed to be bridging oxygen in the POM structure with H^+ nearby, which is consistent with the model that Iglesia and co-workers used in their kinetics and DFT study [24]. The elementary steps Iglesia proposed for the formation of formaldehyde was adopted here too, as shown in Steps 5, 6 and 7 in Scheme 4-5. The H-abstraction step was assumed to happen from an undissociated adsorbed methanol molecule, rather than a methoxy, which is often assumed as intermediate in methanol oxidation over transition metal oxides. A possible MF formation mechanism is then proposed that involves the formation of hemiacetal and H-abstraction from hemiacetal to form MF.

Step 5 and 6 in Scheme 4-5 involved CH_3OH and H_2O competing to adsorb on the same oxidation site, bridging oxygen in the POM structure with H^+ nearby, so that an additional H-bond can be formed between the oxygen from CH_3OH and the H^+ from POM and thus further stabilize the structure. This step is likely relevant to the relationship between methanol oxidation activity and acid site quantity and strength shown in Chapter 3, since the acid site is involved. After CH_3OH is adsorbed on the oxidation site, subsequent irreversible steps followed with the breakage of C-H bond in methanol and form HCHO (Step 7, Scheme 4-5).

As mentioned earlier in steps that occur on the acid site, after HCHO is produced on oxidation sites, hemiacetal can be formed and then condense with another methanol to make DMM. In the meantime, on the oxidation site, it is proposed here that hemiacetal can undergo another H-abstraction step to form MF, eliminating one H_2O molecule (Step 12, Scheme 4-5).

(5) $CH_3OH + s_b \overset{K_5}{\Longleftrightarrow} CH_3OH \cdot s_b$

(6) $H_2O + s_b \overset{K_6}{\Longleftrightarrow} H_2O \cdot s_b$

(7) $CH_3OH \cdot s_b + \frac{1}{2}O_2 \xrightarrow{k_7} HCHO + H_2O + s_b$

(11) $CH_3OH \cdot s_b + HCHO \overset{K_{11}}{\Longleftrightarrow} HOCH_2OCH_3 \cdot s_b$

(12) $HOCH_2OCH_3 \cdot s_b + \frac{1}{2}O_2 \xrightarrow{k_{12}} HCOOCH_3 + H_2O \cdot s_b$

Scheme 4-5. Proposed reaction steps on Site b (oxidation site). K_i and k_i represent the equilibrium constant and rate constants for Step i. Step number 1-4 and 8-9 are used to describe dehydration steps in Scheme 4-3 and do not appear here.

Based on steps proposed in Scheme 4-5, if we assume that the concentration of adsorbed hemiacetal ($HOCH_2OCH_3 \cdot s_b$) is small, and that Steps 5, 6, 11 are in quasi-equilibrium whereas Step 7 and Step 11 are the rate determining steps for HCHO and MF respectively, then the rate of formation for HCHO and MF can be derived as shown in Scheme 4-6. Note that equilibrium constants K_5 and K_6 are used in both HCHO and MF rate calculation, because Steps 5 and 6 in Scheme 4-5 are involved in both HCHO and MF formation.

$$K_5 = \frac{[\,CH_3OH \cdot s_b]}{P_{CH3OH} * [s_b]}$$

$$K_6 = \frac{[\,H_2O \cdot s_b]}{P_{H2O} * [s_b]}$$

$$K_{11} = \frac{[HOCH_2OCH_3 \cdot s_b]}{P_{HCHO} \ * [CH_3OH \cdot s_b]}$$

$$[\,CH_3OH \cdot s_b] + [\,H_2O \cdot s_b] + [s_b] = L_b$$

$$r_{ODH} = k_7 * \ [\,CH_3OH \cdot s_b]$$

$$\frac{r_{ODH}}{L_b} = \frac{k_7 * K_5 * P_{CH3OH}}{1 + K_5 * P_{CH3OH} + K_6 * P_{H2O}}$$

$$= \frac{m_7 * P_{CH3OH}}{1 + m_8 * P_{CH3OH} + m_9 * P_{H2O}}$$

where $m_7 = k_7 * K_5$, $m_8 = K_5$, $m_9 = K_6$, $\frac{m_7}{m_8} = k_7$

$$r_{MF} = k_{12} * \ [HOCH_2OCH_3 \cdot s_b]$$

$$\frac{r_{MF}}{L_b} = \frac{k_{12} * K_5 * K_{11} * P_{HCHO} * P_{CH3OH}}{1 + K_5 * P_{CH3OH} + K_6 * P_{H2O}}$$

$$= \frac{m_2 * P_{HCHO} * P_{CH3OH}}{1 + m_8 * P_{CH3OH} + m_9 * P_{H2O}}$$

$where \ \ m_2 = k_{12} * K_5 * K_{11}, m_8 = K_5, m_9 = K_6 \ , \frac{m_2}{m_8} = k_{12} * K_{11}$

Scheme 4-6. Rate expression derivation for HCHO and MF, if we assume that the concentration of adsorbed hemiacetal ($HOCH_2OCH_3 \cdot s_b$) is small and that Steps 5, 6, 11 are in quasi-equilibrium, whereas Step 7 and Step 11 are the rate determining steps for HCHO and MF respectively. L_b is total number of site b on the surface of the support. K_i and k_i in these equations correspond to those listed in Scheme 4-5. m_i are the parameters used in the kinetic models during calculation.

For CO, a rate equation is proposed based on the assumption that CO comes only from HCHO and is first order in HCHO. For CO_2, a rate equation is proposed assuming that CO_2 comes only from methanol and that during this process methanol adsorb on a different site (possibly a basic site). See Equation 4-3 and Equation 4-4 for rate expressions proposed for CO and CO_2

Equation 4-2: Rate expressions proposed for CO

$$r_{CO} = m_6 * P_{HCHO}$$

Equation 4-3: Rate expressions proposed for CO_2

$$r_{CO2} = \frac{m_{14} * P_{CH3OH}}{1 + m_{15} * P_{CH3OH}}$$

4.3.3 Kinetic models for DME, HCHO, MF, DMM, CO and CO_2

Kinetic models for DME, HCHO, MF, DMM, CO and CO_2 were constructed based on mass balance in a packed-bed reactor (Equation 4-5) as well as the rate equations proposed in section 4.3.2. Combining the mass balance and the rate equations, and using $X_i(yield)$ as well as $X_{CH3OH}(conversion) = \frac{P_{CH3OH}}{P_{CH3OH,0}}$ to rewrite partial pressure of both reactants and products (P_i), we obtain equations 1-6 in Scheme 4-7, where the variables in each equation are either yield or conversion. Equations 7 and 8 are expressions of conversion (based on methanol) and yield for water calculated based on the stoichiometric values of all the reactions in Scheme 4-7.

Equation 4-4: Mass balance in packed-bed reactor

$$\frac{dX_i}{d\tau} = r_i$$

Where $X_i(\text{yield}) = \frac{P_i}{P_{CH3OH,0}}$, P_i is the partial pressure of a product in kPa, $P_{CH3OH,0}$ is the initial partial pressure of methanol in kPa. τ is space time defined in Equation 4-1.

(1) $$\frac{dX_{DME}}{d\tau} = \frac{m_1 * P_{CH3OH,0} * (1 - X_{CH3OH})}{1 + m_4 * P_{CH3OH,0} * (1 - X_{CH3OH}) + m_5 * (P_{H2O,0} + P_{CH3OH,0} * X_{H2O})}$$

(2) $$\frac{dX_{HCHO}}{d\tau} = \frac{m_7 * P_{CH3OH,0} * (1 - X_{CH3OH})}{1 + m_8 * P_{CH3OH,0} * (1 - X_{CH3OH}) + m_9 * (P_{H2O,0} + P_{CH3OH,0} * X_{H2O})} - \frac{dX_{MF}}{d\tau} - \frac{dX_{DMM}}{d\tau} - \frac{dX_{CO}}{d\tau}$$

(3) $$\frac{dX_{MF}}{d\tau} = \frac{m_2 * P_{CH3OH,0} * X_{HCHO} * P_{CH3OH,0} * (1 - X_{CH3OH})}{1 + m_8 * P_{CH3OH,0} * (1 - X_{CH3OH}) + m_9 * (P_{H2O,0} + P_{CH3OH,0} * X_{H2O})}$$

(4) $$\frac{dX_{DMM}}{d\tau} = \frac{m_3 * (m_{10} * P_{CH3OH,0} * X_{HCHO} * \left(P_{CH3OH,0} * (1 - X_{CH3OH})\right)^2 - P_{CH3OH,0} * X_{DMM} * (P_{H2O,0} + P_{CH3OH,0} * X_{H2O}))}{P_{CH3OH,0} * (1 - X_{CH3OH}) * (1 + m_4 * P_{CH3OH,0} * (1 - X_{CH3OH}) + m_5 * (P_{H2O,0} + P_{CH3OH,0} * X_{H2O}))}$$

(5) $$\frac{dX_{CO}}{d\tau} = m_6 * P_{CH3OH,0} * X_{HCHO}$$

(6) $$\frac{dX_{CO2}}{d\tau} = \frac{m_{14} * P_{CH3OH,0} * (1 - X_{CH3OH})}{1 + m_{15} * P_{CH3OH,0} * (1 - X_{CH3OH})}$$

(7) $$X_{CH3OH}\ (conversion) = 2 * X_{DME} + X_{HCHO} + 2 * X_{MF} + 3 * X_{DMM} + X_{CO} + X_{CO2}$$

(8) $$X_{H2O}(yield) = X_{DME} + X_{HCHO} + 2 * X_{MF} + 2 * X_{DMM} + 2 * X_{CO} + 2 * X_{CO2}$$

Scheme 4-7. Kinetic models for DME, HCHO, MF, DMM, CO and CO_2 based on the mass balance for packed-bed reactor and rate expressions derived in 4.3.2.

The eight equations shown in Scheme 4-7 were solved simultaneously in Matlab with initial conditions given as $P_{CH3OH,0}$ (initial partial pressure of CH_3OH) and $P_{H2O,0}$ (initial partial pressure of H_2O). The calculation is stopped when space time $\tau = \tau_{end} = \frac{W}{F_{CH3OH,\,0}}$, where W is total amount of catalyst in the reactor, and $F_{CH3OH,\,0}$ is the initial flow rate of methanol. For example, for 32.6mg HPM-20/C catalyst with 5kPa initial partial pressure of CH_3OH, 101kPa total pressure and 20sccm total flow rate, τ_{end} is calculated to be 4.8s based on the calculation process in Equation 4-6.

Equation 4-5: τ_{end} calculation for 32.6mg HPM-20/C catalyst with 5kPa initial partial pressure of CH_3OH, 101kPa total pressure and 20sccm total flow rate.

$$\tau_{end} = \frac{W}{F_{CH3OH,\,0}} = \frac{\dfrac{32.6mg * 20wt\%}{1.825mg/\mu mol}}{\dfrac{5\ kPa}{101\ kPa} * 20\ sccm * \dfrac{745\ \mu mol/ks}{sccm}} = 4.8\ s$$

where W is total amount of catalyst in the reactor, and $\boldsymbol{F_{CH3OH,\,0}}$ is the initial flow rate of methanol.

The result of experiment 1 (vary total pressure) and the corresponding model prediction for HPM-10/C, HPM-20/C, HPM-7/N-C-600 and HPM-15/N-C-600 are shown in Figure 4-3, Figure 4-4, Figure 4-5 and Figure 4-6 respectively, where partial pressure of both reactants and products are plotted against conversion. Model prediction of experiment 1 (vary total flow rate) for each catalyst involved one pair of initial conditions ($P_{CH3OH,0}$, $P_{H2O,0}$), and 1000 different τ_{end} values were used to generate the smooth blue curve in Figure 4-3 to Figure 4-6. Note that the partial pressure of ODH products (HCHO+MF+DMM+CO) is also plotted, which stands for the total amount of HCHO formed on the oxidation site including those that further reacted to be secondary products.

From Figure 4-3 to Figure 4-6 one can tell that overall the model constructed from the mechanisms proposed in section 4.3.2 can predict the experimental data well. Taking HPM-10/C as an example (Figure 4-3), the curvature of the model prediction for DME, HCHO, DMM and MF are all consistent with the experimental results. The CO and CO_2 model predictions deviated from the experimental data at higher conversions, meaning that the assumptions we made for these products are over-simplified. We have assumed that CO only came from HCHO, but it is possible that some of the CO products also come from other secondary products. For example, when different amount of MF is fed into the system together with the reactants, a small increase of CO signal in the GC is observed. The same idea can apply to CO_2, which we have assumed is produced directly from methanol, whereas it may also arise from the burning of secondary products, which could account for the difference between model prediction and experimental data at higher conversions.

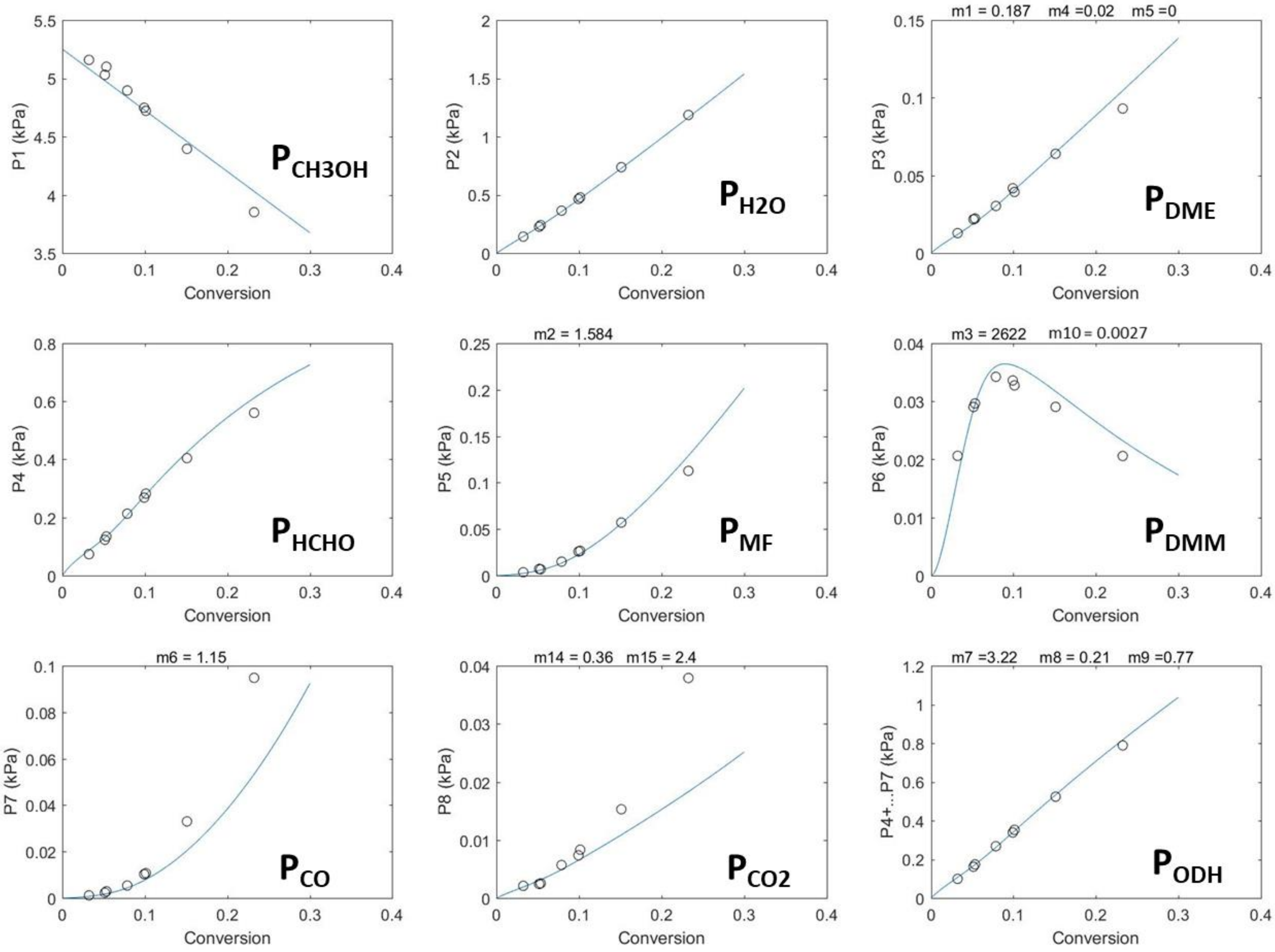

Figure 4-3. Partial pressure of CH_3OH, H_2O, DME, HCHO, MF, DMM, CO, CO_2 and ODH products vs. conversion. HPM-10/C 170mg, 220℃, 101kPa, 5-120sccm, 20kPa O_2, 0kPa H_2O, 5 kPa CH_3OH, balance He (○: experimental data, —: model prediction)

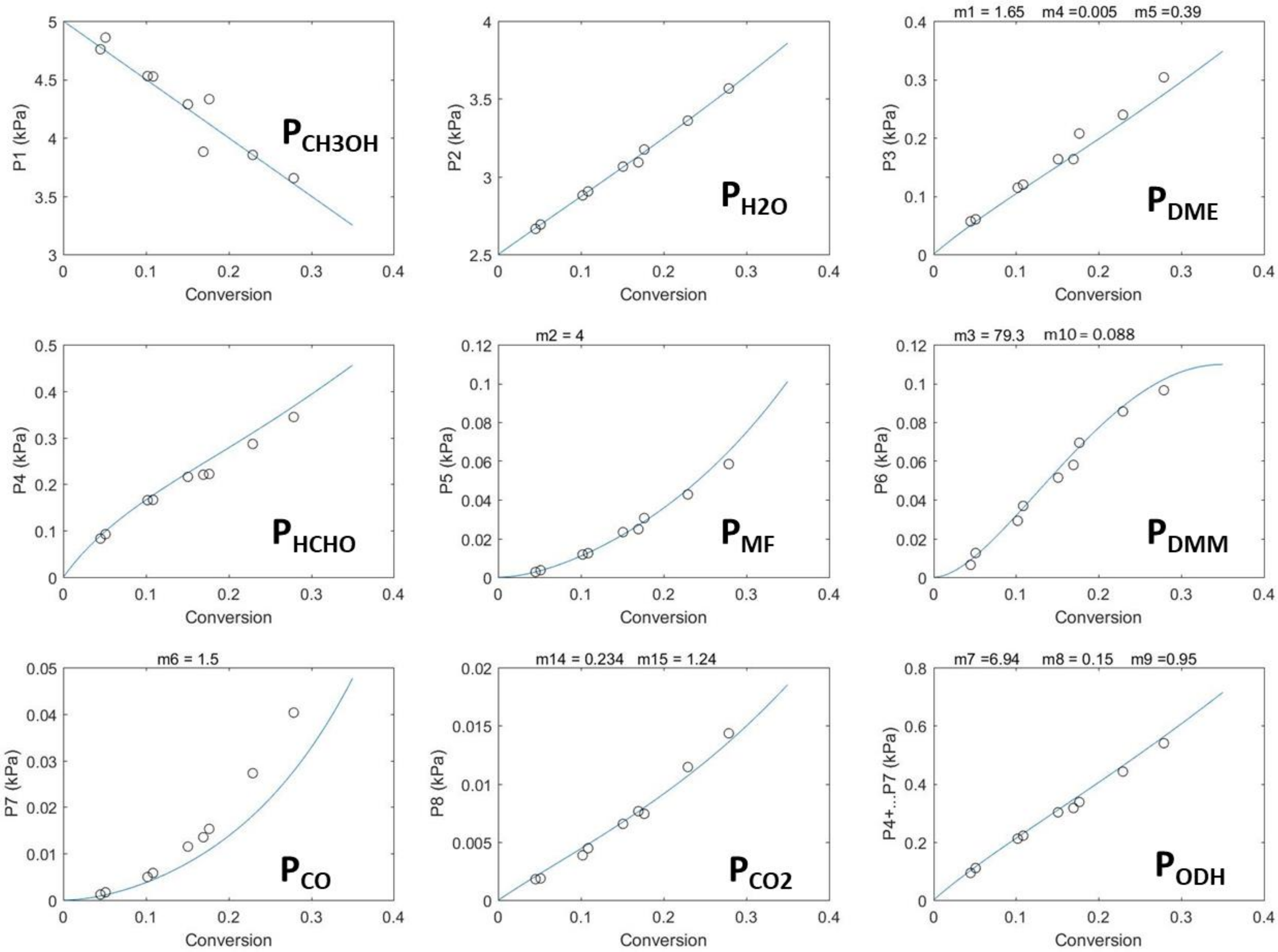

Figure 4-4. Partial pressure of CH_3OH, H_2O, DME, HCHO, MF, DMM, CO, CO_2 and ODH products vs. conversion. HPM-20/C 32.6mg, 220°C, 101kPa, 5-40sccm, 20kPa O_2, 2.5kPa H_2O, 5 kPa CH_3OH, balance He (○: experimental data, —: model prediction)

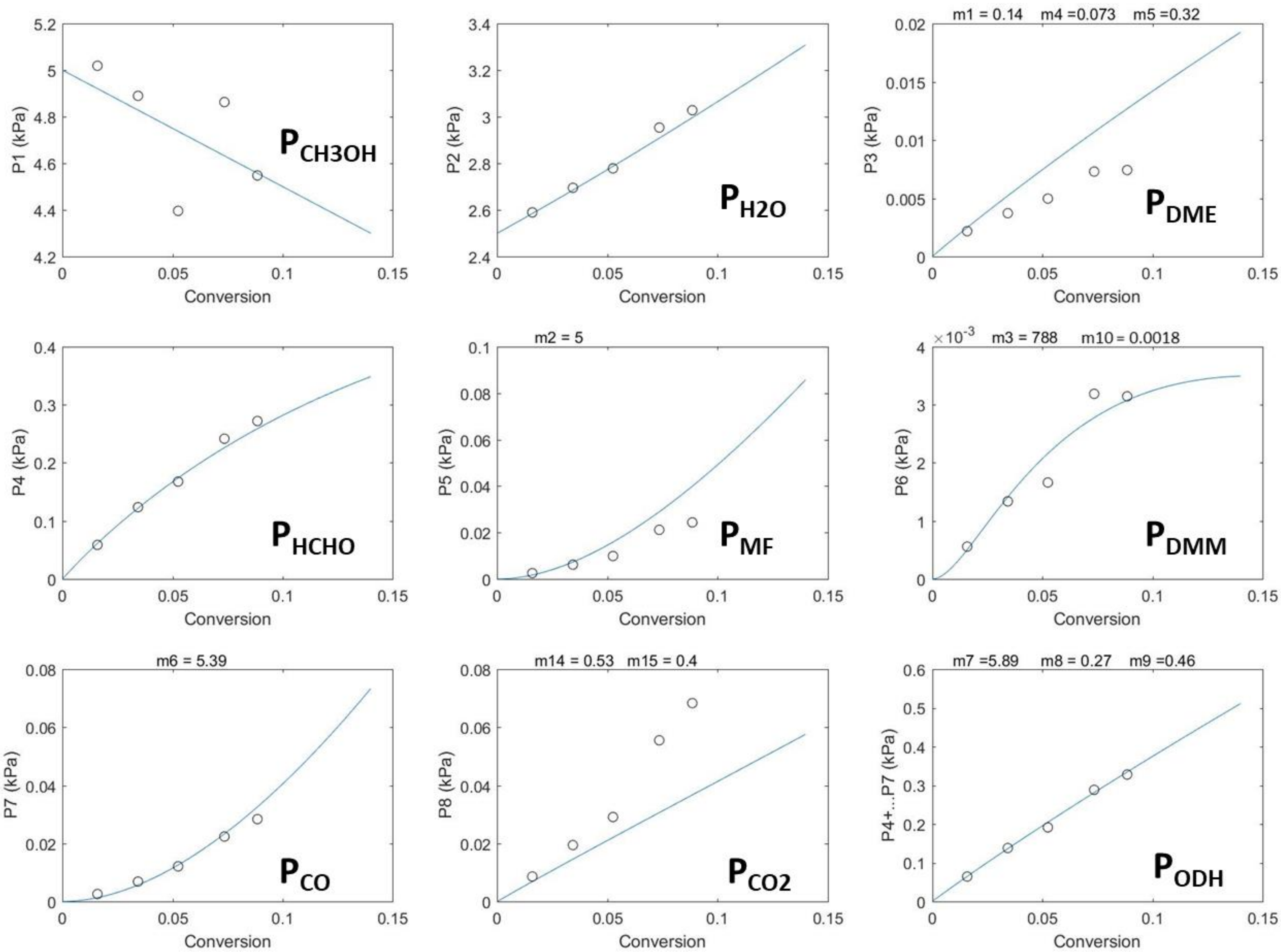

Figure 4-5. Partial pressure of CH_3OH, H_2O, DME, HCHO, MF, DMM, CO, CO_2 and ODH products vs. conversion. HPM-7/N-C-600 53.8mg, 220°C, 101kPa, 6-30sccm, 20kPa O_2, 2.5kPa H_2O, 5 kPa CH_3OH, balance He (○: experimental data, —: model)

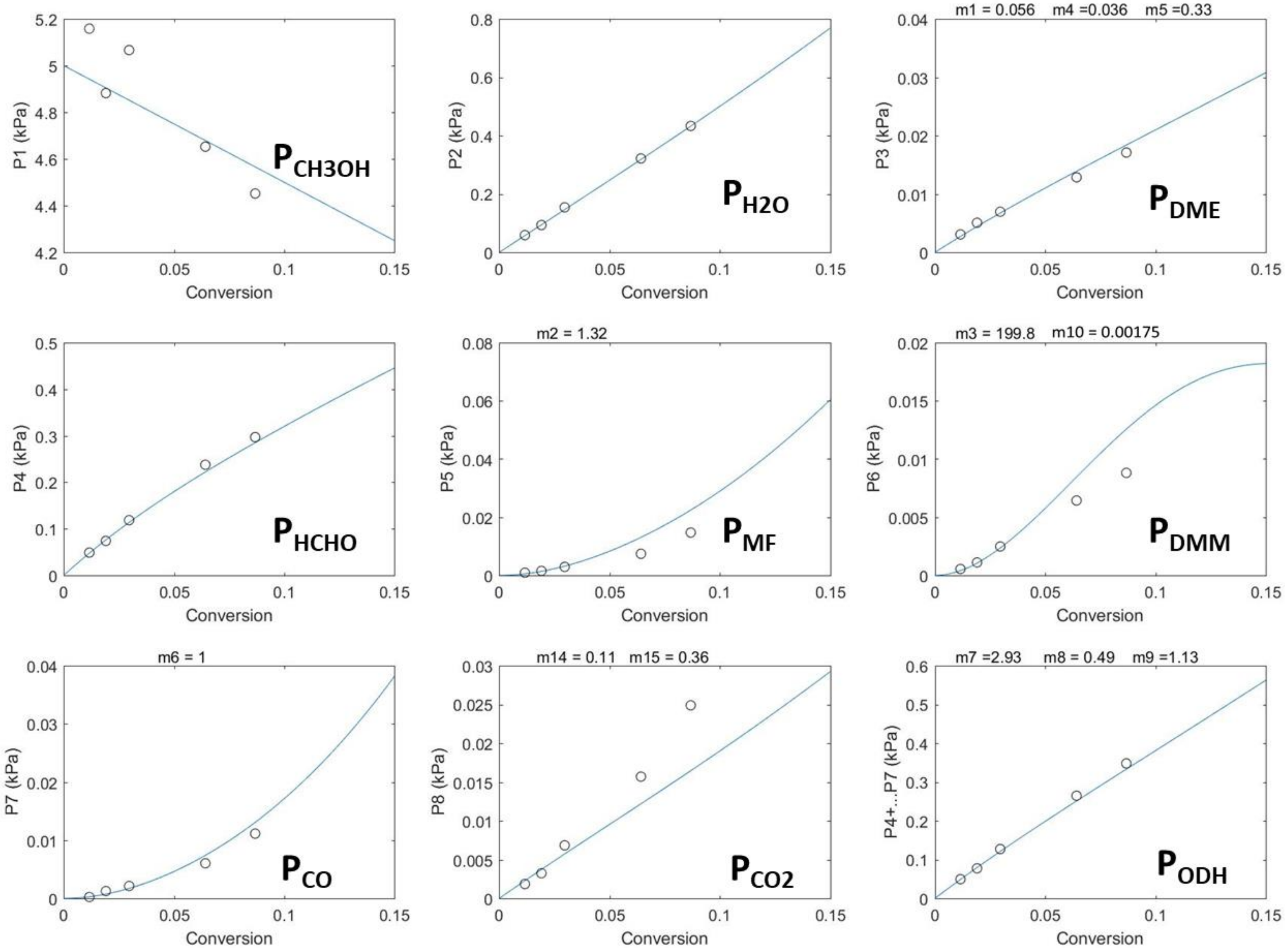

Figure 4-6. Partial pressure of CH_3OH, H_2O, DME, HCHO, MF, DMM, CO, CO_2 and ODH products vs. conversion. HPM-15/N-C-600 60mg, 220℃, 101kPa, 5-80sccm, 20kPa O_2, 0 kPa H_2O, 5 kPa CH_3OH, balance He (○: experimental data, —: model prediction)

The result of experiment 3 (vary methanol initial pressure with 0 kPa H_2O) and experiment 4 (vary methanol initial pressure with 2.5 kPa H_2O) as well as the corresponding model prediction for HPM-10/C, HPM-20/C, HPM-7/N-C-600 and HPM-15/N-C-600, are shown in Figure 4-7, Figure 4-8, Figure 4-9 and Figure 4-10 respectively, with partial pressure for both reactants and products plotted against methanol initial pressure. Model prediction of experiments 3 and 4 (vary methanol initial pressure with 0 kPa or 2.5 kPa H_2O) for each catalyst involved one pair of initial conditions ($P_{CH3OH,0}$, $P_{H2O,0}$) for each experimental data point. Specific τ_{end} values calculated by Equation 4-6 were used to get model prediction result (hollow points) in Figure 4-7 to Figure 4-10.

In Figure 4-7 to Figure 4-10, two sets of curves are shown in each subplot, representing the effect of co-feeding 2.5 kPa water on each product. The 2.5 kPa curve lies below the 0 kPa curve in the case of DME, HCHO, DMM and MF, indicating that adding 2.5 kPa H_2O has a negative effect on the rate for these products, which is consistent with the proposed mechanism (Scheme 4-3 and Scheme 4-5) where water is competing with methanol on both oxidation and acid sites. For CO and CO_2, the water effect is less obvious, possibly due to the more complicated nature of their formation mechanisms.

Overall the models constructed using the proposed mechanisms in Section 4.3.2 have done a good job predicting the reaction rate under different methanol and water conditions.

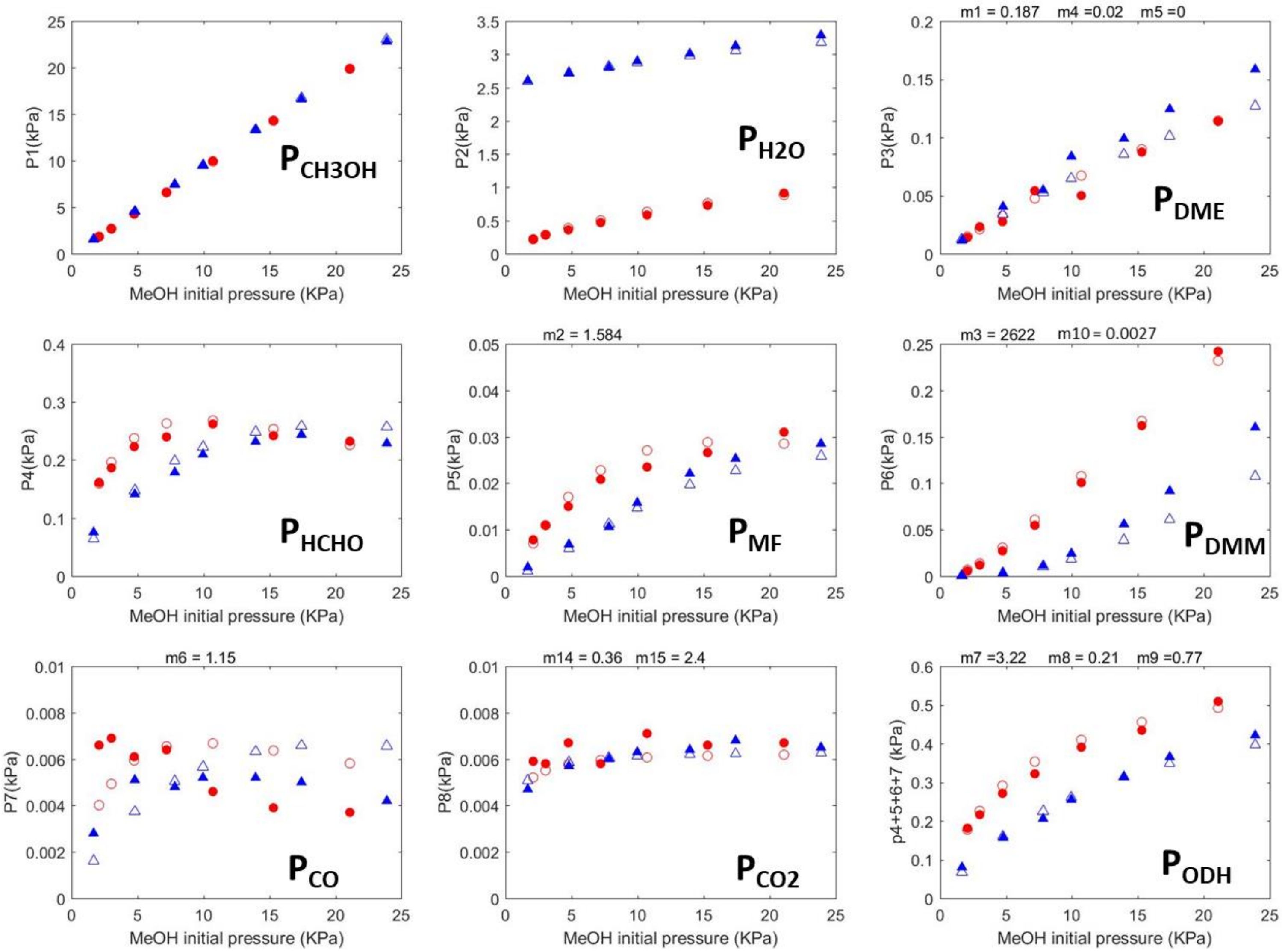

Figure 4-7. Partial pressure of CH_3OH, H_2O, DME, HCHO, MF, DMM, CO, CO_2 and ODH products vs. CH_3OH initial pressure. HPM-10/C 170mg, 220°C, 101kPa, 30sccm, 20kPa O_2, 0kPa H_2O (●: experimental data, ○: model prediction) or 2.5kPa H_2O (▲: experimental data, △: model prediction), 2.5-30 kPa CH_3OH, balance He, 4.5-11% conversion.

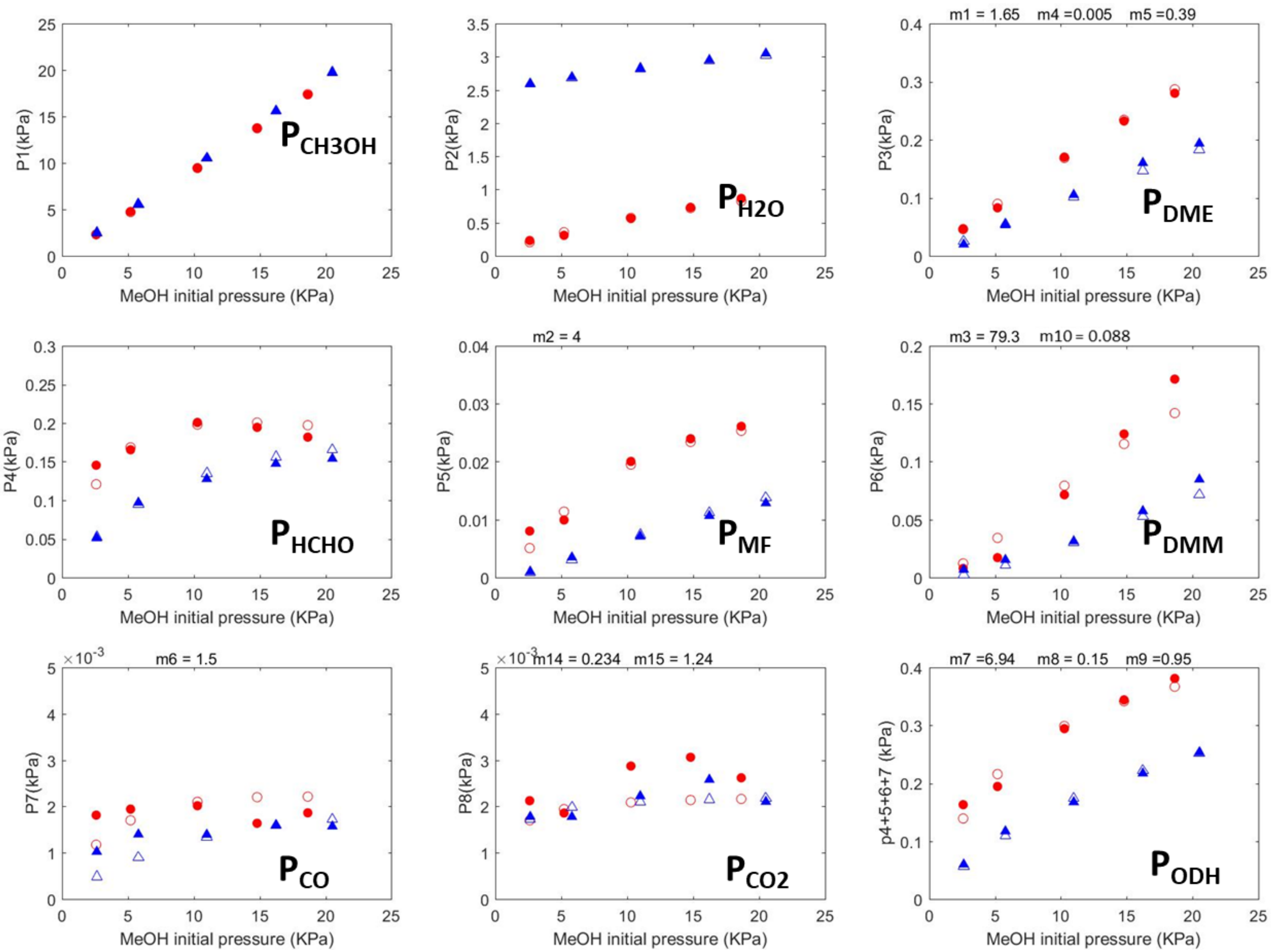

Figure 4-8. Partial pressure of CH_3OH, H_2O, DME, HCHO, MF, DMM, CO, CO_2 and ODH products vs. CH_3OH initial pressure. HPM-20/C 32.6mg, 220°C, 101kPa, 30sccm, 20kPa O_2, 0kPa H_2O (●: experimental data, ○: model prediction) or 2.5kPa H_2O (▲: experimental data, △: model prediction), 2.5-25 kPa CH_3OH, balance He, 4 -11% conversion.

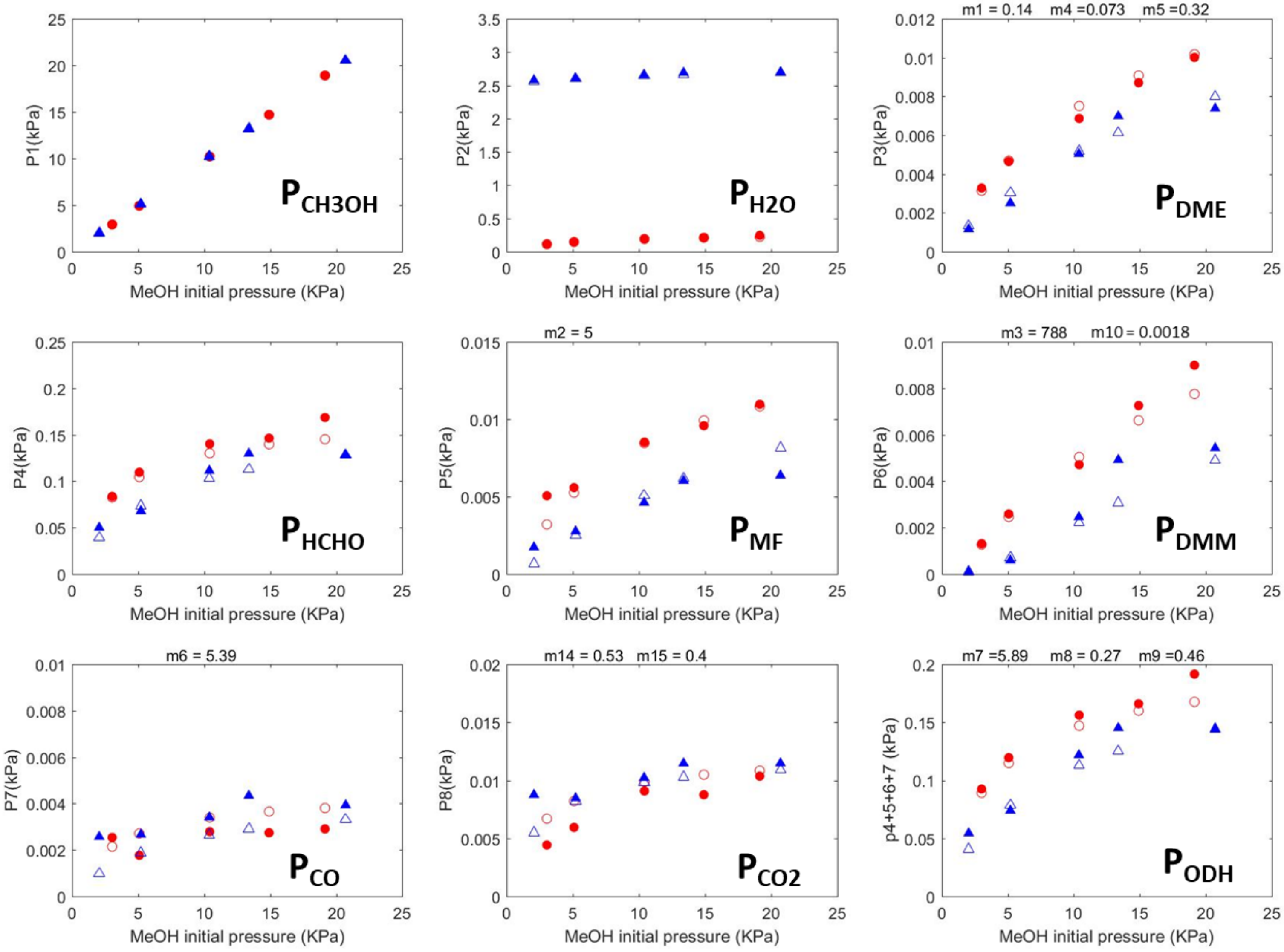

Figure 4-9. Partial pressure of CH_3OH, H_2O, DME, HCHO, MF, DMM, CO, CO_2 and ODH products vs. CH_3OH initial pressure. HPM-7/N-C-600 53.8mg, 220°C, 101kPa, 30sccm, 20kPa O_2, 0kPa H_2O (●: experimental data, ○: model prediction) or 2.5kPa H_2O (▲: experimental data, △: model prediction), 2.5-30 kPa CH_3OH, balance He.

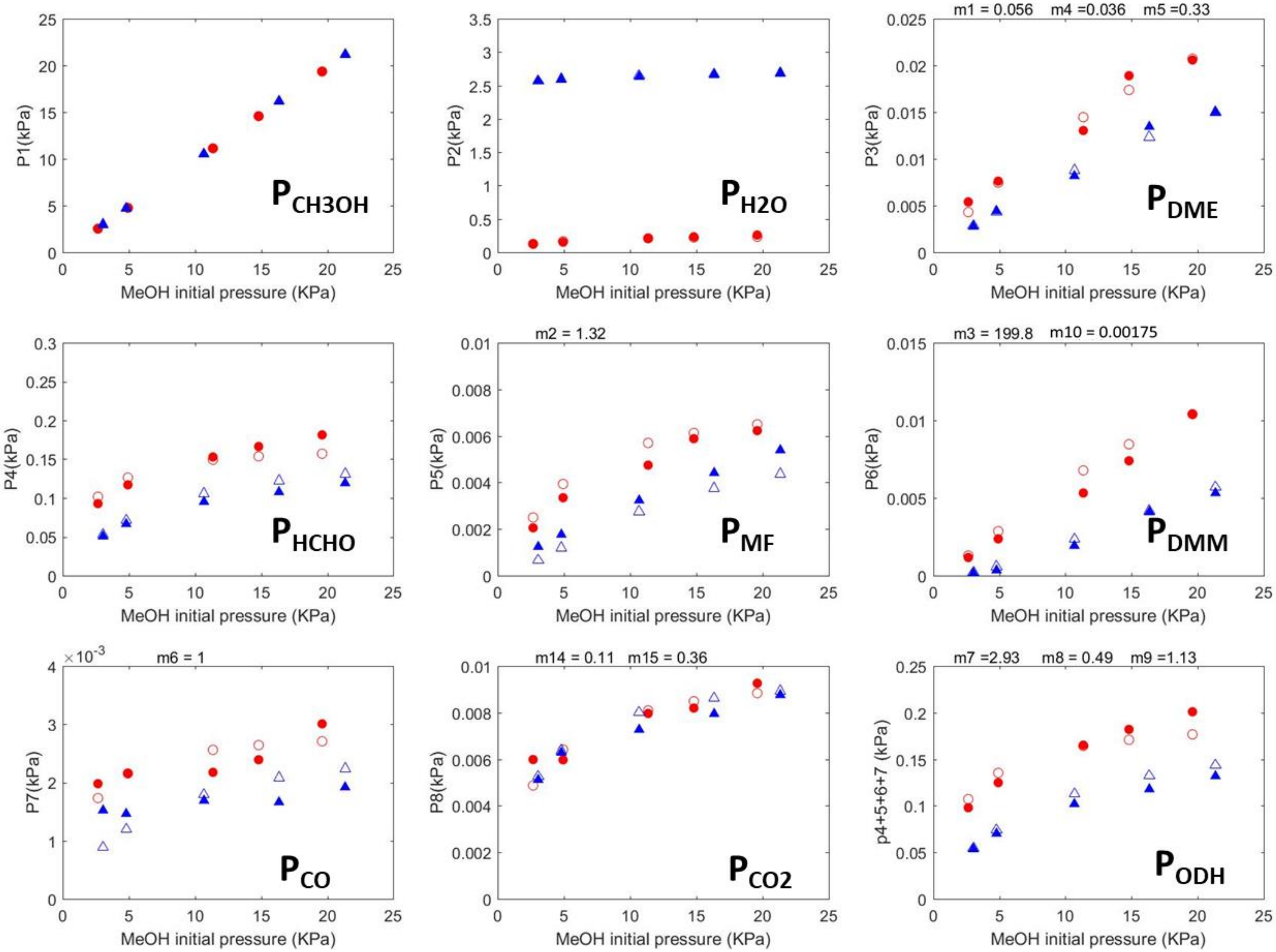

Figure 4-10. Partial pressure of CH_3OH, H_2O, DME, HCHO, MF, DMM, CO, CO_2 and ODH products vs. CH_3OH initial pressure. HPM-15/N-C-600 60mg, 220℃, 101kPa, 20sccm, 20kPa O_2, 0kPa H_2O (●: experimental data, ○: model prediction) or 2.5kPa H_2O(▲ : experimental data, △: model prediction), 2.5-25 kPa CH_3OH, balance He.

4.4 Discussion

Kinetic parameters for formation of DME, HCHO, MF and DMM will be presented and discussed in detail in this section.

Kinetic parameters involved in DME formation used in the model for each catalyst are listed in Table 4-3. As can be seen from the table, m_4 (K_2), the equilibrium constant for a second methanol adsorption to form protonated dimer is very small for all the four catalysts, especially for the carbon-based catalysts, for which only a range estimate can be obtained. This is consistent with the DME plot in Figure 4-7 and Figure 4-8, where the experimental data all fall in a first order region. This linear behavior suggests that the adsorbed methanol monomer dominates the surface.

Rate constants for the rate determining step for DME, calculated as the $k_4 = \frac{m_1}{m_4}$, are presented in row 5-7 of Table 4-3, normalized per POM, per H^+ measured by NH_3-TPD and per H^+ measured by butene chemisorption respectively. As shown in the table, even though only a range can be determined for the carbon-based catalysts, the trend among the four catalysts is still clear. The N-C-600 based catalysts have much smaller rate constant for DME than the carbon-based catalysts regardless of how the rate constant is normalized. This trend of rate constant is consistent with the DME TOF plot (Figure 3-3) presented in Chapter 3. The differences in DME TOF for HPM/C and HPM/N-C-600 catalysts appear to be largely due to the difference in rate constants (k_4). This difference in k_4 could be caused by the energy difference of the late ion-pair transition state that Iglesia proposed [24], or it could be caused by the energy of the protonated dimer

($CH_3OH \cdot s_a \cdot CH_3OH$). A comparison of the energy of protonated dimer cannot be made here because information about K_1 cannot be extracted from the model.

Mechanism and kinetic parameters		**HPM-7/ N-C-600** *(0.04 POM/nm^2)*	**HPM-15/ N-C-600** *(0.09 POM/nm^2)*	**HPM-10/ C** *(0.04 POM/nm^2)*	**HPM-20/ C** *(0.09 POM/nm^2)*
$CH_3OH + s_a \overset{K_1}{\Longleftrightarrow} CH_3OH \cdot s_a$ $CH_3OH \cdot s_a + CH_3OH \overset{K_2}{\Longleftrightarrow} CH_3OH \cdot s_a \cdot CH_3OH$ $CH_3OH \cdot s_a + H_2O \overset{K_3}{\Longleftrightarrow} CH_3OH \cdot s_a \cdot H_2O$ $\boldsymbol{CH_3OH \cdot s_a \cdot CH_3OH \xrightarrow{k_4} CH_3OCH_3\ (DME) + H_2O + s_a}$ $\frac{dX_{DME}}{d\tau} = \frac{m_1 * P_{CH3OH}}{1 + m_4 * P_{CH3OH} + m_5 * P_{H2O}}$	$m_1 = k_4 * K_2$ (kPa^{-1}ks^{-1})	0.14	0.056	0.187	1.65
	$m_4 = K_2$ (kPa^{-1})	0.073	0.036	0.007-0.02	0-0.005
	$m_5 = K_3$ (kPa^{-1})	0.32	0.33	0	0.39
	$\frac{m_1}{m_4} = k_4$ (ks^{-1}) per POM	1.9	1.6	9.4 - 26.7	>= 330
	$\frac{m_1}{m_4} = k_4$ (ks^{-1}) per H$^+$ butene chemisorption	3.3	3.1	7-20	>= 244
	$\frac{m_1}{m_4} = k_4$ (ks^{-1}) per H$^+$ NH$_3$-TPD	3.7	2	11.3-32.2	>= 221

Table 4-3. Kinetic parameters in DME formation.

Equilibrium constants and rate constant involved in formaldehyde production are listed in Table 4-4. Note that the rate equation for ODH products is shown on the left, which represents the rate of formation for formaldehyde if none of it further reacts into secondary products. As shown in row 3-4 in the table, the equilibrium constants for methanol adsorption $m_8(K_5)$ and water adsorption $m_9(K_6)$ on the catalyst do not vary much from catalyst to catalyst. The rate constant for formaldehyde formation, calculated by $k_7 = \frac{m_7}{m_8}$, also does not exhibit a dramatic change. However, the trend of rate constants here again tracked the change in oxidation TOF shown in Figure 3-3, Chapter 3, suggesting that the change in oxidation TOF could also be due to change in rate constant.

Mechanism and kinetic parameters		**HPM-7/ N-C-600**	**HPM-15/ N-C-600**	**HPM-10/ C**	**HPM-20/ C**
$CH_3OH + s_b \overset{K_5}{\Longleftrightarrow} CH_3OH \cdot s_b$ $H_2O + s_b \overset{K_6}{\Longleftrightarrow} H_2O \cdot s_b$ $\boldsymbol{CH_3OH} \cdot s_b + \boldsymbol{\frac{1}{2}O_2} \xrightarrow{k_7} \boldsymbol{HCHO + H_2O + s_b}$ $\frac{dX_{ODH}}{d\tau} = \frac{m_7 * P_{CH3OH}}{1 + m_8 * P_{CH3OH} + m_9 * P_{H2O}}$	$m_7 = k_7 * K_5$ (kPa^{-1}ks^{-1})	5.89	2.93	3.22	6.94
	$m_8 = K_5$ (kPa^{-1})	0.27	0.49	0.21	0.15
	$m_9 = K_6$ (kPa^{-1})	0.46	1.13	0.77	0.95
	$\frac{m_7}{m_8} = k_7$ (ks^{-1})	22.2	6	15.3	46.3

Table 4-4. Kinetic parameters in HCHO formation.

Equilibrium constants and rate constants involved in DMM formation are shown in Table 4-5. Notice that the equilibrium constants for water and methanol adsorption on Site a (acid site) was addressed in the discussion of DME kinetics. The new parameters shown here are m_3 and m_{10}, where m_3 ($\frac{k_{-9}K_{10}}{K_1}$) controls how fast the forward and reverse reaction can achieve equilibrium, whereas m_{10} ($\frac{K_1K_8K_9}{K_{10}}$) controls the amount of DMM that can be made at equilibrium. The trend for m_3 is unclear. However, a trend for m_{10} can be observed from row 5. The m_{10} values for HPM/N-C-600 catalysts are much smaller than the ones for HPM/C, especially smaller than the one for HPM-20/C. One possible reason for this could be that HPM/N-C-600 catalysts have smaller K_1 values, so fewer methanol monomers are formed on the surface providing a lower m_{10} since $m_{10}=\frac{K_1K_8K_9}{K_{10}}$. However lower K_8, K_9 or higher K_{10} values can all lead to this trend. The fact that m_{10} is much lower for HPM/N-C-600 catalysts could be the main reason that these catalysts are more selective to HCHO compared to the other catalysts shown in Chapter 3, because the amount of DMM that can be made with HPM/N-C-600 catalysts is limited by the low m_{10} ($\frac{K_1K_8K_9}{K_{10}}$) value in DMM formation. This trend for m_{10} is very similar to the trend observed for k_4 (rate constant of DME formation, see Table 4-3), which suggests that our assumption about DME and DMM forming on the same site is reasonable.

Mechanism and kinetic parameters		**HPM-7/ N-C-600**	**HPM-15/ N-C-600**	**HPM-10/ C**	**HPM-20/ C**
$CH_3OH + s_a \overset{K_1}{\Longleftrightarrow} CH_3OH \cdot s_a$ $CH_3OH \cdot s_a + CH_3OH \overset{K_2}{\Longleftrightarrow} CH_3OH \cdot s_a \cdot CH_3OH$ $CH_3OH \cdot s_a + H_2O \overset{K_3}{\Longleftrightarrow} CH_3OH \cdot s_a \cdot H_2O$ $\boldsymbol{CH_3OH \cdot s_a \cdot CH_3OH \xrightarrow{k_4} CH_3OCH_3\ (DME) + H_2O + s_a}$ $CH_3OH \cdot s_a + HCHO \overset{K_8}{\Longleftrightarrow} HOCH_2OCH_3 \cdot s_a$ $\boldsymbol{HOCH_2OCH_3} \cdot s_a + \boldsymbol{CH_3OH} \underset{k_{-9}}{\overset{k_9}{\Longleftrightarrow}} \boldsymbol{CH_3OCH_2OCH_3 \cdot s_a + H_2O}$ $CH_3OCH_2OCH_3(DMM) + s_a \overset{K_{10}}{\Longleftrightarrow} CH_3OCH_2OCH_3 \cdot s_a$ $\frac{dX_{DMM}}{d\tau} = \frac{m_3 * (m_{10} * P_{HCHO} * P_{CH3OH}{}^2 - P_{DMM} * P_{H2O})}{P_{CH3OH} * (1 + m_4 * P_{CH3OH} + m_5 * P_{H2O})}$	$m_4 = K_2$ (kPa^{-1})	0.073	0.036	0.007-0.02	0-0.005
	$m_5 = K_3$ (kPa^{-1})	0.32	0.33	0	0.39
	$m_3 = \frac{k_{-9}K_{10}}{K_1}$ ($kPa^{-1}ks^{-1}$)	788	199.8	2622	79.3
	$m_{10} = \frac{K_1K_8K_9}{K_{10}}$ (kPa^{-1}) ($K_9 = \frac{k_9}{k_{-9}}$)	0.0018	0.00175	0.0027	0.088

Table 4-5. Kinetic parameters in DMM formation.

Equilibrium constants and rate constants involved in MF formation are shown in Table 4-6. Note that the equilibrium constants for water and methanol adsorption on Site b (oxidation site) were considered when formaldehyde kinetics were discussed. The rate constant for MF formation cannot be calculated because information of K_{11} could not be obtained from the model. However, a correlation between $k_{12} * K_{11}$ (row 4 in Table 4-6, a combination of the rate constant for MF formation and equilibrium constant for step 11 in Scheme 4-5) and k_7 (row 5 in Table 4-4, rate constant for HCHO formation) is found and plotted in Figure 4-11. This supports our assumption about HCHO and MF that both products are possibly formed on the same oxidation site.

Mechanism and kinetic parameters		**HPM-7/ N-C-600**	**HPM-15/ N-C-600**	**HPM-10/ C**	**HPM-20/ C**
$CH_3OH + s_b \overset{K_5}{\Longleftrightarrow} CH_3OH \cdot s_b$ $H_2O + s_b \overset{K_6}{\Longleftrightarrow} H_2O \cdot s_b$ $\boldsymbol{CH_3OH \cdot s_b + \frac{1}{2}O_2 \xrightarrow{k_7} HCHO + H_2O + s_b}$ $CH_3OH \cdot s_b + HCHO \overset{K_{11}}{\Longleftrightarrow} HOCH_2OCH_3 \cdot s_b$ $\boldsymbol{HOCH_2OCH_3 \cdot s_b + \frac{1}{2}O_2 \xrightarrow{k_{12}} HCOOCH_3 + H_2O \cdot s_b}$ $\frac{dX_{MF}}{d\tau} = \frac{m_2 * P_{HCHO} * P_{CH3OH}}{1 + m_8 * P_{CH3OH} + m_9 * P_{H2O}}$	$m_8 = K_5$ (kPa^{-1})	0.27	0.49	0.21	0.15
	$m_9 = K_6$ (kPa^{-1})	0.46	1.13	0.77	0.95
	$m_2 = k_{12} * K_5 * K_{11}$ (kPa^{-2}ks^{-1})	5	1.32	1.6	4
	$\frac{m_2}{m_8} = k_{12} * K_{11}$ (ks^{-1})	18.9	2.7	7.6	27

Table 4-6. Kinetic parameters in MF formation.

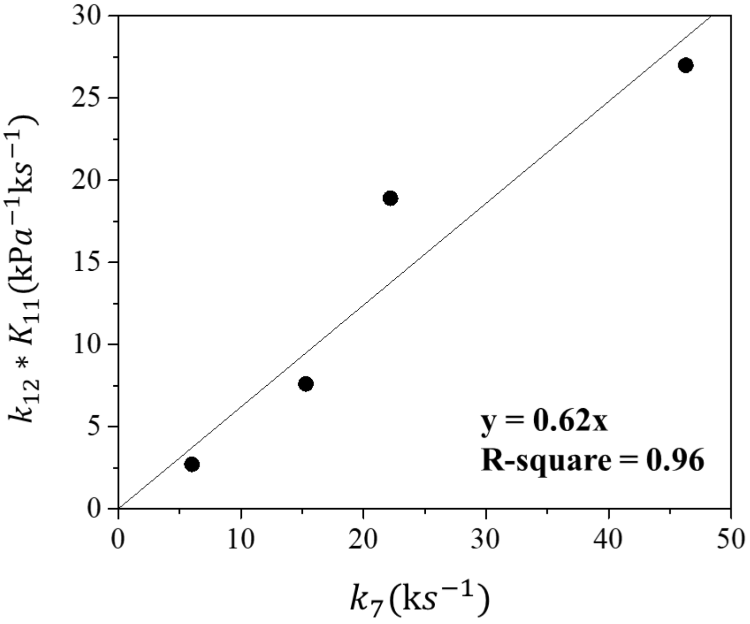

Figure 4-11. k_{12}*K_{11} (kPa^{-1}ks^{-1}) plotted versus k_7 (ks^{-1})

4.5 Conclusions

Detailed kinetics for methanol oxidation and dehydration have been proposed and discussed in this chapter. Mechanism-based kinetic models are constructed for both primary and secondary products for the first time in the literature, and have worked well for HPM/C and HPM/N-C-600 catalysts.

We have shown in this chapter that HCHO and MF may form on the same site (likely on the bridging O in the vicinity of H^+). DME and DMM may form on the same site (H^+). Both k_4(rate constant for DME formation, per POM or per H^+) and $\mathrm{m}_{10} = \frac{K_1 K_8 K_9}{K_{10}}$ follow the trend: HPM-20/C >> HPM-10/C > HPM-15/N-C-600 ≈ HPM-7/N-C-600. The fact that N-C-600 supported catalysts have lower m_{10} (most probably because of lower K_1, the equilibrium constant for CH_3OH adsorption on H^+), could be the reason why high HCHO selectivity can be achieved with this group of catalysts.

Chapter 5 Conclusions and Recommended Future Directions

5.1 Conclusions

The effects of using nitrogen-containing carbon materials as supports for POMs were studied in this work. The presence of intact and dispersed POMs was confirmed by FTIR and XRD, to show that the catalysts envisioned were actually made. HAADF-STEM images provided a view of the catalyst surface - at low surface coverage levels (< 0.09 POM/nm^2) POMs are mostly dispersed at molecular level on all the catalysts studied in this work.

XRD results combined with support XPS spectra provided valuable information on the nature of interactions between POMs and nitrogen-containing supports. We have shown that supports with -NH_2 groups on the surface have the tendency to form ammonium POM salts at high POM loadings. In the meantime, the loading threshold for mpgC_3N_4 to form ammonium POM salts was much higher than N-C-600, possibly because of its ordered structure or the very high number of pyridinic nitrogen sites on the surface. Therefore, if one wants to choose a nitrogen-containing carbon material to disperse as many POMs as possible, more pyridinic nitrogen and fewer amino groups would appear to the key characteristics.

NH_3-TPD and butene chemisorption were used to measure the number and strength of acid sites on the catalysts. The H^+/POM ratios from these two methods were generally consistent, in that both methods gave a H^+/POM ratio for HPM/C catalysts of about 1.2, and ratio for HPM/N-C-600 of about 0.5. Thus, the general trend of decreasing H^+/POM ratio when supports with higher nitrogen content are used can be confirmed by both methods. Butene chemisorption provided a more complete data set, and showed that at similar POM surface coverage level, the interaction between POMs and supports followed the trend: $mpgC_3N_4 > N\text{-}C\text{-}600 > N\text{-}C\text{-}1000 \approx C$. NH_3-TPD data was mainly used to analyze the trend of H^+/POM ratio for HPM/C catalysts with different loadings, where it demonstrated that for low-loading HPM/C catalyst (HPM-7/C and HPM-10/C), the H^+/POM ratio can be as low as 0.83, as opposed to 1.40 for HPM-30/C. Combining these results, if one wants to choose a support for POMs to provide high stability, then POM/N-C-600, POM/mpgC_3N_4 or low-loading POM/C are good choices. Among these, POM/mpgC_3N_4 exhibited the strongest interactions, suggesting that the more pyridinic nitrogen, the stronger the interaction.

Results from methanol test reactions demonstrated that as supports with higher nitrogen content were used, dehydration rates dropped significantly. Combining dehydration rates for HPM/C and HPM/N-C-600 with the results from NH_3-TPD and applying the thermodynamic proton activity theory developed for cation-exchange POM catalysts, we found that the dehydration rates per thermodynamic proton activity were almost constant for every loading of HPM/C and HPM/N-C-600 catalysts. This suggests that using support to control acid sites probably follows the same rule as when using cation exchange to control acid sites, where in both cases H^+/POM ratio is the factor that matters because it determines the acid site strength (thermodynamic activity for protons).

However, the oxidation rates showed different trends as the H^+/POM ratio was decreased via support interaction or by cation exchange. While cation exchange results in identical trends for both dehydration and oxidation rates and thus constant oxidation selectivity, in the case of using nitrogen-containing carbon supports, the selectivity for oxidation products was improved when a small but finite number of acid sites existed on the catalyst surface. Too many acid sites, as in the case of high loading HPM/C catalysts, result in high DME selectivity, whereas too few acid sites, as on HPM/mpgC_3N_4, would sacrifice too much oxidation activity, plus a basic surface could possibly lead to more CO_x formation. For supports used in this work, N-C-600 appears to provide an optimal number of acid sites and thus results in the highest selectivity for the sum of all oxidation products (CO_X excluded), as well as the highest selectivity for HCHO. This indicates that little of the product HCHO reacts further to form DMM or MF.

When looking at the trend of methanol oxidation and dehydration from a kinetics perspective, the decrease in both DME TOF and Oxidation TOF results from a decrease in the rate constant for the respective rate determining steps. This decrease in rate constant reflects either an increase in energy of the transition state or decrease in energy for the adsorbed species preceding the rate determining step. Current data could not differentiate between these two. A detailed DFT study and methanol calorimetry study would be helpful for answering this question.

5.2 Recommended Future Directions

5.2.1 DFT

Density Functional Theory (DFT) has been used by Iglesia and co-workers to study methanol dehydration and oxidation with SiO_2-supported POM catalysts[24, 86]. They have proposed to use separate assessments of ionic and covalent DPE as a descriptor for DME reactivity as well as HAE as a descriptor for oxidative dehydrogenation reaction of methanol. Although DFT calculation of N-C-600 and N-C-1000 supported POM catalyst is hard to do because the specific structures of the supports are unknown, it is easier to perform DFT calculations for carbon and carbon nitride supported POM systems based on their more ordered structures[79, 88, 89]. Performing DFT for these two materials can provide a limiting-case analysis for the support effect when using nitrogen-containing carbon materials as support for POMs. Information like the adsorption energy of methanol on acid sites and oxidation sites, as well as calculated DPE and HAE value for C and mpgC_3N_4 supported POM catalysts would shed light on how support effects lead to the change in rate constants for dehydration and oxidation of methanol observed in our kinetics study.

5.2.2 Calorimetry

Calorimetry experiments for methanol adsorption would be useful to carry out for POM supported on C, N-C-1000, N-C-600 and mpgC_3N_4 to measure the differential heat of adsorption for methanol on these catalysts[90, 91]. Experimental results from calorimetry studies can be compared with the calculated adsorption energies for methanol adsorption on both acid sites and oxidation sites using DFT (discussed in Section 5.2.1). This comparison could help provide a clearer image of how the energy of methanol adsorbed on the catalyst changes on both acid and oxidation sites due to support effects.

5.2.3 Liquid-phase reactions

A strong interaction between POMs and supports is desirable to prevent POMs from leaching into solvent in liquid-phase reactions[92, 93]. Maksimov and co-workers[94] have shown that when using carbon supported Co-substituted POM catalyst in α-pinene/isobutyraldehyde co-oxidation, both epoxide selectivity and the alkene conversion were superior to those achieved using corresponding homogeneous catalysts, and that during the reaction carbon-supported POM catalysts are heterogeneous in nature even when highly polar products such as carboxylic acids are formed in the reaction. However, it has been shown in the literature, as well as in our water washing experiment results, that carbon can only bind POMs strongly under a loading limit of about 10-15 wt%[8], while that limit for N-C-600 and mpgC_3N_4 is much higher. Therefore, using N-C-600 or mpgC_3N_4 supported POM catalysts could permit lower total amounts of catalysts to be used while retaining POMs from leaching into the solvent. Possible reactions to consider are oxidation of olefins, oxidation of phenols as well as oxidation of alcohols and aldehydes in the liquid-phase. A balance of sacrificing acid sites and less leaching may need to be considered when acid sites are involved in the reaction.

Bibliography

[1] M. Misono, Heterogeneous catalysis by heteropoly compounds of molybdenum and tungsten, Catalysis Reviews Science and Engineering, 29 (1987) 269-321.

[2] N. Mizuno, M. Misono, Heteropolyanions in catalysis, Journal of molecular catalysis, 86 (1994) 319-342.

[3] I.V. Kozhevnikov, Heteropoly acids and related compounds as catalysts for fine chemical synthesis, Catalysis Reviews, 37 (1995) 311-352.

[4] I.K. Song, M.A. Barteau, Redox properties of Keggin-type heteropolyacid (HPA) catalysts: effect of counter-cation, heteroatom, and polyatom substitution, Journal of molecular catalysis A: Chemical, 212 (2004) 229-236.

[5] M. Ai, Characteristics of heteropoly compounds as catalysts for selective oxidation, Journal of Catalysis, 71 (1981) 88-98.

[6] A. Mamoru, Effects of cations introduced into 12-molybdophosphoric acid on the catalyst properties, Applied Catalysis, 4 (1982) 245-256.

[7] M.A. Barteau, J.E. Lyons, I.K. Song, Surface chemistry and catalysis on well-defined oxide surfaces: nanoscale design bases for single-site heterogeneous catalysts, Journal of Catalysis, 216 (2003) 236-245.

[8] M.A. Schwegler, P. Vinke, M. Van der Eijk, H. Van Bekkum, Activated carbon as a support for heteropolyanion catalysts, Applied Catalysis A: General, 80 (1992) 41-57.

[9] P.G. Vázquez, M.N. Blanco, C.V. Cáceres, Catalysts based on supported 12-molybdophosphoric acid, Catalysis letters, 60 (1999) 205-215.

[10] J. Haber, L. Matachowski, K. Pamin, B. Napruszewska, Catalytic activity of supported silver and potassium salts of tungstophosphoric acid in dehydration of ethanol, Bulletin of the Polish Academy of Sciences. Chemistry, 50 (2002) 189-202.

[11] M. Hasik, W. Turek, E. Stochmal, M. Lapkowski, A. Pron, Conjugated polymer-supported catalysts-polyaniline protonated with 12-tungstophosphoric acid, Journal of Catalysis, 147 (1994) 544-551.

[12] Y. Zhu, M. Zhu, L. Kang, F. Yu, B. Dai, Phosphotungstic Acid Supported on Mesoporous Graphitic Carbon Nitride as Catalyst for Oxidative Desulfurization of Fuel, Industrial & Engineering Chemistry Research, 54 (2015) 2040-2047.

[13] R. Liu, S. Li, X. Yu, G. Zhang, S. Zhang, J. Yao, B. Keita, L. Nadjo, L. Zhi, Facile Synthesis of Au-Nanoparticle/Polyoxometalate/Graphene Tricomponent Nanohybrids: An Enzyme-Free Electrochemical Biosensor for Hydrogen Peroxide, Small, 8 (2012) 1398-1406.

[14] M. Sadakane, E. Steckhan, Electrochemical properties of polyoxometalates as electrocatalysts, Chemical Reviews, 98 (1998) 219-238.

[15] Y. He, L. Zhang, X. Wang, Y. Wu, H. Lin, L. Zhao, W. Weng, H. Wan, M. Fan, Enhanced photodegradation activity of methyl orange over Z-scheme type MoO 3–gC 3 N 4 composite under visible light irradiation, RSC Advances, 4 (2014) 13610-13619.

[16] H. Li, S. Pang, S. Wu, X. Feng, K. Müllen, C. Bubeck, Layer-by-layer assembly and UV photoreduction of graphene–polyoxometalate composite films for electronics, Journal of the American Chemical Society, 133 (2011) 9423-9429.

[17] M. Genovese, K. Lian, Polyoxometalate modified inorganic–organic nanocomposite materials for energy storage applications: A review, Current Opinion in Solid State and Materials Science, (2015).

[18] S. Omwoma, C.T. Gore, Y. Ji, C. Hu, Y.-F. Song, Environmentally benign polyoxometalate materials, Coordination Chemistry Reviews, 286 (2015) 17-29.

[19] N. Mizuno, M. Misono, Heterogeneous catalysis, Chemical Reviews, 98 (1998) 199-218.

[20] T. Okuhara, N. Mizuno, M. Misono, Catalytic Chemistry of Heteropoly Compounds, Advances in Catalysis, 41 (1996) 113-252.

[21] Y. Moro-oka, The role of acidic properties of metal oxide catalysts in the catalytic oxidation, Applied Catalysis A: General, 181 (1999) 323-329.

[22] T. Okuhara, N. Mizuno, M. Misono, Catalysis by heteropoly compounds—recent developments, Applied Catalysis A: General, 222 (2001) 63-77.

[23] S. Xu, L. Wang, W. Chu, W. Yang, Catalytic oxidation of ethylene to acetic acid on Pd–HPA/SiO 2 catalysts with different heteropoly acids, Reaction Kinetics and Catalysis Letters, 98 (2009) 107-115.

[24] P. Deshlahra, R.T. Carr, S.-H. Chai, E. Iglesia, Mechanistic details and reactivity descriptors in oxidation and acid catalysis of methanol, ACS Catalysis, 5 (2014) 666-682.

[25] J. Macht, M.J. Janik, M. Neurock, E. Iglesia, Catalytic consequences of composition in polyoxometalate clusters with Keggin structure, Angewandte Chemie, 119 (2007) 8010-8014.

[26] J.-P. Tessonnier, S. Goubert-Renaudin, S. Alia, Y. Yan, M.A. Barteau, Structure, Stability, and Electronic Interactions of Polyoxometalates on Functionalized Graphene Sheets, Langmuir, 29 (2012) 393-402.

[27] M.S. Kaba, I.K. Song, M.A. Barteau, Ordered Array Formation and Negative Differential Resistance Behavior of Cation-Exchanged Heteropoly Acids Probed by Scanning Tunneling Microscopy, The Journal of Physical Chemistry, 100 (1996) 19577-19581.

[28] I. Song, M. Kaba, G. Coulston, K. Kourtakis, M. Barteau, Scanning tunneling microscopy of ordered arrays of heteropolyacids deposited on a graphite surface, Chemistry of materials, 8 (1996) 2352-2358.

[29] P. Deshlahra, R.T. Carr, S.-H. Chai, E. Iglesia, Mechanistic Details and Reactivity Descriptors in Oxidation and Acid Catalysis of Methanol, ACS Catalysis, 5 (2015) 666-682.

[30] J.M. Tatibouët, Methanol oxidation as a catalytic surface probe, Applied Catalysis A: General, 148 (1997) 213-252.

[31] S. Xu, L. Wang, W. Chu, W. Yang, Catalytic oxidation of ethylene to acetic acid on Pd–HPA/SiO2 catalysts with different heteropoly acids, Reaction Kinetics and Catalysis Letters, 98 (2009) 107-115.

[32] M. Hasik, W. Turek, E. Stochmal, M. Lapkowski, A. Pron, Conjugated Polymer-Supported Catalysts - Polyaniline Protonated with 12-Tungstophosphoric Acid, Journal of Catalysis, 147 (1994) 544-551.

[33] H. Liu, E. Iglesia, Effects of support on bifunctional methanol oxidation pathways catalyzed by polyoxometallate Keggin clusters, Journal of Catalysis, 223 (2004) 161-169.

[34] B.A. Watson, M.A. Barteau, L. Haggerty, A.M. Lenhoff, R.S. Weber, Scanning tunneling microscopy and tunneling spectroscopy of ordered hetero-and isopolyanion arrays on graphite, Langmuir, 8 (1992) 1145-1148.

[35] A.K. Cuentas-Gallegos, R. Martínez-Rosales, M.E. Rincón, G.A. Hirata, G. Orozco, Design of hybrid materials based on carbon nanotubes and polyoxometalates, Optical materials, 29 (2006) 126-133.

[36] N. Kawasaki, H. Wang, R. Nakanishi, S. Hamanaka, R. Kitaura, H. Shinohara, T. Yokoyama, H. Yoshikawa, K. Awaga, Nanohybridization of Polyoxometalate Clusters and Single-Wall Carbon Nanotubes: Applications in Molecular Cluster Batteries, Angewandte Chemie, 123 (2011) 3533-3536.

[37] H. Kim, J.C. Jung, D.R. Park, J. Lee, K.M. Cho, S. Park, S.H. Lee, I.K. Song, Immobilization of H3PMo12O40 catalyst on the nitrogen-containing mesoporous carbon and its application to the vapor-phase 2-propanol conversion reaction, Korean Journal of Chemical Engineering, 25 (2008) 231-235.

[38] D. Zhou, B.H. Han, Graphene-Based Nanoporous Materials Assembled by Mediation of Polyoxometalate Nanoparticles, Advanced Functional Materials, 20 (2010) 2717-2722.

[39] K.W. La, H. Kim, J.C. Jung, J. Lee, D.R. Park, S.H. Lee, I.K. Song, Preparation of H5PMo10V2O40 catalyst immobilized on spherical carbon and its application to the vapor-phase 2-propanol conversion reaction, Korean Journal of Chemical Engineering, 25 (2008) 710-713.

[40] Y. Bang, D.R. Park, Y.J. Lee, J.C. Jung, I.K. Song, Preparation, characterization, and oxidation catalysis of H3PMo12O40 heteropolyacid catalyst immobilized on carbon aerogel, Korean Journal of Chemical Engineering, 28 (2011) 79-83.

[41] H. Kim, D.R. Park, S. Park, J.C. Jung, S.-B. Lee, I.K. Song, Preparation, characterization, and catalytic activity of H5PMo10V2O40 immobilized on nitrogen-containing mesoporous

carbon (PMo10V2/N-MC) for selective conversion of methanol to dimethoxymethane, Korean Journal of Chemical Engineering, 26 (2009) 660-665.

[42] J. Lee, H. Kim, K.W. La, D.R. Park, J.C. Jung, S.H. Lee, I.K. Song, Chemical immobilization of H5PMo10V2O40 (PMo10V2) catalyst on nitrogen-rich macroporous carbon (N-MC) for use as an oxidation catalyst, Catalysis Letters, 123 (2008) 90-95.

[43] W. Liu, W. Qi, X. Guo, D. Su, Heteropoly Acid/Nitrogen Functionalized Onion-like Carbon Hybrid Catalyst for Ester Hydrolysis Reactions, Chemistry–An Asian Journal, (2015).

[44] J. Poźniczek, A. Bielański, I. Kulszewicz-Bajer, M. Zagorska, K. Kruczała, K. Dyrek, A. Proń, Heteropolyanion-doped polypyrrole as catalyst for ethyl alcohol conversion, Journal of molecular catalysis, 69 (1991) 223-233.

[45] K. Nomiya, H. Murasaki, M. Miwa, Catalysis by heteropolyacids—VIII. Immobilization of keggin-type heteropolyacids on poly (4-vinylpyridine), Polyhedron, 5 (1986) 1031-1033.

[46] A. Thomas, A. Fischer, F. Goettmann, M. Antonietti, J.-O. Müller, R. Schlögl, J.M. Carlsson, Graphitic carbon nitride materials: variation of structure and morphology and their use as metal-free catalysts, Journal of Materials Chemistry, 18 (2008) 4893-4908.

[47] J. He, H. Sun, S. Indrawirawan, X. Duan, M.O. Tade, S. Wang, Novel polyoxometalate@ gC 3 N 4 hybrid photocatalysts for degradation of dyes and phenolics, Journal of colloid and interface science, 456 (2015) 15-21.

[48] Z. Long, Y. Zhou, G. Chen, W. Ge, J. Wang, C3N4-H5PMo10V2O40: a dual-catalysis system for reductant-free aerobic oxidation of benzene to phenol, Scientific reports, 4 (2014).

[49] C. Rocchiccioli-Deltcheff, A. Aouissi, S. Launay, M. Fournier, Silica-supported 12-molybdophosphoric acid catalysts: Influence of the thermal treatments and of the Mo

contents on their behavior, from IR, Raman, X-ray diffraction studies, and catalytic reactivity in the methanol oxidation, Journal of molecular catalysis A: Chemical, 114 (1996) 331-342.

[50] C. Rocchiccioli-Deltcheff, M. Amirouche, M. Fournier, Structure and catalytic properties of silica-supported polyoxomolybdates III. 12-molybdosilicic acid catalysts: vibrational study of the dispersion effect and nature of the Mo species in interaction with the silica support, Journal of Catalysis, 138 (1992) 445-456.

[51] C. Rocchiccioli-Deltcheff, M. Fournier, R. Franck, R. Thouvenot, Vibrational investigations of polyoxometalates. 2. Evidence for anion-anion interactions in molybdenum (VI) and tungsten (VI) compounds related to the Keggin structure, Inorganic Chemistry, 22 (1983) 207-216.

[52] B. Viswanadham, A. Srikanth, K.V. Chary, Characterization and reactivity of 11-molybdo-1-vanadophosphoric acid catalyst supported on zirconia for dehydration of glycerol to acrolein, Journal of Chemical Sciences, 126 (2014) 445-454.

[53] M. Fournier, C. Feumi-Jantou, C. Rabia, G. Hervé, S. Launay, Polyoxometalates catalyst materials: X-ray thermal stability study of phosphorus-containing heteropolyacids H 3+ x PM 12–x V x O 40· 13–14H 2 O (M= Mo, W; x= 0–1), Journal of Materials Chemistry, 2 (1992) 971-978.

[54] P. Madhusudhan Rao, A. Wolfson, S. Kababya, S. Vega, M.V. Landau, Immobilization of molecular H3PW12O40 heteropolyacid catalyst in alumina-grafted silica-gel and mesostructured SBA-15 silica matrices, Journal of Catalysis, 232 (2005) 210-225.

[55] J. Macht, R.T. Carr, E. Iglesia, Consequences of acid strength for isomerization and elimination catalysis on solid acids, Journal of the American Chemical Society, 131 (2009) 6554-6565.

[56] H. Liu, N. Bayat, E. Iglesia, Site titration with organic bases during catalysis: Selectivity modifier and structural probe in methanol oxidation on Keggin clusters, Angewandte Chemie, 115 (2003) 5226-5229.

[57] W. Knaeble, E. Iglesia, Kinetic and theoretical insights into the mechanism of alkanol dehydration on solid Brønsted acid catalysts, The Journal of Physical Chemistry C, 120 (2016) 3371-3389.

[58] R.T. Carr, M. Neurock, E. Iglesia, Catalytic consequences of acid strength in the conversion of methanol to dimethyl ether, Journal of catalysis, 278 (2011) 78-93.

[59] W.-G. Kim, M.-W. Kim, J.-H. Kim, G. Seo, Dispersion measurement of heteropoly acid supported on KIT-1 mesoporous material, Microporous and mesoporous materials, 57 (2003) 113-120.

[60] B.B. Bardin, S.V. Bordawekar, M. Neurock, R.J. Davis, Acidity of Keggin-type heteropolycompounds evaluated by catalytic probe reactions, sorption microcalorimetry, and density functional quantum chemical calculations, The Journal of Physical Chemistry B, 102 (1998) 10817-10825.

[61] L.-N. Han, X. Wei, Q.-C. Zhu, S.-M. Xu, K.-X. Wang, J.-S. Chen, Nitrogen-doped carbon nets with micro/mesoporous structures as electrodes for high-performance supercapacitors, J. Mater. Chem. A, 4 (2016) 16698-16705.

[62] Y.Y. Cai, X.H. Li, Y.N. Zhang, X. Wei, K.X. Wang, J.S. Chen, Highly Efficient Dehydrogenation of Formic Acid over a Palladium-Nanoparticle-Based Mott–Schottky Photocatalyst, Angewandte Chemie International Edition, 52 (2013) 11822-11825.

[63] M.S. Kaba, I.K. Song, D.C. Duncan, C.L. Hill, M.A. Barteau, Molecular Shapes, Orientation, and Packing of Polyoxometalate Arrays Imaged by Scanning Tunneling Microscopy, Inorganic Chemistry, 37 (1998) 398-406.

[64] G.M. Brown, M.-R. Noe-Spirlet, W.R. Busing, H.A. Levy, Dodecatungstophosphoric acid hexahydrate, (H5O2+)3(PW12O403-). The true structure of Keggin's `pentahydrate' from single-crystal X-ray and neutron diffraction data, Acta Crystallographica Section B, 33 (1977) 1038-1046.

[65] B. Jurgens, E. Irran, J. Senker, P. Kroll, H. Muller, W. Schnick, Melem (2,5,8-triamino-tri-s-triazine), an important intermediate during condensation of melamine rings to graphitic carbon nitride: synthesis, structure determination by X-ray powder diffractometry, solid-state NMR, and theoretical studies, J Am Chem Soc, 125 (2003) 10288-10300.

[66] K.L. Tan, B.T.G. Tan, E.T. Kang, K.G. Neoh, X-ray photoelectron spectroscopy studies of the chemical structure of polyaniline, Physical Review B, 39 (1989) 8070-8073.

[67] J. Boutique, J. Verbist, J. Fripiat, J. Delhalle, G. Pfister-Guillouzo, G. Ashwell, 3, 5, 11, 13-tetraazacycl [3.3. 3] azine: Theoretical (ab initio) and experimental (X-ray and ultraviolet photoelectron spectroscopy) studies of the electronic structure, Journal of the American Chemical Society, 106 (1984) 4374-4378.

[68] R. Arrigo, M. Hävecker, S. Wrabetz, R. Blume, M. Lerch, J. McGregor, E.P.J. Parrott, J.A. Zeitler, L.F. Gladden, A. Knop-Gericke, R. Schlögl, D.S. Su, Tuning the Acid/Base

Properties of Nanocarbons by Functionalization via Amination, Journal of the American Chemical Society, 132 (2010) 9616-9630.

[69] J. Casanovas, J.M. Ricart, J. Rubio, F. Illas, J.M. Jiménez-Mateos, Origin of the large N 1s binding energy in X-ray photoelectron spectra of calcined carbonaceous materials, Journal of the American Chemical Society, 118 (1996) 8071-8076.

[70] R. Arrigo, M. Hävecker, R. Schlögl, D.S. Su, Dynamic surface rearrangement and thermal stability of nitrogen functional groups on carbon nanotubes, Chemical Communications, (2008) 4891-4893.

[71] E. Arendt, K.M. McEvoy, E.M. Gaigneaux, Structural rearrangement and catalytic properties of the Wells–Dawson (NH4)6P2Mo18O62 heteropolycompound in the 2-butanol reaction, Applied Catalysis A: General, 357 (2009) 115-124.

[72] Y. Cui, Z. Ding, P. Liu, M. Antonietti, X. Fu, X. Wang, Metal-free activation of H2O2 by g-C3N4 under visible light irradiation for the degradation of organic pollutants, Physical Chemistry Chemical Physics, 14 (2012) 1455-1462.

[73] F.C. Jentoft, S. Klokishner, J. Kröhnert, J. Melsheimer, T. Ressler, O. Timpe, J. Wienold, R. Schlögl, The structure of molybdenum-heteropoly acids under conditions of gas-phase selective oxidation catalysis: a multi-method in situ study, Applied Catalysis A: General, 256 (2003) 291-317.

[74] F. Chami, L. Dermeche, A. Saadi, C. Rabia, Propan-2-ol conversion to diisopropyl ether over (NH4) xXyPMo12O40 salts with X= Sn, Sb, and Bi. The effect of salt preparation pH, Applied Petrochemical Research, 3 (2013) 35-45.

[75] M.J. Janik, R.J. Davis, M. Neurock, The relationship between adsorption and solid acidity of heteropolyacids, Catalysis today, 105 (2005) 134-143.

[76] I.V. Kozhevnikov, Catalysis by heteropoly acids and multicomponent polyoxometalates in liquid-phase reactions, Chemical Reviews, 98 (1998) 171-198.

[77] G.G. Papagianni, D.V. Stergiou, G.S. Armatas, M.G. Kanatzidis, M.I. Prodromidis, Synthesis, characterization and performance of polyaniline–polyoxometalates (XM 12, X= P, Si and M= Mo, W) composites as electrocatalysts of bromates, Sensors and Actuators B: Chemical, 173 (2012) 346-353.

[78] K. Li, L. Yan, Z. Zeng, S. Luo, X. Luo, X. Liu, H. Guo, Y. Guo, Fabrication of H 3 PW 12 O 40-doped carbon nitride nanotubes by one-step hydrothermal treatment strategy and their efficient visible-light photocatalytic activity toward representative aqueous persistent organic pollutants degradation, Applied Catalysis B: Environmental, 156 (2014) 141-152.

[79] L.M. Azofra, D.R. MacFarlane, C. Sun, A DFT study of planar vs. corrugated graphene-like carbon nitride (g-C3N4) and its role in the catalytic performance of CO2 conversion, Physical chemistry chemical physics : PCCP, 18 (2016) 18507-18514.

[80] Y. Bang, D.R. Park, Y.J. Lee, J.C. Jung, I.K. Song, Preparation, characterization, and oxidation catalysis of H 3 PMo 12 O 40 heteropolyacid catalyst immobilized on carbon aerogel, Korean Journal of Chemical Engineering, 28 (2011) 79-83.

[81] H. Kim, J.C. Jung, D.R. Park, S.-H. Baeck, I.K. Song, Preparation of H 5 PMo 10 V 2 O 40 (PMo 10 V 2) catalyst immobilized on nitrogen-containing mesoporous carbon (N-MC) and its application to the methacrolein oxidation, Applied Catalysis A: General, 320 (2007) 159-165.

[82] H. Kim, J.C. Jung, D.R. Park, J. Lee, K.M. Cho, S. Park, S.H. Lee, I.K. Song, Immobilization of H 3 PMo 12 O 40 catalyst on the nitrogen-containing mesoporous carbon

and its application to the vapor-phase 2-propanol conversion reaction, Korean Journal of Chemical Engineering, 25 (2008) 231-235.

[83] E. Hückel, The theory of concentrated, aqueous solutions of strong electrolytes, Phys. Z, 26 (1925) 93-147.

[84] H.S. Harned, The activity coefficient of hydrochloric acid in concentrated solutions of strong electrolytes, Journal of the American Chemical Society, 48 (1926) 326-342.

[85] H.S. Harned, R. Gary, The Activity Coefficient of Hydrochloric Acid in Concentrated Aqueous Higher Valence Type Chloride Solutions at 25°. I. The System Hydrochloric Acid-Barium Chloride, Journal of the American Chemical Society, 76 (1954) 5924-5927.

[86] P. Deshlahra, E. Iglesia, Methanol oxidative dehydrogenation on oxide catalysts: molecular and dissociative routes and hydrogen addition energies as descriptors of reactivity, The Journal of Physical Chemistry C, 118 (2014) 26115-26129.

[87] H. Liu, E. Iglesia, Selective One-Step Synthesis of Dimethoxymethane via Methanol or Dimethyl Ether Oxidation on H3+ n V n Mo12-n PO40 Keggin Structures, The Journal of Physical Chemistry B, 107 (2003) 10840-10847.

[88] S. Wen, W. Guan, J. Wang, Z. Lang, L. Yan, Z. Su, Theoretical investigation of structural and electronic propertyies of [PW 12 O 40] 3− on graphene layer, Dalton Transactions, 41 (2012) 4602-4607.

[89] J. Gracia, P. Kroll, Corrugated layered heptazine-based carbon nitride: the lowest energy modifications of C3N4 ground state, Journal of Materials Chemistry, 19 (2009) 3013.

[90] W. Alharbi, E. Brown, E.F. Kozhevnikova, I.V. Kozhevnikov, Dehydration of ethanol over heteropoly acid catalysts in the gas phase, Journal of Catalysis, 319 (2014) 174-181.

[91] W. Alharbi, E.F. Kozhevnikova, I.V. Kozhevnikov, Dehydration of methanol to dimethyl ether over heteropoly acid catalysts: The relationship between reaction rate and catalyst acid strength, ACS Catalysis, 5 (2015) 7186-7193.

[92] Y. Izumi, K. Urabe, Catalysis of heteropoly acids entrapped in activated carbon, Chemistry Letters, 10 (1981) 663-666.

[93] R. Jansen, H. Van Veldhuizen, M. Schwegler, H. Van Bekkum, Recent (1987-1993) developments in heteropolyacid catalysts in acid catalyzed reactions and oxidation catalysis, Recueil des Travaux Chimiques des Pays-Bas, 113 (1994) 115-135.

[94] O. Kholdeeva, N. Maksimchuk, G. Maksimov, Polyoxometalate-based heterogeneous catalysts for liquid phase selective oxidations: Comparison of different strategies, Catalysis today, 157 (2010) 107-113.